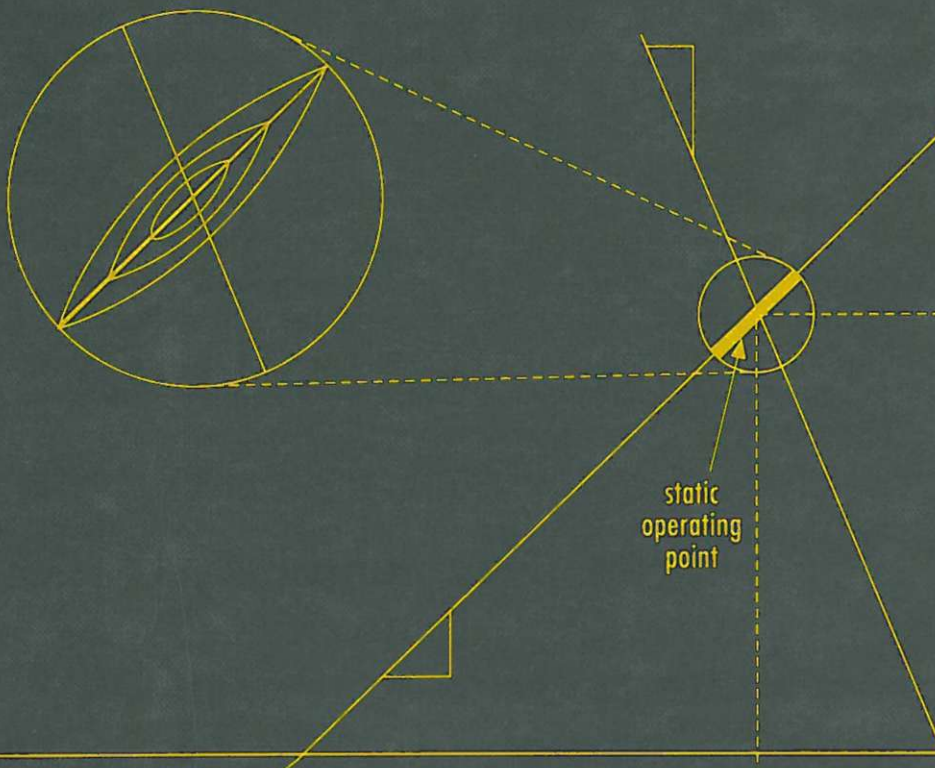


# Brushless Permanent-Magnet Motor Design



DUANE C. HANSELMAN

---

# **Brushless Permanent-Magnet Motor Design**

**Duane C. Hanselman**

*University of Maine  
Orono, Maine*

**McGraw-Hill, Inc.**

New York San Francisco Washington, D.C. Auckland Bogotá  
Caracas Lisbon London Madrid Mexico City Milan  
Montreal New Delhi San Juan Singapore  
Sydney Tokyo Toronto

Library of Congress Cataloging-in-Publication Data

Hanselman, Duane C.

Brushless permanent-magnet motor design / Duane C. Hanselman.  
p. cm.

Includes bibliographical references and index.

ISBN 0-07-026025-7 (alk. paper)

1. Electric motors, Permanent magnet—Design and construction.
2. Electric motors, Brushless—Design and construction. I. Title.

TK2537.H36 1994

621.46—dc20

93-43581

CIP

Copyright © 1994 by McGraw-Hill, Inc. All rights reserved. Printed in the United States of America. Except as permitted under the United States Copyright Act of 1976, no part of this publication may be reproduced or distributed in any form or by any means, or stored in a data base or retrieval system, without the prior written permission of the publisher.

2 3 4 5 6 7 8 9 0 DOC/DOC 9 9 8 7 6 5 4

ISBN 0-07-026025-7

*The sponsoring editor for this book was Harold B. Crawford, the editing supervisor was Paul R. Sobel, and the production supervisor was Pamela A. Pelton. It was set in Century Schoolbook by Techna Type, Inc.*

*Printed and bound by R. R. Donnelley & Sons Company.*

Information contained in this book has been obtained by McGraw-Hill, Inc. from sources believed to be reliable. However, neither McGraw-Hill nor its authors guarantee the accuracy or completeness of any information published herein, and neither McGraw-Hill nor its authors shall be responsible for any errors, omissions, or damages arising out of use of this information. This work is published with the understanding that McGraw-Hill and its authors are supplying information but are not attempting to render engineering or other professional services. If such services are required, the assistance of an appropriate professional should be sought.



This book is printed on recycled, acid-free paper containing a minimum of 50% recycled de-inked fiber.

---

# Contents

Preface	ix
<b>Chapter 1. Basic Concepts</b>	1
Scope	1
Shape	1
Torque	4
Motor Action	5
Magnet Poles and Motor Phases	8
Poles, Slots, and Teeth	9
Mechanical and Electrical Measures	10
Motor Size	11
Conclusion	12
<b>Chapter 2. Magnetic Modeling</b>	13
Magnetic Circuit Concepts	14
Basic relationships	14
Magnetic field sources	17
Air gap modeling	19
Slot modeling	21
Example	24
Magnetic Materials	26
Permeability	26
Ferromagnetic materials	26
Core loss	28
Permanent magnets	30
PM magnetic circuit model	34
Example	36
Conclusion	38
<b>Chapter 3. Electrical and Mechanical Relationships</b>	41
Flux Linkage and Inductance	41
Self inductance	41
Mutual inductance	42
Mutual flux due to a permanent magnet	44

<b>Induced Voltage</b>	46
Faraday's law	46
Example	47
<b>Energy and Coenergy</b>	48
Energy and coenergy in singly excited systems	48
Energy and coenergy in doubly excited systems	50
Coenergy in the presence of a permanent magnet	51
<b>Force, Torque, and Power</b>	52
Basic relationships	52
Fundamental implications	53
Torque from a macroscopic viewpoint	54
Force from a microscopic viewpoint	56
Reluctance and mutual torque	57
Example	58
 <b>Chapter 4. Brushless Motor Operation</b>	 61
<b>Assumptions</b>	61
Rotational motion	61
Motor load	61
Motor drive	62
Slotting	62
Surface-mounted magnets	62
Steel	63
<b>Basic Motor Operation</b>	63
<b>Magnetic Circuit Model</b>	64
<b>Flux Linkage</b>	69
<b>Back EMF</b>	70
<b>Force</b>	73
Multiple phases	74
<b>Winding Approaches</b>	75
Single-layer lap winding	76
Double-layer lap winding	77
Single-layer wave winding	77
<b>Self Inductance</b>	78
Air gap inductance	80
Slot leakage inductance	81
End turn leakage inductance	82
Summary	84
<b>Mutual Inductance</b>	85
<b>Winding Resistance</b>	86
DC resistance	87
AC resistance	88
<b>Armature Reaction</b>	89
<b>Conductor Forces</b>	91
Intrawinding force	92
Current induced winding force	92
Permanent-magnet induced winding force	93
Summary	93
<b>Cogging Force</b>	93
<b>Rotor-Stator Attraction</b>	95
<b>Core Loss</b>	95

<b>Summary</b>	96
<b>Fundamental Design Issues</b>	96
Air gap flux density	97
Active motor length	97
Number of magnet poles	97
Slot current	98
Electric versus magnetic loading	99
<b>Dual Air Gap Motor Construction</b>	99
<b>Summary</b>	101
<b>Chapter 5. Design Variations</b>	103
<b>Rotor Variations</b>	103
<b>Stator Variations</b>	106
<b>Shoes and Teeth</b>	107
<b>Slotted Stator Design</b>	110
Fractional pitch cogging torque reduction	112
Back emf smoothing	113
Distribution factor	113
Pitch factor	115
<b>Cogging Torque Reduction</b>	117
Shoes	118
Fractional pitch winding	118
Air gap lengthening	118
Skewing	118
Magnet shaping	120
Summary	121
<b>Sinusoidal versus trapezoidal motors</b>	121
<b>Topologies</b>	121
Radial flux	122
Axial flux	122
<b>Conclusion</b>	123
<b>Chapter 6. Design Equations</b>	125
<b>Design Approach</b>	125
<b>Radial Flux Motor Design</b>	126
Fixed parameters	126
Geometric parameters	127
Magnetic parameters	130
Electrical parameters	131
Performance	135
Design procedure	137
Summary	137
<b>Dual Axial Flux Motor Design</b>	137
Magnetic circuit analysis	137
Fixed parameters	143
Geometric parameters	144
Magnetic parameters	145
Electrical parameters	147
Performance	150
Design procedure	150
Summary	150
<b>Conclusion</b>	150

<b>Chapter 7. Motor Drive Schemes</b>	<b>155</b>
Two-Phase Motors	155
One-phase-ON operation	157
Two-phase-ON operation	158
The sine wave motor	160
H-bridge circuitry	161
Three-Phase Motors	165
Three-phase-ON operation	165
Y connection	166
$\Delta$ connection	170
The sine wave motor	173
PWM Methods	174
Hysteresis PWM	174
Clocked turn-ON PWM	175
Clocked turn-OFF PWM	176
Dual current-model PWM	177
Triangle PWM	178
Summary	179
<b>Appendix A. List of Symbols</b>	<b>183</b>
<b>Appendix B. Common Units and Equivalents</b>	<b>185</b>
<b>Bibliography</b>	<b>187</b>
<b>Index</b>	<b>189</b>

---

# Preface

You've just picked up another book on motors. You've seen many others, but they all assume that you know more about motors than you do. Phrases such as armature reaction, slot leakage, fractional pitch, and skew factor are used with little or no introduction. You keep looking for a book that is written from a more basic, yet rigorous, perspective and you're hoping this is it.

If the above describes at least part of your reason for picking up this book, then this book is for you. This book starts with basic concepts, provides intuitive reasoning for them, and gradually builds a set of understandable concepts for the design of brushless permanent-magnet motors. It is meant to be the book to read before all other motor books. Every possible design variation is not considered. Only basic design concepts are covered in depth. However, the concepts illustrated are described in such a way that common design variations follow naturally.

If the first paragraph above does not describe your reason for picking up this book, then this book may still be for you. It is for you if you are looking for a fresh approach to this material. It is also for you if you are looking for a modern text that brings together material normally scattered in numerous texts and articles many of which were written decades ago.

Is this book for you if you are never going to design a motor? By all means, yes. Although the number of people who actually design motors is very small, many more people specify and use motors in an infinite variety of applications. The material presented in this text will provide the designers of systems containing motors a wealth of information about how brushless permanent-magnet motors work and what the basic performance tradeoffs are. Used wisely, this information will lead to better engineered motor systems.

Why a book on brushless permanent-magnet motor design? This book is motivated by the ever increasing use of brushless permanent-magnet motors in applications ranging from hard disk drives to a variety of

industrial and military uses. Brushless permanent-magnet motors have become attractive because of the significant improvements in permanent magnets over the past decade, similar improvements in power electronic devices, and the ever increasing need to develop smaller, cheaper, and more energy-efficient motors. At the present time, brushless permanent-magnet motors are not the most prevalent motor type in use. However, as their cost continues to decrease, they will slowly become a dominant motor type because of their superior drive characteristics and efficiency.

Finally, what's missing from this book? What's missing is the "nuts and bolts" required to actually build a motor. There are no commercial material specifications and their suppliers given, such as those for electrical steels, permanent magnets, adhesives, wire tables, bearings, etc. In addition, this book does not discuss the variety of manufacturing processes used in motor fabrication. While this information is needed to build a motor, much of it becomes outdated as new materials and processes evolve. Moreover, the inclusion of this material would dilute the primary focus of this book, which is to understand the intricacies and tradeoffs in the magnetic design of brushless permanent-magnet motors.

I hope that you find this book useful and perhaps enlightening. If you have corrections, please share them with me, as it is impossible to eliminate all errors, especially as a sole author. I also welcome your comments and constructive criticisms about the material.

## Acknowledgments

This text would not have been possible without the generous opportunities provided by Mike and his staff. Moreover, it would not have been possible without the commitment and dedication of my wife Pamela and our children Ruth, Sarah, and Kevin.

*Duane C. Hanselman*

---

**Brushless  
Permanent-Magnet  
Motor Design**

# Basic Concepts

This chapter develops a number of basic motor concepts in a way that appeals to your intuition. By appealing to your intuition, the concepts are more likely to make sense, especially when these concepts are used for motor design in later chapters. Many of the concepts presented here apply to most motor types, since all motors are constructed of similar materials and all produce the same output, namely, torque.

## Scope

This text covers the analysis and design of rotational brushless permanent-magnet (PM) motors. Brushless dc, PM synchronous, and PM step motors are all brushless permanent-magnet motors. These specific motor types evolved over time to satisfy different application niches, but their operating principles are essentially identical. Thus the material presented in this text is applicable to all three of these motor types.

To put these motor types into perspective, it is useful to show where they fit in the overall classification of electric motors as shown in Fig. 1.1. The other motors shown in the figure are not considered in this text. Their operating principles can be found in a number of other texts.

## Shape

The most common motor shape is cylindrical, as shown in Fig. 1.2a. This motor shape and all others contain two primary parts. The non-moving, or stationary, part is called the stator. The moving, or rotating, part is called the rotor. In most cylindrical-shaped motors, the rotor appears inside the stator as shown in Fig. 1.2a. This construction is

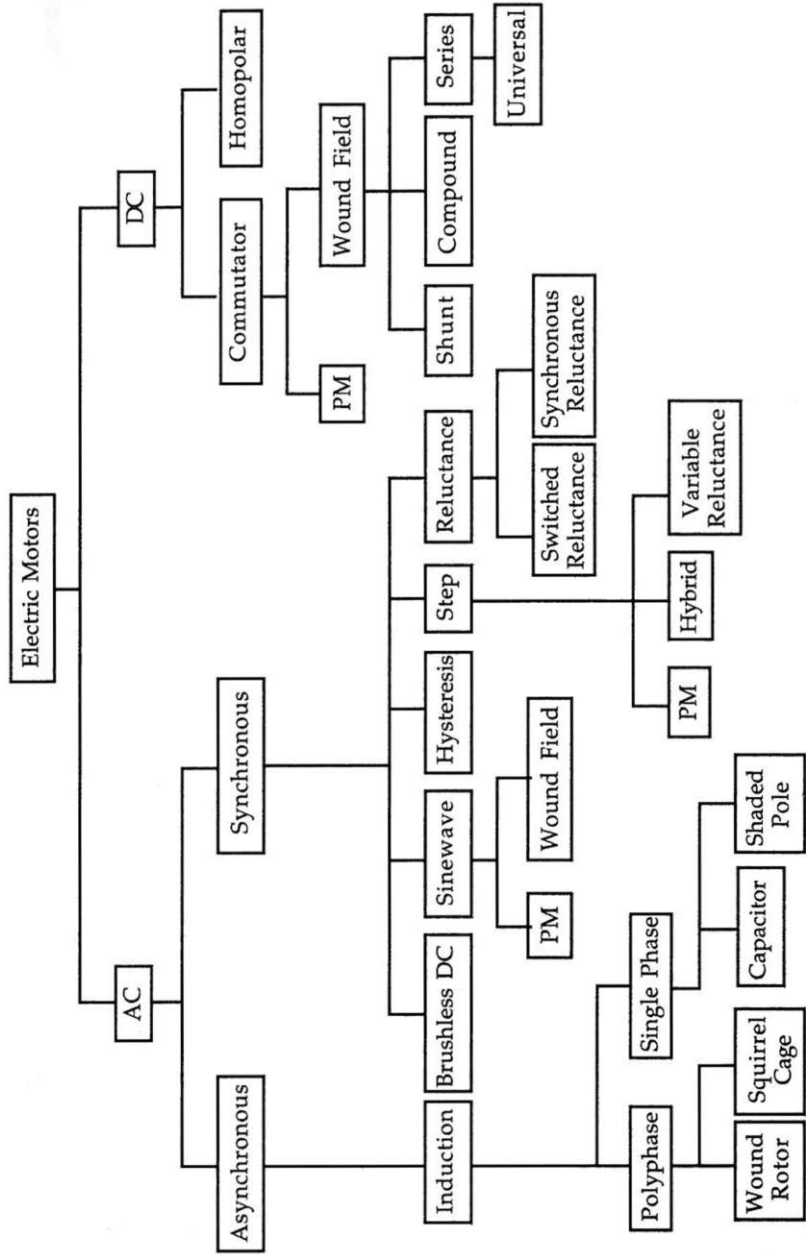


Figure 1.1 A classification of electric motors.

popular because placing the nonmoving stator on the outside makes it easy to attach the motor to its surroundings. Moreover, confining the rotor inside the stator provides a natural shield to protect the moving rotor from its surroundings.

In addition to the cylindrical shape, motors can be constructed in numerous other ways. Several possibilities are shown in Fig. 1.2. Figure 1.2a and b shows the two cylindrical shapes. When the rotor appears on the outside of the stator as shown in Fig. 1.2b, the motor is often said to be an “inside-out” motor. For these motors a magnetic field travels in a radial direction across the air gap between the rotor and stator. As a result, these motors are called radial flux motors. Motors having a pancake shape are shown in Fig. 1.2c and d. In these motors the magnetic field between the rotor and stator travels in the axial direction. Thus these motors are called axial flux motors.

Brushless PM motors can be built in all the shapes shown in Fig. 1.2 as well as in a number of other more creative shapes. All brushless

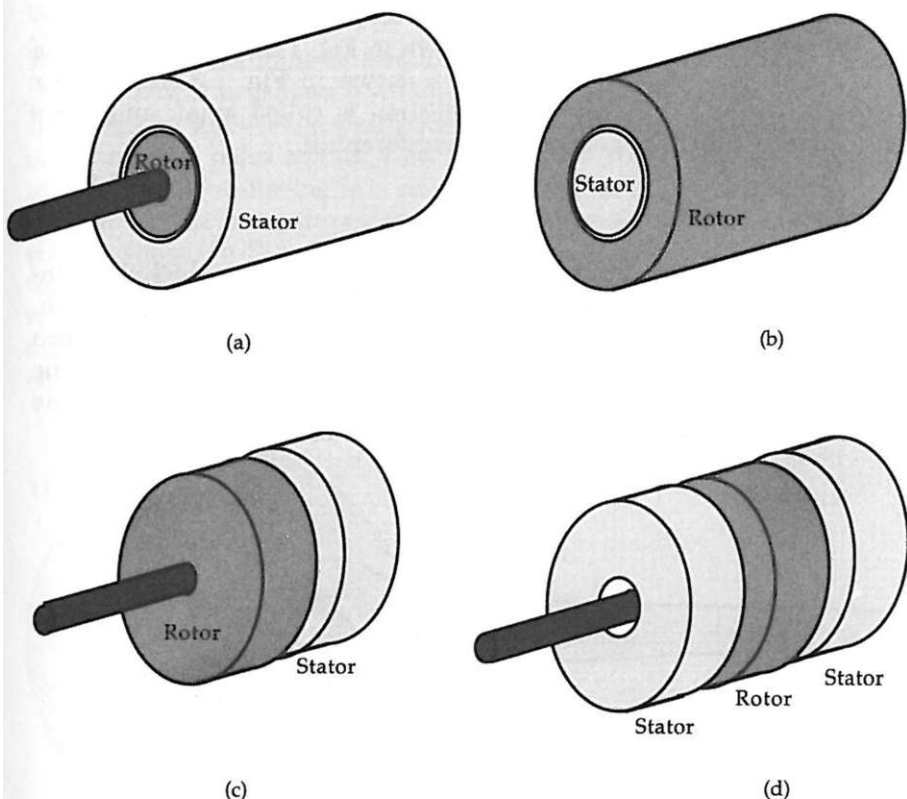


Figure 1.2 Motor construction possibilities.

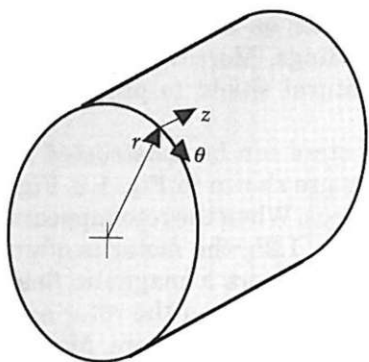


Figure 1.3 The cylindrical coordinate system.

PM motors are constructed with electrical windings on the stator and permanent magnets on the rotor. This construction is one of the primary reasons for the increasing popularity of brushless PM motors. Because the windings remain stationary, no potentially troublesome moving electrical contacts, i.e., brushes, are required. In addition, because the windings are stationary it is easier to keep them cool.

The common cylindrical shape shown in Fig. 1.2 leads to the use of the cylindrical coordinate system as shown in Fig. 1.3. Here the  $r$  direction is called radial, the  $z$  direction is called axial, and the  $\theta$  direction is called tangential or circumferential.

## Torque

All motors produce torque. Torque is given by the product of a tangential force acting at a radius, and thus has units of force times length, e.g., oz·in, lb·ft, N·m. To understand this concept, consider the wrench and nut shown in Fig. 1.4. If a force  $F$  is applied to the wrench in the tangential direction at a distance  $r$  from the center of the nut, the twisting force, or torque, experienced by the bolt is

$$T = Fr \quad (1.1)$$

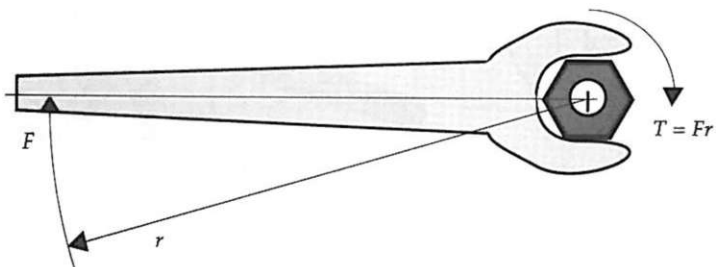


Figure 1.4 A wrench on a nut.

This relationship implies that if the length of the wrench is doubled and the same force is applied at a distance  $2r$ , the torque experienced by the nut is doubled. Likewise, shortening the wrench by a factor of 2 and applying the same force cuts the torque in half. Thus a fixed force produces the most torque when the radius at which it is applied is maximized. Furthermore, it is only force acting in the tangential direction that creates torque. If the force is applied in an outwardly radial direction, the wrench simply comes off the nut and no torque is experienced by the nut. Taking the direction of applied force into account, torque can be expressed as  $T = Fr \sin \theta$ , where  $\theta$  is the angle at which the force is applied with respect to the radial direction.

Certainly this concept of torque makes sense to anyone who has tried to loosen a rusted nut. The longer the wrench, the less force required to loosen the nut. And the force applied to the wrench is most efficient when it is in the circumferential direction, i.e., in the direction tangential to a circle centered over the nut as shown in the figure.

### **Motor Action**

With an understanding of torque production, it is now possible to illustrate how a brushless PM motor works. All that's required is the rudimentary knowledge that magnets are attracted to iron, that opposite magnet poles attract, that like magnet poles repel each other, and that current flowing in a coil of wire makes an electromagnet.

Consider the bar permanent magnet centered in a stationary iron ring as shown in Fig. 1.5, where the bar magnet in the figure is free to spin about its center but is otherwise fixed. Here the magnet is the rotor and the iron ring is the stator. As shown in the figure, the magnet does not have any preferred resting position. Each end experiences an equal but oppositely directed radial force of attraction to the ring that

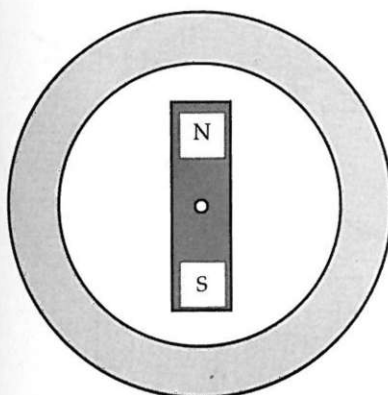
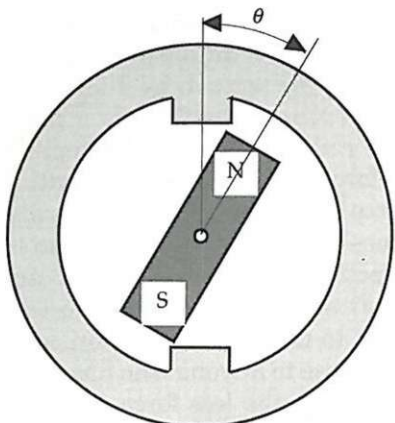


Figure 1.5 A magnet free to spin inside a steel ring.



**Figure 1.6** A magnet free to spin inside a steel ring having two poles.

is not a function of the particular direction of the magnet. The magnet experiences no net force and thus no torque is produced.

Next consider changing the iron ring so that it has two protrusions or poles on it as shown in Fig. 1.6. As before, each end of the magnet experiences an equal but oppositely directed radial force. Now, however, if the magnet is spun slowly it will have the tendency to come to rest in the  $\theta = 0$  position shown in the figure. That is, as the magnet spins it will experience a force that will try to align the magnet with the stator poles. This occurs because the force of attraction between a magnet and iron increases dramatically as the physical distance between the two decreases. Because the magnet is free to spin, this force is partly in the tangential direction, and torque is produced.

Figure 1.7 depicts this torque graphically as a function of motor position. The positions where the force or torque is zero are called detent

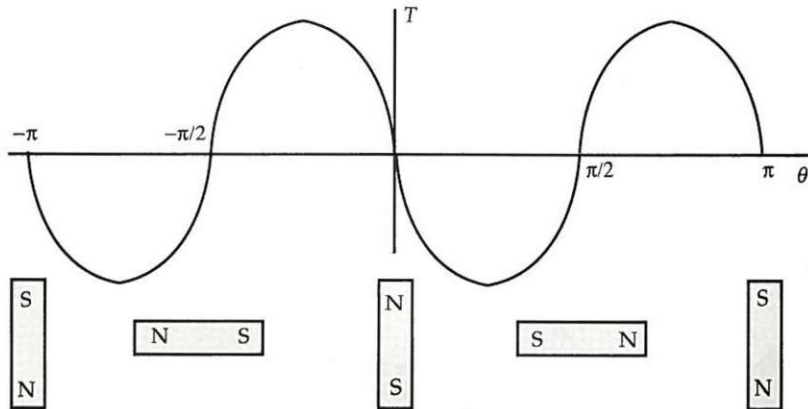


**Figure 1.7** Torque experienced by the magnet in Fig. 1.6.

positions. When the magnet is aligned with the poles, any small disturbance causes the magnet to restore itself to the same aligned position. Thus these detent positions are said to be stable. On the other hand, when the magnet is halfway between the poles, i.e., unaligned, any small disturbance causes the magnet to move away from the unaligned position and seek alignment. Thus unaligned detent positions are said to be unstable. While the shape of the detent torque is approximately sinusoidal in Fig. 1.7, in a real motor its shape is a complex function of motor geometry and material properties.

The torque described here is formally called reluctance torque. In most brushless permanent-magnet motors this torque is undesirable and is given the special names of cogging torque or detent torque.

Now consider the addition of current-carrying coils to the poles as shown in Fig. 1.8. If current is applied to the coils, the poles become electromagnets. In particular, if the current is applied in the proper direction, the poles become magnetized as shown in Fig. 1.8. In this situation, the force of attraction between the bar magnet and the opposite electromagnet poles creates another type of torque, formally called mutual or alignment torque. It is this torque that is used in brushless PM motors to do work. The term mutual is used because it is the mutual attraction between the magnets that produces torque. The term alignment is used because the force of attraction seeks to align the bar magnet and coil-wound poles.

This torque could also be called repulsion torque, since if the current is applied in the opposite direction, the poles become magnetized in the opposite direction, as shown in Fig. 1.9. In this situation the like poles repel, sending the bar magnet in the opposite direction. Since both of these scenarios involve the mutual interaction of the magnets, the torque mechanism is identical and the term repulsion torque is not used.

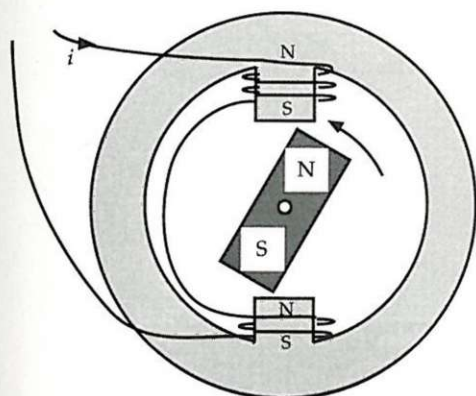
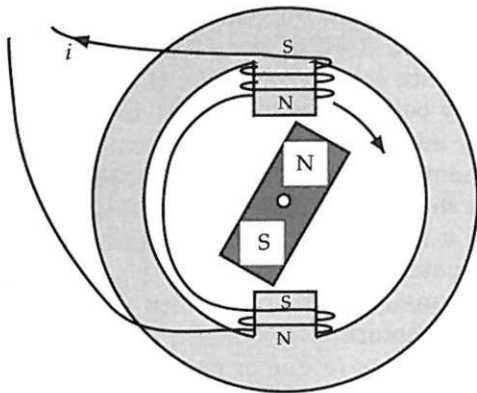


Figure 1.8 Current-carrying windings added to Fig. 1.6.



**Figure 1.9** Current flow in the opposite direction compared with Fig. 1.8.

To get the bar magnet to turn continuously, it is common to employ more than one set of coils. Figure 1.10 shows the case where three sets of coils are used; i.e., there are three motor phases labeled *A*, *B*, and *C* in the figure. By creating electromagnet poles on the stator that attract and/or repel those of the bar magnet, the bar magnet can be made to rotate by successively energizing and deenergizing the phases. This action of the rotor chasing after the electromagnet poles on the stator is the fundamental motor action involved in brushless PM motors.

### Magnet Poles and Motor Phases

Although the motor depicted in Fig. 1.10 has two rotor magnet poles and three stator phases, it is possible to build brushless PM motors with any even number of rotor magnet poles and any number of phases greater than or equal to 2. Two- and three-phase motors are the most

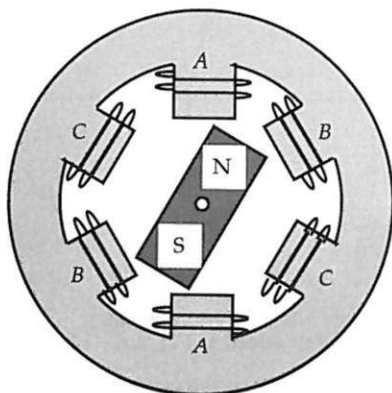


**Figure 1.10** Motor structure having three phases.

common, with three-phase motors dominating all others. The reason for these choices is that two- and three-phase motors minimize the number of power electronic devices required to control the winding currents.

The choice of magnet poles offers more flexibility. Brushless PM motors have been constructed with two to fifty or more magnet poles, with the most common being two- and four-magnet poles. As will be shown later, a greater number of magnet poles usually creates a greater torque for the same current level. On the other hand, more magnet poles implies having less room for each pole. Eventually, a point is reached where the spacing between rotor magnet poles becomes a significant percentage of the total room on the rotor and torque no longer increases. The optimum number of magnet poles is a complex function of motor geometry and material properties. Thus in many designs, economics dictates that a small number of magnet poles be used.

### Poles, Slots, and Teeth

The motor in Fig. 1.10 has concentrated solenoidal windings. That is, the windings of each phase are isolated from each other and concentrated around individual poles called salient poles in much the same way that a simple solenoid is wound. A more common alternative to this construction is to overlap the phases and let them share the same stator area, as shown in Fig. 1.11. Furthermore, it is more common to use magnet arcs or pieces distributed around an iron rotor disk for the rotor, as shown in the figure. Here the rotor is shown with four magnet poles and the stator phase *B* and *C* windings are distributed on top of the phase *A* windings. When constructed in this way, the areas occupied by the windings are called slots and the iron areas between the slots are called teeth. The principle of operation remains the same: The

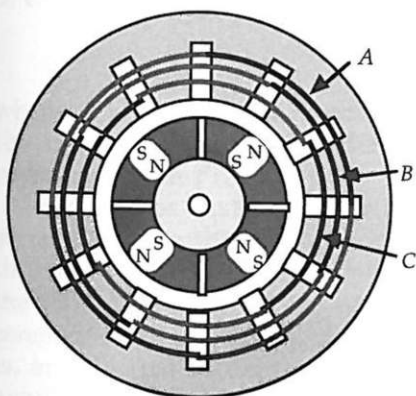


Figure 1.11 Slotted three-phase motor structure.

phase windings are energized and deenergized in turn to create electromagnet poles on the stator that attract and/or repel the rotor magnet poles.

### Mechanical and Electrical Measures

In electric motors it is common to define two related measures of position and speed. Mechanical position and speed are the respective position and speed of the rotor output shaft. When the rotor shaft makes one complete revolution, it traverses 360 mechanical degrees ( $2\pi$  mechanical radians). Having made this revolution, the rotor is right back where it started.

Electrical position is defined such that movement of the rotor by 360 electrical degrees ( $2\pi$  electrical radians) puts the rotor back in an identical magnetic orientation. In Fig. 1.10, mechanical and electrical position are identical since the rotor must rotate 360 mechanical degrees to reach the same magnetic orientation. On the other hand, in Fig. 1.12 the rotor need only move 180 mechanical degrees to have the same magnetic orientation. Thus 360 electrical degrees is the same as 180 mechanical degrees for this case. Based on these two cases, it is easy to see that the relationship between electrical and mechanical position is related to the number of magnet poles on the rotor. If  $N_m$  is the number of magnet poles on the rotor facing the air gap, i.e.,  $N_m = 2$  for Fig. 1.10 and  $N_m = 4$  for Fig. 1.12, this relationship can be stated as

$$\theta_e = \frac{N_m}{2} \theta_m \quad (1.2)$$

where  $\theta_e$  and  $\theta_m$  are electrical and mechanical position, respectively.

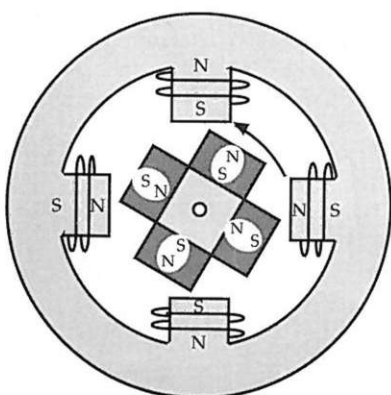


Figure 1.12 Motor structure having four magnet poles.

Since magnets always have two poles, some texts define a pole pair as one north and one south magnet pole facing the air gap. In this case, the number of pole pairs is equal to  $N_p = N_m/2$ , and the above relationship is simply  $\theta_e = N_p \theta_m$ .

Differentiating (1.2) with respect to time gives the relationship between electrical and mechanical frequency or speed as

$$\omega_e = \frac{N_m}{2} \omega_m \quad (1.3)$$

where  $\omega_e$  and  $\omega_m$  are electrical and mechanical frequencies, respectively, in radians per second. This relationship can also be stated in terms of hertz as  $f_e = (N_m/2)f_m$ . Later, when harmonics of  $f_e$  are discussed,  $f_e$  will be called the fundamental electrical frequency.

It is common practice to specify motor mechanical speed  $S$  in terms of revolutions per minute (rpm). For reference, the relationships among  $S$ ,  $\omega_m$ , and  $f_m$  are given by

$$\begin{aligned} \omega_m &= \frac{\pi}{30} S \\ f_m &= \frac{\omega_m}{2\pi} = \frac{S}{60} \end{aligned} \quad (1.4)$$

These relationships, taken with (1.3), allow one to further relate  $S$  to  $\omega_e$  and  $f_e$  as required.

## Motor Size

A fundamental question in motor design is "How big does a motor have to be to produce a required torque?" For radial flux motors the answer to this question is often stated as

$$T = kD^2L \quad (1.5)$$

where  $T$  is torque,  $k$  is a constant,  $D$  is the rotor diameter, and  $L$  is the axial rotor length. To understand this relationship, reconsider the motor shown in Fig. 1.10.

First assume that the motor has an axial length (depth into page) equal to  $L$ . For this length, a certain torque  $T_L$  is available. Now if this motor is duplicated, added to the end of the original motor, and the rotor shafts are connected together, the total torque available becomes the sum of that from each motor, namely,  $T = T_L + T_L$ . That is, an effective doubling of the axial rotor length to  $2L$  doubles the available torque. Thus torque is linearly proportional to  $L$ .

Understanding the  $D^2$  relationship requires a little more effort. In the discussion of the wrench and nut shown in Fig. 1.4, it was shown that a given force produces a torque that is proportional to radius ( $D/2$ ). Therefore, torque is at least linearly proportional to diameter. However, it can be argued that the ability to produce force is also linearly proportional to diameter. This follows because the available rotor perimeter increases linearly with diameter; e.g., the circumference of a circle is equal to  $\pi D$ . A simple way to see this relationship is to compare the simple motor in Fig. 1.8 with that in Fig. 1.12. If the motor in Fig. 1.8 produces a torque  $T_L$ , then the motor in Fig. 1.12 should produce a torque equal to  $2T_L$  because twice the magnets are producing twice the force. Clearly as diameter increases, there is more and more room for magnets around the rotor. So it makes sense that the ability to produce force increases linearly with diameter. Combining these two contributing factors leads to the desired relationship that torque is proportional to diameter squared.

## Conclusion

This chapter developed the basic concepts involved in brushless PM motor design. Both radial flux and axial flux shapes were described. The relationship between torque and force was developed and basic properties of magnets were used to intuitively describe how a motor works. Along the way, the ideas of poles, phases, slots, and teeth were introduced. The commonly held  $D^2L$  sizing relationship was also justified intuitively. The purpose of the remaining chapters of this text is to use and expand the intuition gained in this chapter to develop quantitative expressions describing motor performance. Of particular interest is an expression for the torque produced in a brushless PM motor.

## Magnetic Modeling

Brushless PM motor operation relies on the conversion of energy from electrical to magnetic to mechanical. Because magnetic energy plays a central role in the production of torque, it is necessary to formulate methods for computing it. Magnetic energy is highly dependent upon the spatial distribution of a magnetic field, i.e., how it is distributed within an apparatus. For brushless PM motors this means finding the magnetic field distribution within the motor.

There are numerous ways to determine the magnetic field distribution within an apparatus. For very simple geometries, the magnetic field distribution can be found analytically. However, in most cases, the field distribution can only be approximated. Magnetic field approximations appear in two general forms. In the first, the direction of the magnetic field is assumed known everywhere within the apparatus. This leads to magnetic circuit analysis, which is analogous to electric circuit analysis. In the other form, the apparatus is discretized geometrically and the magnetic field is numerically computed at discrete points in the apparatus. From this information, the magnitude and direction of the magnetic field can be approximated throughout the apparatus. This approach is commonly called finite element analysis, and it embodies a variety of similar mathematical methods known as the finite difference method, the finite element method, and the boundary element method.

Of these two magnetic field approximations, finite element analysis produces the most accurate results if the geometric discretization is fine enough. However, this accuracy comes with a significant computational cost. Despite the ever-increasing capabilities of computers, a typical finite element analysis solution takes from tens of minutes to more than an hour. This time is in addition to the many hours or days

needed to generate the initial discretized geometric model. In addition to the time involved, finite element analysis produces a purely numerical solution. The solution is typically composed of the potential at hundreds or thousands of points within the apparatus. The geometrical parameters and the resulting change in the magnetic field distribution are not related analytically. Thus many finite element solutions are usually required to develop basic insight into the effect of various parameters on the magnetic field distribution. Because of these disadvantages, finite element analysis is not used extensively as a design tool. Rather it is most often used to confirm or improve the results of analytical design work. Finite element analysis provides microscopic detail in a problem where it is more important to have macroscopic information to predict performance.

As opposed to the complexity and numerical nature of finite element analysis, the simplicity and analytic properties of magnetic circuit analysis make it the most commonly used magnetic field approximation method. By making the assumption that the direction of the magnetic field is known throughout an apparatus, magnetic circuit analysis allows one to approximate the field distribution analytically. Because of this analytical relationship, the geometry of a problem is clearly related to its field distribution, thereby providing substantial design insight. A major weakness of the magnetic circuit approach is that it is often difficult to determine the magnetic field direction throughout an apparatus. Moreover, predetermining the magnetic field direction requires subjective foresight that is influenced by the experience of the person using magnetic circuit analysis. Despite these weaknesses, magnetic circuit analysis is very useful for designing brushless PM motors. For this reason, magnetic circuit analysis concepts are developed in this chapter.

## Magnetic Circuit Concepts

### Basic relationships

Two vector quantities  $B$  and  $H$  describe a magnetic field. The flux density  $B$  can be thought of as the amount of magnetic field flowing through a given area of material, and the field intensity  $H$  is the resulting change in the intensity of the magnetic field due to the interaction of  $B$  with the material it encounters. For magnetic materials common to motor design,  $B$  and  $H$  are collinear. That is, they are oriented in the same direction within a given material. Figure 2.1 illustrates these relationships for a differential size block of material. In this figure,  $B$  is directed perpendicularly through the block in the  $z$  direction, and  $H$  is the change in the field intensity in the  $z$  direction. In general, the relationship between  $B$  and  $H$  is a nonlinear, multi-

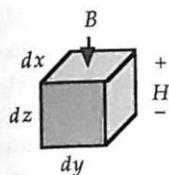


**Figure 2.1** Differential size block of magnetic material.

valued function of the material. However, for many materials this relationship is linear or nearly linear over a sufficiently large operating range. In this case,  $B$  and  $H$  are linearly related and written as

$$B = \mu H \quad (2.1)$$

where  $\mu$  is the permeability of the material.

Magnetic circuit analysis is based on the assumptions of material linearity and the collinearity of  $B$  and  $H$ . Two fundamental equations lead to magnetic circuit analysis. One of these relates flux density to flux, and the other relates field intensity to magnetomotive force (mmf).

To develop magnetic circuit analysis, let the material in Fig. 2.1 be linear and let the cross-sectional area exposed to the magnetic flux density  $B$  grow to a nondifferential size as shown in Fig. 2.2. The total flux  $\phi$  flowing perpendicularly into this volume is the sum of that flowing into each differential cross section. Hence  $\phi$  can be written as the integral

$$\phi = \int B_z(x, y) dx dy \quad (2.2)$$

For the common situation where  $B_z(x, y) = B$  is constant over the cross section, this integral can be simplified as

$$\phi = BA \quad (2.3)$$

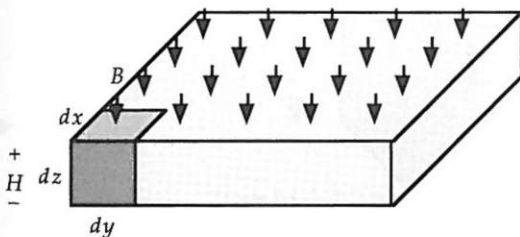


**Figure 2.2** Magnetic material having a differential length.

where  $A$  is the cross-sectional area. In the International System of Units (SI),  $B$  is given in webers per meter squared ( $\text{Wb}/\text{m}^2$ ) or tesla ( $T$ ). Thus flux  $\phi$  is given by webers ( $\text{Wb}$ ). This equation forms the first fundamental equation of magnetic circuit analysis. In Fig. 2.2, the change in the field intensity across the block remains equal to  $H$ , as each differential cross section making up the entire block has a field intensity of  $H$  and all cross sections are in parallel with each other.

Next, consider stretching the block in the  $z$  direction as shown in Fig. 2.3. As the block is stretched in the  $z$  direction, the flux  $\phi$  flows through each succeeding layer of thickness  $dz$ , creating a change in the magnetic field intensity of  $H$  for each layer. Thus the total change in the field intensity is

$$F = \int H dz = Hl \quad (2.4)$$

where  $F$  is defined as mmf and  $l$  is the length of the block in the  $z$  direction. The SI unit of  $H$  is amperes per meter ( $\text{A/m}$ ), and thus mmf has the unit of amperes ( $\text{A}$ ). Equation (2.4) defines the second fundamental equation of magnetic circuit analysis.

Connecting these two fundamental equations is the material characteristic given in (2.1). Substituting (2.3) and (2.4) into (2.1) and rearranging gives

$$\phi = PF \quad (2.5)$$

where

$$P = \frac{\mu A}{l} \quad (2.6)$$

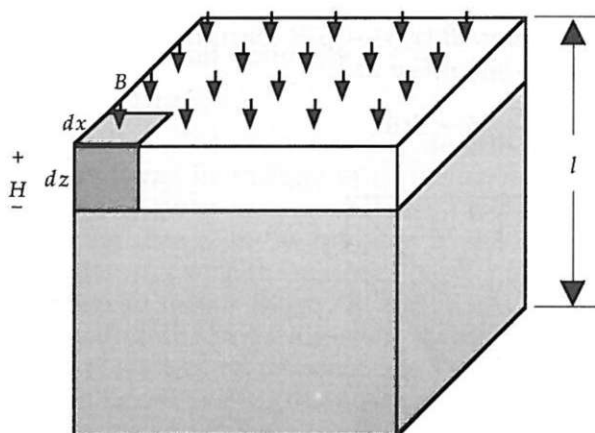


Figure 2.3 A block of magnetic material.

is defined as the permeance of the material having a cross-sectional area  $A$ , length  $l$ , and permeability  $\mu$ . The unit of permeance is webers per ampere (Wb/A) or henries (H). Materials having higher permeability have greater permeance and therefore promote greater flux flow through them.

Equation (2.5) is analogous to Ohm's law,  $I = GV$ . Flux flows in closed paths, just as current does;  $F$  is magnetomotive force (mmf), just as voltage is electromotive force (emf), and the conductance of a rectangular block of resistive material is identical to the permeance equation (2.6), with conductivity replacing permeability.

The inverse of permeance is reluctance and is given by

$$R \equiv \frac{1}{P} = \frac{l}{\mu A} \quad (2.7)$$

In terms of reluctance, (2.5) can be rewritten as

$$F = \phi R \quad (2.8)$$

which is analogous to Ohm's law written as  $V = IR$ , with reluctance being analogous to resistance. At this point the analogy between electric and magnetic circuits ends because current flow through a resistance constitutes energy dissipation, whereas flux flow through a reluctance constitutes energy storage.

### Magnetic field sources

There are two common sources of magnetic fields, one being current flowing in a wire, the other being a PM. Postponing PMs until later, consider a coil of wire wrapped about a piece of highly permeable material, called a core, as shown in Fig. 2.4. Current flowing through the coil produces a magnetic field that can be found by applying Ampère's law. This law is stated as the line integral

$$\oint_C H \cdot dl = \begin{cases} I, & \text{if } C \text{ encloses } I \\ 0, & \text{if } C \text{ does not enclose } I \end{cases} \quad (2.9)$$

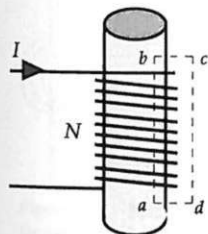


Figure 2.4 A coil wrapped around a piece of magnetic material.

where  $C$  is any closed path or contour. In this expression,  $H \cdot dl$  is the vector dot product between the field intensity and a differential line segment  $dl$  on the contour  $C$ . The direction of  $H$  with respect to the current  $I$  is related by the right-hand screw rule: *Positive current is defined as flowing in the direction of the advance of a right-hand screw turned in the direction in which the closed path is traversed.* Alternately, the magnetic field produced by a current flowing in a wire has its direction defined by the right-hand rule as illustrated in Fig. 2.5.

Application of the above relationship to the contour enclosing  $N$  turns carrying a current of  $I$  A as shown in Fig. 2.4 gives

$$NI = \int_a^b H_{ab} \cdot dz + \int_b^c H_{bc} \cdot dr + \int_c^d H_{cd} \cdot (-dz) + \int_d^a H_{da} \cdot (-dr)$$

where  $H_{xy}$  is the component of the field intensity coincident with the  $xy$  section of the contour. If the core has infinite permeability, it can be shown that the magnetic field is confined to the core and has a  $z$  direction component only. For finite permeabilities much greater than that of the surrounding material, the field is essentially confined to the core also; thus all terms in the above equation, except the first, are zero. Using this assumption, the above simplifies to

$$NI = \int_a^b H dz = Hl \quad (2.10)$$

where  $N$  is the number of turns enclosed and  $l = |b - a|$ . Since the product  $Hl$  is an mmf according to (2.4), (2.10) implies that a coil of wire is modeled as an mmf source of value  $F = NI$ . This mmf source is analogous to a voltage source in electric circuits. The fact that mmf is given by the product of a current and a number of turns leads to the conventional units of ampere-turns for mmf. However, since turns is dimensionless, it is ignored in SI units, giving mmf units of amperes, as discussed previously.

It is important to note that the value of the mmf source is not a function of the length of the cylinder taken up by the coil. The cylinder

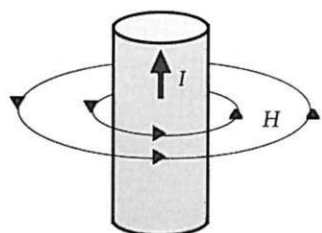
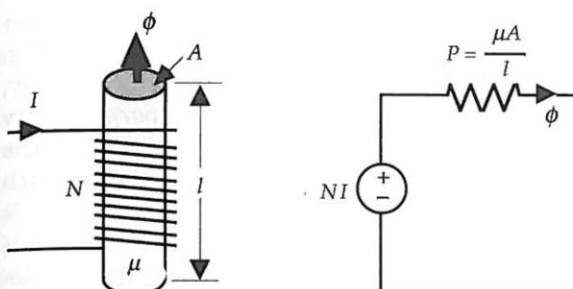


Figure 2.5 The magnetic field about a conductor.



**Figure 2.6** Magnetic circuit model of a coil.

itself must be modeled as a reluctance or permeance, as described earlier. Hence a practical winding about a core is modeled as an mmf source in series with a permeance, as shown in Fig. 2.6.

### Air gap modeling

In all motors, flux passes between the rotor and stator through an air gap. For this reason it is important to model the permeance or reluctance of an air gap. Consider the structure shown in Fig. 2.7, where an air gap is created between two blocks of highly permeable material. Flux flowing from one block to the other passes through the air gap and creates an mmf drop between the two blocks. The permeance of this air gap  $P_g$  is difficult to model because flux does not flow straight across the air gap near the edges of the blocks. This occurs because the air in the gap has the same permeability as the air fringing the gap; therefore, some flux will flow in the fringe area as shown in Fig. 2.7. The permeance of the gap depends on the exact magnetic field distribution in the gap. While this can be accurately approximated using finite element methods, it is possible to approximate the air gap permeance with sufficient accuracy for most applications using magnetic circuit concepts.

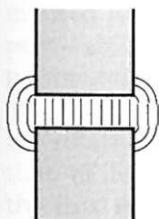


**Figure 2.7** Magnetic flux flow in an air gap between two highly permeable structures.

Depending on the degree of precision required, there are a number of techniques for modeling flux flow in an air gap as depicted in Fig. 2.8. The simplest model (Fig. 2.8a) ignores the fringing flux entirely, giving  $P_g = \mu_0 A/g$ , where  $g$  is the air gap length,  $\mu_0$  is the permeability of free space ( $4\pi \cdot 10^{-7}$  H/m), and  $A$  is the cross-sectional area of the blocks facing the air gap. A refinement of this model (Fig. 2.8b) which is accurate when  $g/A$  is small lets  $P_g = \mu_0 A'/g$ , where the length  $g$  is added to the perimeter of  $A$  to obtain  $A'$ . Yet another refinement models the fringing flux as a separate permeance in parallel with the permeance of the direct flux path across the air gap. One method for doing this is shown in Fig. 2.8c. In this figure, the fringing flux is assumed to follow a circular arc from the side of one block, travel in a straight line across the gap area, then follow a circular arc to the other block. This technique was introduced by Roters (1941) and popularized by Chai (1973).

The calculation of the air gap permeance using this circular-arc, straight-line approximation utilizes the fact that permeances add in parallel just as electrical conductances do. The air gap permeance  $P_g$  in Fig. 2.9 is equal to the sum of  $P_s$  and  $4P_f$  (one  $P_f$  for each side of the block). While the straight-line permeance  $P_s$  is computed using (2.6), the fringing permeance  $P_f$  requires more work. As depicted in Fig. 2.9,  $P_f$  is an infinite sum of differential width permeances, each of length  $g + \pi x$ . That is,

$$P_f = \sum \frac{\mu_0 dA}{l} = \sum \frac{\mu_0 L dx}{g + \pi x}$$

where  $dA = L dx$  is the cross-sectional area of each differential permeance and  $L$  is the depth of the block into the page. Because this equation involves the sum of differential elements, its solution is given by the integral

$$P_f = \int_0^X \frac{\mu_0 L}{g + \pi x} dx = \frac{\mu_0 L}{\pi} \ln \left( 1 + \frac{\pi X}{g} \right) \quad (2.11)$$

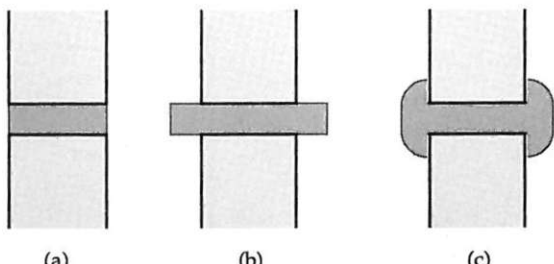
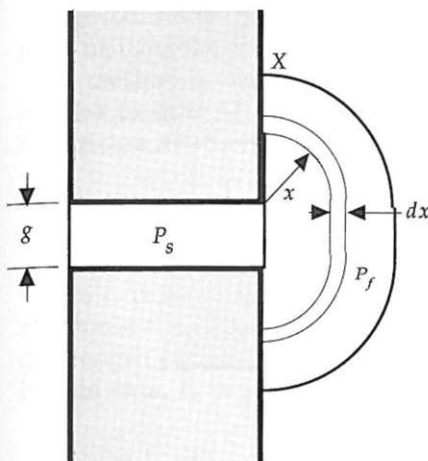


Figure 2.8 Air gap permeance models.



**Figure 2.9** Circular-arc, straight-line permeance model.

In this equation,  $X$ , the extent that the fringing permeance extends up the sides of the blocks, is the only unknown. In those cases where  $X$  is not fixed by geometric constraints, it is commonly chosen to be some multiple of the air gap length. The exact value chosen is not that critical because the contribution of differential permeances decreases as one moves farther from the air gap. Thus as  $X$  increases beyond about 10 $g$ , there is little change in the total air gap permeance.

### Slot modeling

Often electrical machines have slots facing an air gap which hold current-carrying windings. Since the windings are nonmagnetic, flux crossing an air gap containing slots will try to avoid the low relative permeability of the slot area. This adds another factor that must be considered in determining the permeance of an air gap.

To illustrate this point, consider Fig. 2.10a, where slots have been placed in the lower block of highly permeable material. Considering just one slot and the tooth between the slots, there are several ways to approximate the air gap permeance. The simplest and crudest method is to ignore the slot by assuming that it contains material of permeability equal to that of the rest of the block. In this case, the permeability is simply  $P_g = \mu_0 A/g$ , where  $A$  is the total cross-sectional area facing the gap. Obviously, this is a poor approximation because the relative permeability of the slot is orders of magnitude lower than that of block material. Another crude approximation is to ignore the flux crossing the gap over the slot, giving a permeance of  $P_g = \mu_0(A - A_s)/g$ , where  $A_s$  is the cross-sectional area of the slot facing the air gap. Neither of these methods is very accurate, but they do represent upper and lower bounds on the air gap permeance, respectively.

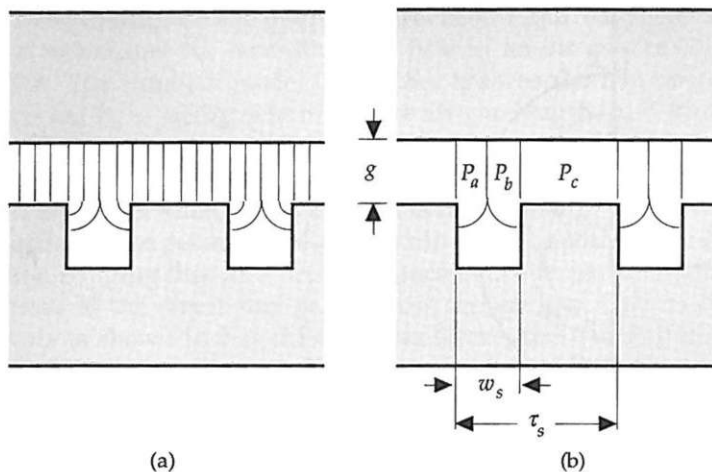


**Figure 2.10** A slotted structure.

There are two more accurate ways of determining air gap permeance in the presence of slotting. The first is based on the observation that the flux crossing the gap over the slot travels a further distance before reaching the highly permeable material across the gap. As a result, the permeance can be written as  $P_g = \mu_0 A / g_e$ , where  $g_e = g k_c$  is an effective air gap length. Here  $k_c > 1$  is a correction factor that increases the entire air gap length to account for the extra flux path distance over the slot. One approximation for  $k_c$  is known as Carter's coefficient (Mukherji and Neville, 1971; Qishan and Hongzhan, 1985). By applying conformal mapping techniques, Carter was able to determine an analytic magnetic field solution for the case where slots appear on both sides of the air gap. Through symmetry considerations it can be shown that the Carter coefficient for the aligned case, i.e., when the slots are directly opposite each other, is an acceptable approximation to the geometry shown in Fig. 2.10a. Two expressions for Carter's coefficient are

$$k_{c1} = \left[ 1 - \frac{1}{\frac{\tau_s}{w_s} \left( 5 \frac{g}{w_s} + 1 \right)} \right]^{-1} \quad (2.12)$$

given by Nasar (1987), and

$$k_{c2} = \left( 1 - \frac{2w_s}{\pi\tau_s} \left\{ \tan^{-1} \left( \frac{w_s}{g} \right) - \frac{g}{2w_s} \ln \left[ 1 + \left( \frac{w_s}{g} \right)^2 \right] \right\} \right)^{-1} \quad (2.13)$$

given by Ward and Lawrenson (1977).

The other more accurate method for determining the air gap permeance utilizes the circular-arc, straight-line modeling discussed earlier. This method is demonstrated in Fig. 2.10b. Following an approach similar to that described in (2.11), the permeance of the air gap can be written as

$$P_g = P_a + P_b + P_c = \mu_0 L \left[ \frac{\tau_s - w_s}{g} + \frac{4}{\pi} \ln \left( 1 + \frac{\pi w_s}{4g} \right) \right]$$

where  $L$  is the depth of the block into the page. With some algebraic manipulation, this solution can also be written in the form of an air gap length correction factor, as described in the preceding paragraph. In this case,  $k_c$  is given by

$$k_{c3} = \left[ 1 - \frac{w_s}{\tau_s} + \frac{4g}{\pi\tau_s} \ln \left( 1 + \frac{\pi w_s}{4g} \right) \right]^{-1} \quad (2.14)$$

A comparison of (2.12), (2.13), and (2.14) shows that all produce similar air gap length correction factors. As illustrated in Fig. 2.11,  $k_{c2}$  gives a larger correction factor than  $k_{c3}$  and  $k_{c3}$  gives a larger correction factor than  $k_{c1}$ , with the deviation among the expressions increasing as  $g/\tau_s$  decreases and  $w_s/\tau_s$  increases.

One important consequence of slotting shown in Fig. 2.12 is that the presence of slots squeezes the air gap flux into a cross-sectional area  $(1 - w_s/\tau_s)$  times smaller than the cross-sectional area of the entire air gap. Thus the average flux density at the base of the teeth is greater

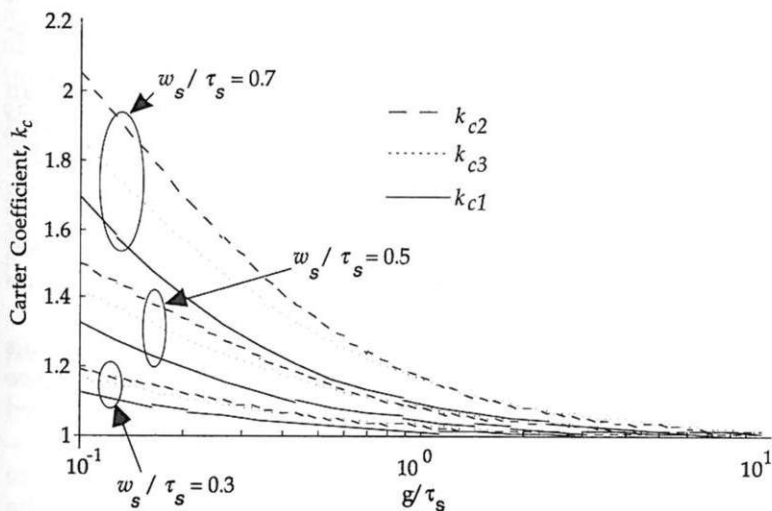
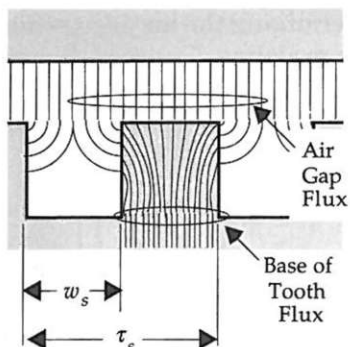


Figure 2.11 A comparison of various carter coefficients.



**Figure 2.12** Flux squeezing at the base of a tooth.

by a factor of  $(1 - w_s/\tau_s)^{-1}$ . The importance of this phenomenon cannot be understated. For example, if the average flux density crossing the air gap is 1.0 T and slot fraction  $\alpha_s = w_s/\tau_s$  is 0.5, then the average flux density in the base of the teeth is  $(1.0)(1 - 0.5)^{-1} = 2.0$  T. Since this flux density level is sufficient to saturate (i.e., dramatically reduce the effective permeability of) most magnetic materials, there is an upper limit to the achievable air gap flux density in a motor. Later this will be shown to be a limiting factor in motor performance.

### Example

The preceding discussion embodies the basic concepts of magnetic circuit analysis. Application of these concepts requires making assumptions about magnetic field direction, flux path lengths, and flux uniformity over cross-sectional areas. To illustrate magnetic circuit analysis, consider the wound core shown in Fig. 2.13a and its corresponding magnetic circuit diagram in Fig. 2.13b.

Assuming that the permeability of the core is much greater than that of the surrounding air, the magnetic field is essentially confined to the core, except at the air gap. Comparing Figs. 2.13a with 2.13b, the coil is represented by the mmf source of value  $NI$ . The reluctance of the core material is modeled by the reluctance  $R_c = l_c/\mu A$ , where  $l_c$  is the average length of the core from one side of the air gap around to the other,  $\mu$  is the permeability of the core material, and  $A$  is the cross-sectional area of the core. This modeling approximates the flux path length around bends as having median length. It also assumes that the flux density is uniform over the cross section.  $R_g$ , the reluctance of the air gap, is given by the inverse of the air gap permeance discussed earlier.

Table 2.1 shows solutions of this magnetic circuit example for the three air gap models discussed earlier. The first row corresponds to the model shown in Fig. 2.8a, the second row to Fig. 2.8b, and the third

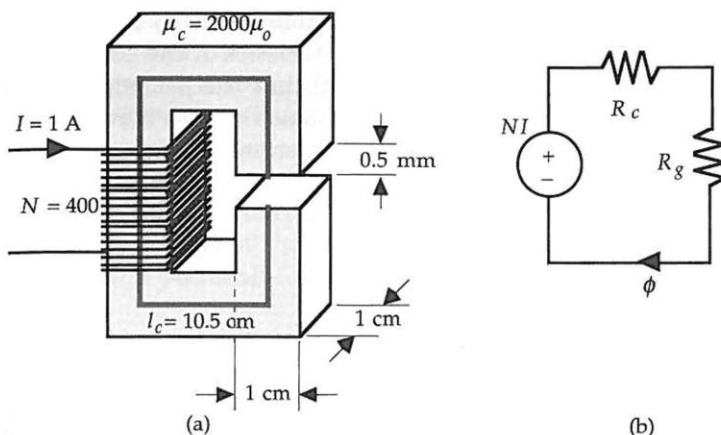


Figure 2.13 A simple magnetic structure and its magnetic circuit model.

row to Fig. 2.8c, with the fringe permeance having a width ten times larger than the air gap. The second column in the table is the air gap reluctance, the third column is the core reluctance, the fourth is the flux density in the core,  $B = \phi/A$ , and the fifth is the percentage of the applied mmf that appears across the air gap.

Based on the information in the table, several statements can be made. First, the core reluctance is small with respect to the air gap reluctance. This follows because the permeability of the core material is several orders of magnitude greater than that of the air gap. As a result, the core reluctance has little effect on the solution, and more accurate modeling of the core is not necessary. Second, the reluctance of the air gap decreases as more fringing flux is accounted for. This increases the flux density in the core because the net circuit reluctance decreases with the decreasing air gap reluctance. Last, both methods which account for fringing flux lead to nearly identical solutions.

The fact that the air gap dominates the magnetic circuit has profound implications in practice. It implies that the majority of the applied mmf appears across the air gap as shown in Table 2.1. For analytic work, it allows one to neglect the reluctance of the core in many cases, thereby

TABLE 2.1 Magnetic Circuit Solutions

Air gap permeance model	$R_g(H^{-1})$	$R_c(H^{-1})$	Core flux density (T)	Percentage air gap mmf (%)
Figure 2.8a	3.98e6	4.18e5	0.91	90.5
Figure 2.8b	3.29e6	4.18e5	1.08	88.7
Figure 2.8c, $X = 10g$	3.26e6	4.18e5	1.09	88.6

simplifying the analysis considerably. The dominance of the air gap also implies that the exact magnetic characteristics of the core do not have a great effect on the solution provided that the permeability of the core remains high. This is fortunate because the core is commonly made from materials having highly nonlinear magnetic properties. These properties are discussed next.

## Magnetic Materials

### Permeability

As stated earlier in (2.1), in linear materials  $B$  and  $H$  are related by  $B = \mu H$ , where  $\mu$  is the permeability of the material. For convenience, it is common to express permeability with respect to the permeability of free space,  $\mu = \mu_0 = 4\pi \cdot 10^{-7}$  H/m. In doing so, a nondimensional relative permeability is defined as

$$\mu_r = \frac{\mu}{\mu_0} \quad (2.15)$$

and (2.1) is rewritten as  $B = \mu_r \mu_0 H$ . Using this relationship, materials having  $\mu_r \approx 1$  are commonly called nonmagnetic materials, while those with greater permeability are called magnetic materials. Permeability as defined by (2.1) and (2.15) applies strictly to materials that are linear, homogeneous (have uniform properties), and isotropic (have the same properties in all directions). Despite this fact, however, (2.1) and (2.15) are used extensively because they approximate the actual properties of more complex magnetic materials with sufficient accuracy over a sufficiently wide operating range.

Ferromagnetic materials, especially electrical steels, are the most common magnetic materials used in motor construction. The permeability of these materials is described by (2.1) and (2.15) in an approximate sense only. The permeability of these materials is nonlinear and multivalued, making exact analysis extremely difficult. In addition to the permeability being a nonlinear, saturating function of the field intensity, the multivalued nature of the permeability means that the flux density through the material is not unique for a given field intensity but rather is a function of the past history of the field intensity. Because of this behavior, the magnetic properties of ferromagnetic materials are often described graphically in terms of their  $B$ - $H$  curve, hysteresis loop, and core losses.

### Ferromagnetic materials

Figure 2.14 shows the  $B$ - $H$  curve and several hysteresis loops for a typical ferromagnetic material. Each hysteresis loop is formed by ap-

plying ac excitation of fixed amplitude to the material and plotting  $B$  vs.  $H$ . The  $B$ - $H$  curve is formed by connecting the tips of the hysteresis loops together to form a smooth curve. The  $B$ - $H$  curve, or dc magnetization curve, represents an average material characteristic that reflects the nonlinear property of the permeability but ignores its multivalued property.

Two relative permeabilities are associated with the  $B$ - $H$  curve. The normalized slope of the  $B$ - $H$  curve at any point is called the relative differential permeability and is given by

$$\mu_d = \frac{1}{\mu_0} \frac{dB}{dH}$$

In addition, the relative amplitude permeability is simply the ratio of  $B$  to  $H$  at a point on the curve,

$$\mu_a = \frac{1}{\mu_0} \frac{B}{H}$$

Both of these permeability measures are useful for describing the relative permeability of the material. Over a significant range of operating conditions, they are both much greater than 1. As is apparent from Fig. 2.14, the relative differential permeability is small for low excitations, increases and peaks at medium excitations, and finally decreases for high excitations. At very high excitations,  $\mu_d$  approaches 1, and the material is said to be in hard saturation. For common elec-

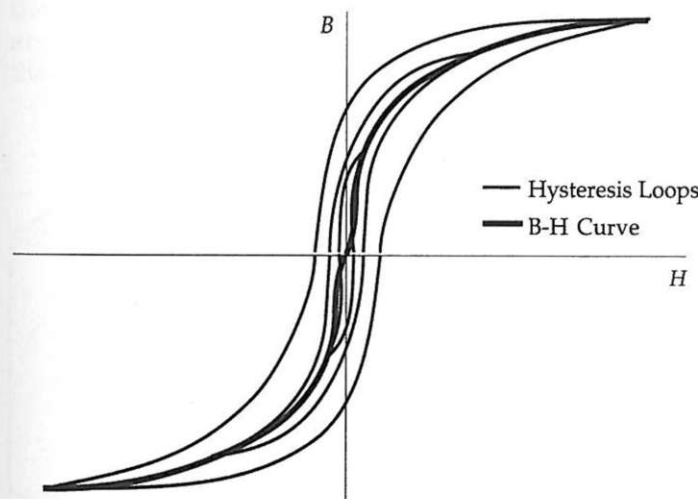


**Figure 2.14** Typical magnetization characteristics of ferromagnetic material.

trical steels, hard saturation is reached at a flux density between 1.7 and 2.3 T, and the onset of saturation occurs in the neighborhood of 1.0 to 1.5 T.

### Core loss

When ferromagnetic materials are excited with any time-varying excitation, energy is dissipated due to hysteresis and eddy current losses. These losses are difficult to isolate experimentally; therefore, their combined losses are usually measured and called core losses. Figure 2.15 shows core loss density data of a typical magnetic material. These curves represent the loss per unit mass when the material is exposed uniformly to a sinusoidal magnetic field of various amplitudes. Total core loss in a block of material is therefore found by multiplying the mass of the material by the appropriate data value read from the graph. In brushless PM motors, different parts of the motor ferromagnetic material are exposed to different flux density amplitudes, different waveshapes, and different frequencies of excitation. Therefore, core loss data such as those shown in Fig. 2.15 are difficult to apply accurately to brushless PM motors. However, because more accurate computation of actual core losses is much more difficult to compute (Slemon and Liu, 1990), traditional core loss data are considered an adequate approximation.

Hysteresis loss results because energy is lost every time a hysteresis loop is traversed. This loss is directly proportional to the size of the hysteresis loop of a given material, and therefore by inspection of Fig.

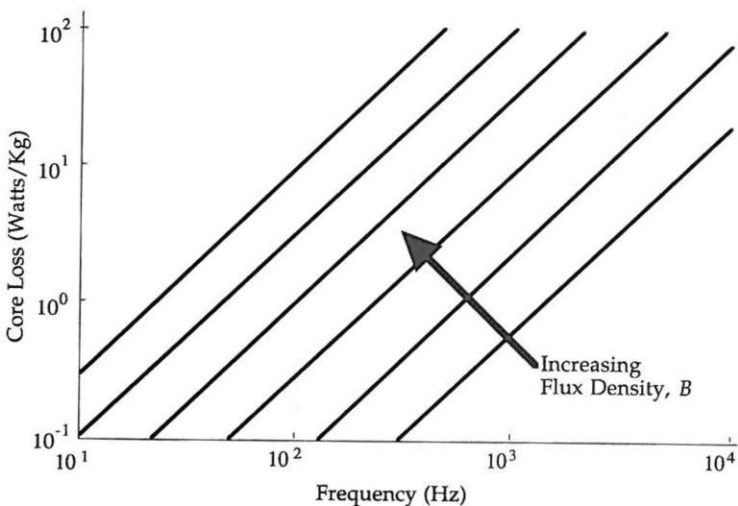


Figure 2.15 Typical core loss characteristics of ferromagnetic material.

2.14, it is proportional to the magnitude of the excitation. In general, hysteresis power loss is described by the equation

$$P_h = k_h f B_m^n$$

where  $k_h$  is a constant that depends on the material type and dimensions,  $f$  is the frequency of applied excitation,  $B_m$  is the maximum flux density within the material, and  $n$  is a material-dependent exponent between 1.5 and 2.5.

Eddy current loss is caused by induced electric currents within the ferromagnetic material under time-varying excitation. These induced eddy currents circulate within the material, dissipating power due to the resistivity of the material. Eddy current power loss is approximately described by the relationship

$$P_e = k_e f^2 B_m^2$$

where  $k_e$  is a constant. In this case, the power lost is proportional to the square of both frequency and maximum flux density. Therefore, one would expect hysteresis loss to dominate at low frequencies and eddy current loss to dominate at higher frequencies.

The most straightforward way to reduce eddy current loss is to increase the resistivity of the material. This is commonly done in a number of ways. First, electrical steels contain a small percentage of silicon, which is a semiconductor. The presence of silicon increases the resistivity of the steel substantially, thereby reducing eddy current losses. In addition, it is common to build an apparatus using laminations of material as shown in Fig. 2.16. These thin sheets of material are coated with a thin layer of nonconductive material. By stacking these laminations together, the resistivity of the material is dramat-

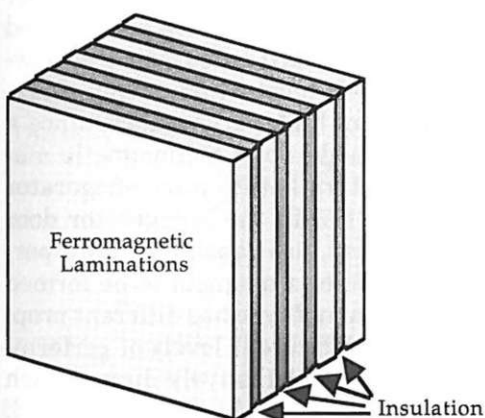


Figure 2.16 Laminated ferromagnetic material.

ically increased in the direction of the stack. Since the nonconductive material is also nonmagnetic, it is necessary to orient the lamination edges parallel to the desired flow of flux. It can be shown that eddy current loss in laminated material is proportional to the square of the lamination thickness. Thus thin laminations are required for lower loss operation.

Laminations decrease the amount of magnetic material available to carry flux within a given cross-sectional area. To compensate for this in analysis, a stacking factor is defined as

$$k_{st} \equiv \frac{\text{cross section occupied by magnetic material}}{\text{total cross section}} \quad (2.16)$$

This factor is important for the accurate calculation of flux densities in laminated magnetic materials. Typical stacking factors range from 0.5 to 0.95.

Though not extensively used in motor construction, it is possible to use powdered magnetic materials to reduce eddy current loss to a minimum. These materials are composed of powdered magnetic material suspended in a nonconductive resin. The small size of the particles used, and their electrical isolation from one another, dramatically increases the effective resistivity of the material. However, in this case the effective permeability of the material is decreased because the nonmagnetic resin appears in all flux paths through the material.

### Permanent magnets

Many different types of PM materials are available today. The types available include alnico, ferrite (ceramic), rare-earth samarium-cobalt, and neodymium-iron-boron (NdFeB). Of these, ferrite types are the most popular because they are cheap. NdFeB magnets are more popular in higher-performance applications because they are much cheaper than samarium cobalt. Most magnet types are available in both bonded and sintered forms. Bonded magnets are formed by suspending powdered magnet material in a nonconductive, nonmagnetic resin. Magnets formed in this way are not capable of high performance, since a substantial fraction of their volume is made up of nonmagnetic material. The magnetic material used to hold trinkets to your refrigerator door is bonded, as is the magnetic material in the refrigerator door seal. Sintered magnets, on the other hand, are capable of high performance because the sintering process allows magnets to be formed without a bonding agent. Overall, each magnet type has different properties leading to different constraints and different levels of performance in brushless PM motors. Rather than exhaustively discuss each of these magnet types, only generic properties of PMs will be discussed.

Those wishing more in-depth information should see references such as McCaig and Clegg (1987).

Stated in the simplest possible terms, PMs are magnetic materials with large hysteresis loops. Thus the starting point for understanding PMs is their hysteresis loop, the first and second quadrant of which are shown in Fig. 2.17. For convenience, the field intensity axis is scaled by  $\mu_0$ , giving both axes dimensions in tesla. (Note: This also visually compresses the field intensity axis. The uncompressed slope of the line in the second quadrant is approximately  $\mu_0$ , which is very small.) The hysteresis loop shown in the figure is formed by applying the largest possible field to an unmagnetized sample of material, then shutting it off. This allows the material to relax, or recoil, along the upper curve shown in the figure. The final position attained is a function of the magnetic circuit external to the magnet. If the two ends of the magnet are shorted together by a piece of infinitely permeable material (an infinite permeance) as shown in Fig. 2.18a, the magnet is said to be keepered, and the final point attained is  $H = 0$ . The flux density leaving the magnet at this point is equal to the remanence, denoted  $B_r$ . The remanence is the maximum flux density that the magnet can produce by itself. On the other hand, if the permeability surrounding the magnet is zero (a zero permeance) as shown in Fig. 2.18b, no flux flows out of the magnet and the final point attained is  $B = 0$ . At this point, the magnitude of the field intensity across the magnet is equal to the coercivity, denoted  $H_c$ . For permeance values between zero and infinity, the operating point lies somewhere in the second quadrant, i.e., between the remanence and coercivity. The absolute value of the slope of the load line formed from the operating point to

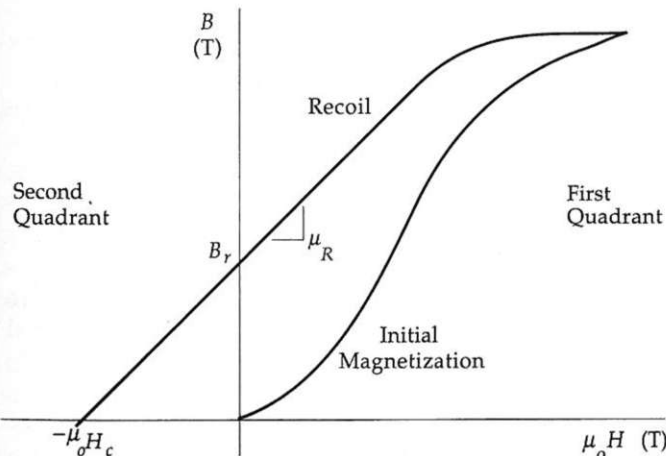
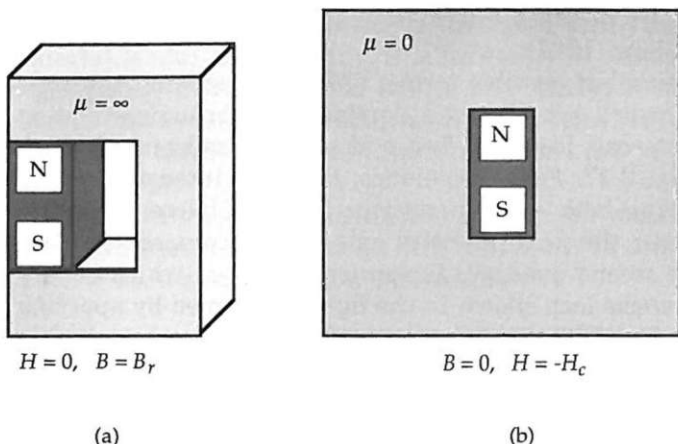


Figure 2.17 The  $B$ - $H$  loop of a permanent magnet.



**Figure 2.18** Operation of a magnet at its (a) remanence and (b) coercivity.

the origin, normalized by  $\mu_0$ , is known as the permeance coefficient (PC) (Miller, 1989). Therefore, operating at the remanence is a PC of infinity, operating at the coercivity is a PC of zero, and operating halfway between these points is a PC of 1.

Hard PM materials such as samarium-cobalt and NdFeB materials have straight demagnetization curves throughout the second quadrant at room temperature, as shown in Fig. 2.19. The slope of this straight line is equal to  $\mu_R\mu_0$ , where  $\mu_R$  is the recoil permeability of the material. The value of  $\mu_R$  is typically between 1.0 and 1.1. At higher temperatures, the demagnetization curve tends to shrink toward the origin, as shown in Fig. 2.19, with these changes often approximated as temperature coefficients on  $B_r$  and  $H_c$ . As this shrinking occurs, the flux available from the magnet drops, reducing the performance of the magnet. This performance degradation is reversible, however, as the demagnetization curve returns to its former shape as temperature drops. In addition to shrinking toward the origin as temperature increases, the knee of the demagnetization characteristic may move into the second quadrant as shown in Fig. 2.19. This deviation from a straight line causes the flux density to drop off more quickly as  $-H_c$  is approached. Operation in the area of the knee can cause the magnet to lose some magnetization irreversibly because the magnet will recoil along a line of lower magnetization, as shown by the dotted line in Fig. 2.19. If this happens, the effective  $B_r$  and  $H_c$  drop, lowering the performance of the magnet. Since this is clearly undesirable, it is necessary to assure that magnets operate away from the coercivity at a sufficiently large PC (denoted  $P_c$  in Fig. 2.19).

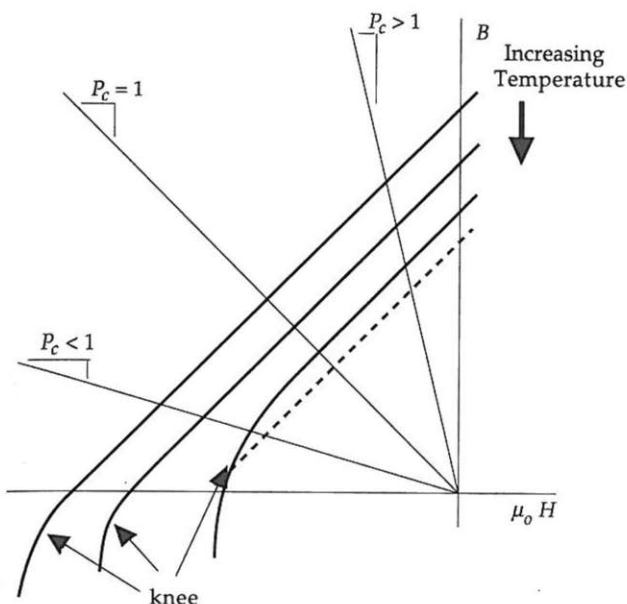


**Figure 2.19** Typical temperature characteristics of permanent magnets.

In addition to the fundamental hysteresis characteristic of PM magnet material, PM material also exhibits a pronounced anisotropic behavior. That is, the material has a preferred direction of magnetization that gives it a permeability that is dramatically smaller in other directions. This fact implies that care must be used when orienting and magnetizing magnets to be sure they follow the desired direction of magnetization with respect to the desired geometrical shape. Moreover, it implies that little flux leaks from the side of a magnet if the magnet is not terribly long.

Before moving on, it is beneficial to define the maximum energy product, as this specification is usually the first specification used to compare magnets. The maximum energy product ( $BH$ )<sub>max</sub> of a magnet is the maximum product of the flux density and field intensity along the magnet demagnetization curve. This product is not the actual stored magnet energy (even though it has units of energy), but rather it is a qualitative measure of a magnet's performance capability in a magnetic circuit. By convention, ( $BH$ )<sub>max</sub> is usually specified in the English units of millions of gauss-oersteds (MG·Oe). However, some magnet manufacturers do conform to SI units of joules per cubic meter (1 MG·Oe = 7.958 kJ/m<sup>3</sup>). For magnets with  $\mu_R \approx 1$ , ( $BH$ )<sub>max</sub> occurs near the unity PC operating point. It can be shown that operation at

$(BH)_{\max}$  is the most efficient in terms of magnet volumetric energy density. Despite this fact, PMs in motors are almost never operated at  $(BH)_{\max}$  because of possible irreversible demagnetization with increasing temperature, as discussed in the previous paragraph (Miller, 1989).

### PM magnetic circuit model

To move the magnet operating point from its static operating point determined by the external permeance, an external magnetic field must be applied. In a motor, the static operating point lies somewhere in the second quadrant, usually at a PC of 4 or more. When motor windings are energized, the operating point dynamically varies following minor hysteresis loops about the static operating point, as shown in Fig. 2.20. These loops are thin and have a slope essentially equal to that of the demagnetization characteristic. As a result, the trajectory closely follows the straight-line demagnetization characteristic described by

$$B_m = B_r + \mu_R \mu_0 H_m \quad (2.17)$$

This equation assumes that the magnet remains in a linear operating region under all operating conditions. Driving the magnet past the remanence into the first quadrant normally causes no harm, as this is

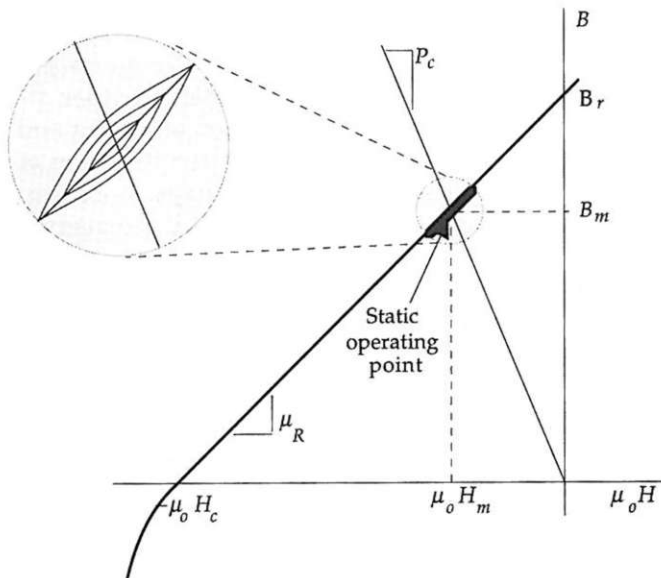


Figure 2.20 Dynamic operation of a magnet about an operating point.

in the direction of magnetization. However, if the external magnetic field opposes that developed by the magnet and drives the operating point into the third quadrant past the coercivity, it is possible to irreversibly demagnetize the magnet if a knee in the characteristic is encountered.

Using (2.17), it is possible to develop a magnetic circuit model for a PM. Let the rectangular magnet shown in Fig. 2.21a be described by (2.17). Then the flux leaving the magnet is

$$\phi_m = B_m A_m = B_r A_m + \mu_R \mu_0 A_m H_m$$

where  $A_m$  is the cross-sectional area of the magnet face in the direction of magnetization. Using (2.4), (2.5), and (2.6), this equation can be rewritten as

$$\phi_m = \phi_r + P_m F_m \quad (2.18)$$

where

$$\phi_r = B_r A_m \quad (2.19)$$

is a fixed flux source, and where

$$P_m = \frac{\mu_R \mu_0 A_m}{l_m} \quad (2.20)$$

is the permeance of the magnet. Conventionally (2.20) is called the magnet leakage permeance, although here it will simply be called the magnet permeance. Equation (2.18) implies that the magnetic circuit model for the magnet is a flux source in parallel with a permeance, as shown in Fig. 2.21b. It is important to recognize that this model as-

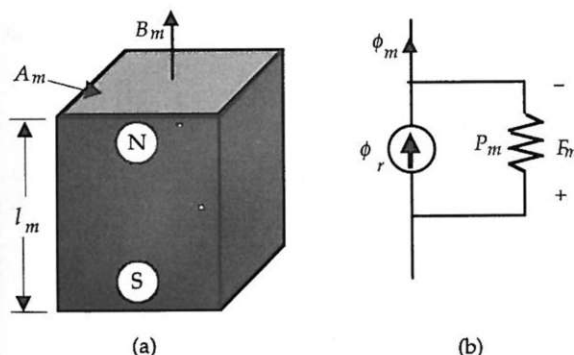


Figure 2.21 A rectangular magnet and its magnetic circuit model.

sumes that the physical magnet is uniformly magnetized over its cross section and is magnetized in its preferred direction of magnetization.

When the magnet shape differs from the rectangular shape shown in Fig. 2.21a, it is necessary to reevaluate its magnetic circuit model. In brushless PM motors having a radial air gap, the magnet shape may appear as an arc, as shown in Fig. 2.22. The magnetic circuit model of this shape can be found by considering it to be a radial stack of differential length magnets, each having a model as given in Fig. 2.21b. During magnetization the same amount of flux magnetizes each differential length. As a result, the achieved remanence decreases linearly with increasing radius because the same flux over an increasing area gives a smaller flux density (Hendershot, 1991). Therefore, integration of these differential elements gives a magnet magnetic circuit model of the same form as Fig. 2.21b with

$$P_m = \frac{\mu_R \mu_0 L \theta_p}{\ln(1 + l_m/r_i)} \quad (2.21)$$

and

$$\phi_r = B_r L \theta_p r_i \quad (2.22)$$

where  $B_r$  is the remanence achieved at  $r_i$  and  $L$  is the axial length of the magnet into the page. In the common case where  $l_m \ll r_i$  (2.21) can be simplified by approximating the permeance shape as rectangular with an average cross section. This approximation gives

$$P_m = \mu_R \mu_0 L \theta_p \left( \frac{1}{2} + \frac{r_i}{l_m} \right) \quad (2.23)$$

### Example

To illustrate the concepts presented in this chapter, consider the magnetic apparatus and circuit shown in Fig. 2.23. The apparatus consists

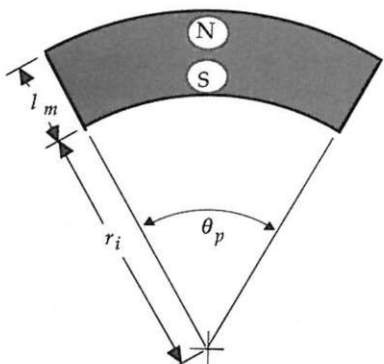


Figure 2.22 An arc-shaped magnet.

of a PM, highly permeable ferromagnetic material, and an air gap. Given that the ferromagnetic material has very high permeability, its reluctance can be ignored, resulting in a magnetic circuit consisting of the magnet equivalent circuit and the air gap permeance as shown in Fig. 2.23b.

Since the flux leaving the magnet is equal to that crossing the air gap, the magnet and air gap flux densities are related by

$$B_g = B_m \frac{A_m}{A_g} = B_m C_\phi \quad (2.24)$$

where  $A_m$  and  $A_g$  are the cross-sectional areas of the magnet and air gap, respectively, and  $C_\phi = A_m/A_g$  is the flux concentration factor. When  $C_\phi$  is greater than 1, the flux density in the air gap is greater than that at the magnet surface.

The magnet flux is easily found by flux division as

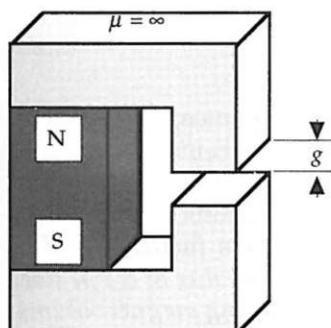
$$\phi_m = B_m A_m = \phi_r \frac{P_g}{P_m + P_g}$$

If the air gap is modeled simply as  $P_g = \mu_0 A_g / g$ , then this equation can be rewritten as

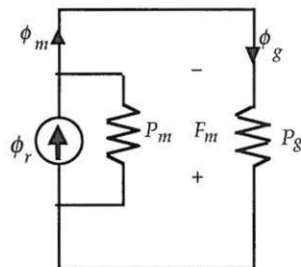
$$\frac{\phi_m}{\phi_r} = \frac{B_m}{B_r} = \frac{1}{1 + (\mu_R g / l_m) C_\phi} \quad (2.25)$$

Knowing  $\phi_m$ , the mmf across the circuit as defined in the figure is

$$F_m = \frac{-\phi_m}{P_g} = \frac{-\phi_r}{P_m + P_g} = \frac{-B_r l_m}{\mu_0 \mu_R [1 + l_m / (\mu_R g) C_\phi^{-1}]}$$



(a)



(b)

Figure 2.23 A simple magnetic structure and its magnetic circuit model.

and the field intensity operating point of the magnet  $H_m = F_m/l_m$  normalized by the magnet coercivity  $H_c = -B_r/(\mu_R\mu_0)$  is

$$\frac{H_m}{H_c} = \frac{1}{1 + l_m/(\mu_R g) C_\phi^{-1}} = 1 - \frac{B_m}{B_r} \quad (2.26)$$

Comparing (2.25) with (2.26), it is clear that there is an inverse relationship between the magnet flux density and its field intensity. As one increases the other decreases. Furthermore, from (2.25), the magnet flux density increases as the flux concentration factor decreases or as the ratio of the magnet length to air gap increases. Therefore, a longer relative magnet length increases the available air gap flux density.

The exact operating point of the magnet is found by computing the permeance coefficient,

$$P_c \equiv \frac{-B_m}{\mu_0 H_m} = \frac{l_m A_g}{g A_m} = \frac{l_m}{g} C_\phi^{-1} \quad (2.27)$$

This remarkably simple result says that the ratio of the magnet length to the air gap length and the flux concentration factor determines the PC. Therefore, for safe operation of the magnet, especially at higher temperatures, the magnet length must be significantly larger than the air gap length. Moreover, any attempt to increase the available air gap flux density through flux concentration, i.e.,  $C_\phi > 1$ , pushes the PC lower.

The fundamental importance of (2.27) can be seen by considering what is required to maintain a constant PC as the concentration factor increases. Multiplying the numerator and denominator of (2.27) by  $A_m A_g$  and simplifying gives

$$P_c = \frac{V_m}{V_g} \frac{1}{C_\phi^2} \quad (2.28)$$

where  $V_m$  and  $V_g$  are the magnet and air gap volumes, respectively. Now if  $C_\phi$  is doubled to  $2C_\phi$  and the air gap volume remains constant, the magnet volume must increase by a factor of  $2^2 = 4$  to maintain a constant PC. If the magnet cross-sectional area remains constant, this implies that the magnet length must increase by a factor of 4. *The implication of this analysis is that concentrating the flux of a PM does not come without the penalty of geometrically increasing magnet volume.*

### Conclusion

In this chapter, the basics of magnetic circuit analysis were presented. Starting with fundamental magnetic field concepts, the concepts of

permeance, reluctance, flux, and mmf were developed. Permeance models for blocks of magnetic material, air gaps, and slotted magnetic structures were developed. The properties of ferromagnetic and permanent-magnet materials were discussed. A magnetic circuit model of a permanent magnet was introduced and the concept of flux concentration was illustrated.

With this background it is now possible to discuss how magnetic fields interact with the electrical and mechanical parts of a motor. These concepts are discussed in the next chapter.

## Electrical and Mechanical Relationships

As stated in the first chapter, the operation of a brushless PM motor relies on the conversion of electrical energy to magnetic energy and from magnetic energy to mechanical energy. In this chapter, the connections between magnetic field concepts, electric circuits, and mechanical motion will be explored to illustrate this energy conversion process.

### Flux Linkage and Inductance

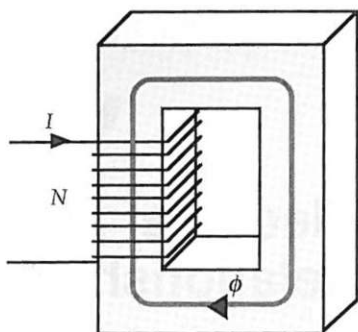
#### Self inductance

To define flux linkage and self-inductance, consider the magnetic circuits shown in Fig. 3.1. This circuit is said to be singly excited since it has only one coil to produce a magnetic field. The flux flowing around the core  $\phi$  is due to the current  $I$ , and the direction of flux flow is clockwise because of the right-hand rule. Using the magnetic circuit equivalent of Ohm's law, the flux produced is given by

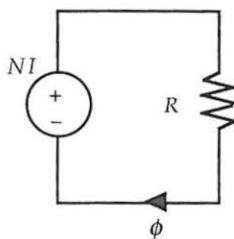
$$\phi = \frac{NI}{R}$$

where  $R$  is the reluctance seen by the mmf source. Since this flux passes through, or links, all  $N$  turns of the winding, the total flux linked by the winding is called the flux linkage, which is defined as

$$\lambda \equiv N\phi \quad (3.1)$$



(a)



(b)

**Figure 3.1** Singly excited magnetic structure and its magnetic circuit model.

Combining these two equations gives

$$\lambda = \frac{N^2}{R} I \quad (3.2)$$

This expression shows that flux linkage is directly proportional to the current flowing in the coil. As a result, it is common to define the constant relating current to flux linkage as inductance

$$L \equiv \frac{\lambda}{I} = \frac{N^2}{R} = N^2 P \quad (3.3)$$

where  $P = R^{-1}$ . This relationship applies in those situations where the reluctance is not a function of the excitation level. That is, it applies when the magnetic material is linear or can be assumed to be linear. When the material is nonlinear, inductance becomes a function of the excitation level. In this case, differential and average inductances are defined in a manner similar to the permeability of ferromagnetic materials.

Equations (3.1) through (3.3) define the inductance properties of a single coil. These relationships are used extensively in brushless PM motor design.

### Mutual inductance

To illustrate mutual inductance, consider the magnetic circuit shown in Fig. 3.2. This circuit is doubly excited because it has two sources of magnetic excitation. Here the flux flowing in the core is composed of two components. By superposition, the flux  $\phi_1$  is the sum of the flux

produced by coil 1 alone, plus that produced by coil 2 alone. Likewise, the same is true for  $\phi_2$ . These facts are stated mathematically as

$$\phi_1 = \phi_{11} + \phi_{12}$$

$$\phi_2 = \phi_{22} + \phi_{21}$$

where  $\phi_{ij}$  is the flux linking the  $i$ th coil due to current in the  $j$ th coil. Solving the magnetic circuit, these fluxes are

$$\phi_{11} = \frac{N_1 I_1}{R_1 + R_2 \| R_m}$$

$$\phi_{22} = \frac{N_2 I_2}{R_2 + R_1 \| R_m}$$

$$\phi_{12} = \phi_{21} = \frac{\phi_{11} R_m}{R_2 + R_m}$$

where  $\parallel$  denotes addition of reluctances in parallel, e.g.,

$$R_a \| R_b \equiv \frac{R_a R_b}{R_a + R_b} \quad (3.4)$$

By the same reasoning that led to (3.1), the flux linkage of each coil is equal to

$$\lambda_1 = N_1 \phi_1 = N_1 (\phi_{11} + \phi_{12})$$

$$\lambda_2 = N_2 \phi_2 = N_2 (\phi_{22} + \phi_{21})$$

Combining the above expressions leads to

$$\begin{aligned} \lambda_1 &= L_1 I_1 + L_{12} I_2 \\ \lambda_2 &= L_{21} I_1 + L_2 I_2 \end{aligned} \quad (3.5)$$

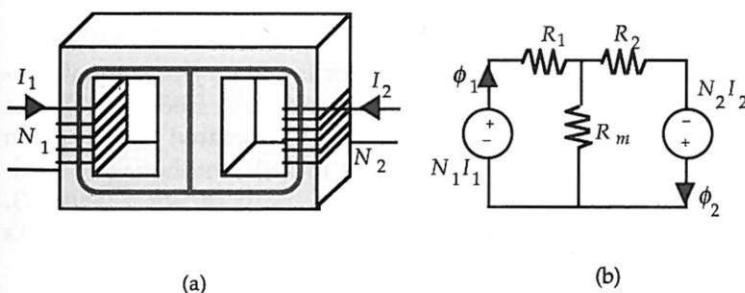


Figure 3.2 Doubly excited magnetic structure and its magnetic circuit model.

where the self inductances  $L_1$  and  $L_2$  are

$$\begin{aligned} L_1 &= \left. \frac{\lambda_1}{I_1} \right|_{I_2=0} = \frac{N_1^2}{R_1 + R_2\parallel R_m} \\ L_2 &= \left. \frac{\lambda_2}{I_2} \right|_{I_1=0} = \frac{N_2^2}{R_2 + R_1\parallel R_m} \end{aligned} \quad (3.6)$$

and the mutual inductances are

$$\begin{aligned} L_{12} &= \left. \frac{\lambda_1}{I_2} \right|_{I_1=0} = \frac{N_1 N_2 R_m}{R_m(R_1 + R_2) + R_1 R_2} \\ L_{21} &= \left. \frac{\lambda_2}{I_1} \right|_{I_2=0} = L_{12} \end{aligned} \quad (3.7)$$

The self inductance expressions in (3.6) are identical to (3.3) in that the denominators in (3.6) are equal to the reluctance seen by the respective coils. The mutual inductance (3.7) is due to the mutual coupling between the two coils. The reluctance  $R_m$  governs the mutual inductance. If  $R_m$  is zero, both coils see a magnetic short and no flux from either coil is linked to the other. Setting  $R_m$  to zero in (3.7) confirms this, as the mutual inductance is zero in this case. On the other hand, if  $R_m$  goes to infinity (a magnetic open circuit), the entire flux from each coil is coupled to the other, since there is no other flux path except that through the other coil. In this case, the mutual inductance is maximum and equal to  $(L_1 L_2)^{1/2}$ .

Mutually coupled coils appear in most brushless PM motors. It is common for a brushless PM motor to have two or more phases, each composed of one or more coils. In this case, the above derivation is easily generalized to include the mutual inductances between pairs of coils.

### Mutual flux due to a permanent magnet

Torque production in a brushless PM motor is due to the mutual coupling between a PM and one or more energized coils. Because a PM is not a coil, it does not have a number of turns associated with it or an inductance. It does, however, provide flux to link another coil. To illustrate this concept, consider the magnetic circuit shown in Fig. 3.3.

In this circuit, the flux leaving the magnet is linked to the coil. As a result, the flux linking the coil can be written as

$$\phi = \phi_1 + \phi_m$$

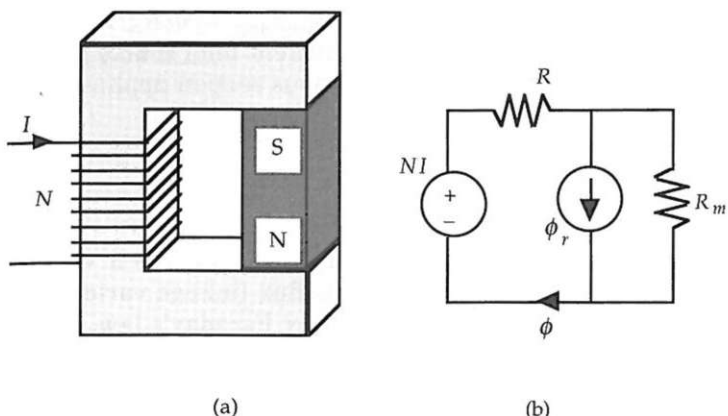


Figure 3.3 A magnetic structure containing a magnet and a coil.

where  $\phi_1$  is the flux linking the coil due to the coil current and  $\phi_m$  is the flux linking the coil due to the magnet. For the given circuit, these fluxes are

$$\phi_1 = \frac{NI}{R + R_m}$$

$$\phi_m = \frac{R_m \phi_r}{R + R_m}$$

As before, this flux links all  $N$  turns of the winding. Thus the flux linkage is

$$\lambda = LI + N\phi_m \quad (3.8)$$

where the self inductance follows from (3.3) as  $L = N^2/(R + R_m)$ .

As an alternative to the above modeling, it is sometimes convenient to perform a Norton to Thévinin source transformation on the PM model as shown in Fig. 3.4. After having done so, the magnet can be

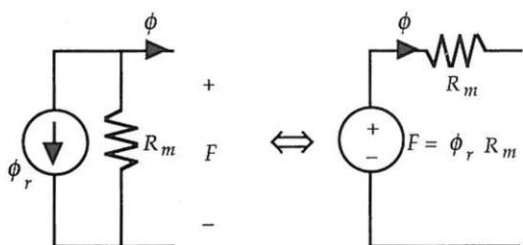


Figure 3.4 The Thévinin equivalent of a magnet.

thought of as a coil producing an mmf of  $N_{\text{mag}}I_{\text{mag}} = \phi_r R_m$  in series with the magnet reluctance. Using this equivalent mmf source model, the mutual inductance modeling of the previous section applies.

## Induced Voltage

### Faraday's law

The primary significance of flux linkage is that it induces a voltage across the winding in question whenever the flux linkage varies with time. The voltage  $e$  that is induced is given by Faraday's law, which states

$$e = \frac{d\lambda}{dt} \quad (3.9)$$

The polarity of the voltage induced is governed by Lenz's law, which states that *the induced voltage will cause a current to flow in a closed circuit in a direction such that its magnetic effect will oppose the change that produces it*. That is, the induced voltage will always try to keep the flux linkage from changing from its present value.

Application of (3.9) to the singly excited case, (3.3), gives

$$e = \frac{d(LI)}{dt} = L \frac{dI}{dt} + I \frac{dL}{dt} \quad (3.10)$$

For constant inductances, the second term on the right-hand side of (3.10) is zero, giving the standard electric circuit analysis relationship for an inductor. When the inductance is not constant, and in particular when it is a function of position  $x$ , then (3.16) can be rewritten as

$$e = L \frac{dI}{dt} + vI \frac{dL}{dx} \quad (3.11)$$

where  $v = dx/dt$  is the velocity or rate at which the inductance changes. The first term in (3.11) is called the transformer voltage, and the second term is the speed voltage or back emf because its amplitude is directly proportional to speed. For rotational systems,  $x = \theta$  and  $v = \omega$ . Based on (3.11), the electric circuit model for an inductor is shown in Fig. 3.5.

An expression similar to (3.11) results when (3.9) is applied to the doubly excited case (3.5) and to the PM case (3.8). Each term in these flux linkage equations has transformer and speed voltage terms. Because these expressions result from the straightforward application of (3.9), they will not be developed further here.

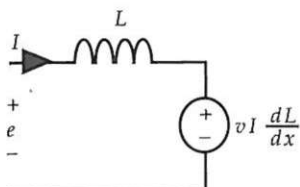


**Figure 3.5** A general circuit model for an inductor.

### Example

To illustrate the calculation of speed voltage, consider the apparatus shown in Fig. 3.6. In this figure, the resistance of the conducting and sliding bars is lumped into the resistance  $R$  at the left. The conducting bars provide a path so that current flows through the sliding bar at any position. Passing through the loop formed by the resistance, conducting bars, and sliding bar is an applied magnetic field having a constant and uniform flux density  $B$  flowing into the page. Given this setup, it is desired to find the speed voltage induced across the resistance due to sliding bar motion.

The flux flowing through the loop is given by  $\phi = BLx$ , where the product  $Lx$  is the area of the loop through which  $B$  passes. Since the loop forms a one-turn coil, the flux linkage is equal to the flux itself, and the voltage induced is found by applying (3.9),

$$e_b = \frac{d(BLx)}{dt} = BL \frac{dx}{dt} = BLv \quad (3.12)$$

where  $v = dx/dt$  is the sliding bar velocity. This expression is known as the  $BLv$  law. The polarity of this speed voltage is determined by applying Lenz's law and the right-hand rule of magnetic fields about a wire.

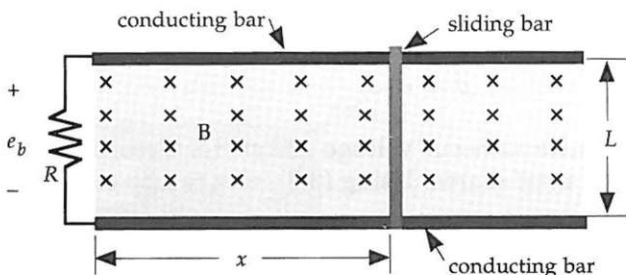


**Figure 3.6** A conceptual linear motor/generator.

Assume that the bar is pulled to the right, so that  $x$  is increasing. Then if the induced voltage given by (3.12) appears across the resistor with a positive potential at the top, a current is induced in the loop in the counterclockwise direction. By the right-hand rule, this current creates a magnetic field that is directed out of the page inside the loop. This opposes the applied magnetic field and therefore agrees with Lenz's law. Thus the voltage is positive at the top of the resistor for increasing  $x$  and an applied magnetic field directed into the page. The polarity of the induced voltage changes if either of these conditions changes. If both change, i.e.,  $x$  decreases and the magnetic field is directed out of the page, the polarity remains the same. It is important to note that the magnetic field produced by current in the loop does not modify  $B$  in (3.12). Equation (3.12) is independent of the magnetic field produced by current flow.

Although the  $BLv$  law is derived for the apparatus shown in Fig. 3.6, it is useful in many applications where a constant flux density passes through a coil. In particular, it is useful for brushless PM motor design.

## Energy and Coenergy

The energy stored in a magnetic field is an important quantity to know in the design and analysis of brushless PM motors, as the magnetic field is the medium through which electric energy is converted to mechanical energy. In addition, knowing the energy or coenergy stored in a magnetic field provides one method for computing inductance.

### Energy and coenergy in singly excited systems

To illustrate the computation of energy and coenergy, reconsider the singly excited magnetic circuit shown in Fig. 3.1a. Ignoring resistive losses, the instantaneous power delivered to the magnetic field of the coil is

$$p = ei$$

where  $e$  and  $i$  are the instantaneous voltage and current, respectively, in the coil forming the mmf source. Using (3.9), this can be rewritten as

$$p = i \frac{d\lambda}{dt}$$

Since power is the rate at which energy is transmitted, the energy stored in the coil at a time  $t$  is given by the integral of power,

$$W = \int_0^t i \frac{d\lambda}{dt} dt = \int_{\lambda(0)}^{\lambda(t)} id\lambda \quad (3.13)$$

where  $\lambda(0)$  is the initial flux linkage and  $\lambda(t)$  is the flux linkage at time  $t$ . For a linear magnetic circuit,  $i$  and  $\lambda$  are related by the inductance given in (3.3). Substituting (3.3) into the above expression gives

$$W = \frac{1}{2L} [\lambda(t)^2 - \lambda(0)^2]$$

From this expression it is apparent that if the flux linkage at time  $t$  is less than the flux linkage at time 0, the energy supplied is negative. This implies that energy has come out of the magnetic field. It is customary to let the initial energy stored be zero, implying that  $\lambda(0) = 0$ . By doing so, the above equation describes the total energy stored in the magnetic field. Using this assumption, the above becomes

$$W = \frac{\lambda^2}{2L} \quad (3.14)$$

where  $\lambda = \lambda(t)$ .

As described by (3.13), energy stored in a magnetic field can be viewed as the shaded area to the left of the inductance line shown in Fig. 3.7. When  $\lambda(0) = 0$  is assumed, energy is simply the area of the triangle to the left of the line.

Oftentimes it is convenient to express energy in terms of current rather than flux linkage as given in (3.14). For linear magnetic circuits as being considered here, the area below the inductance line shown in

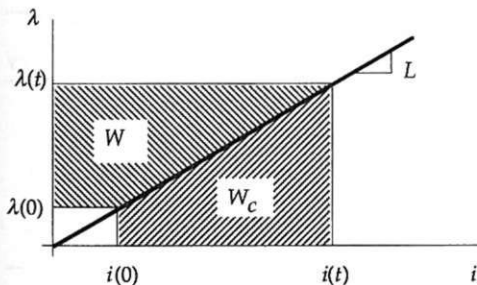


Figure 3.7 Graphical interpretation of energy and coenergy.

Fig. 3.7 is numerically equal to the area on the left. The area below the line is called coenergy and is given by

$$W_c = \int_{i(0)}^{i(t)} \lambda \, di$$

which upon substitution of (3.3) and  $i(0) = 0$  becomes the familiar expression

$$W_c = \frac{1}{2} L i^2 \quad (3.15)$$

Equations (3.14) and (3.15) define the energy and coenergy stored in a singly excited magnetic circuit. Before considering doubly excited circuits, it is sometimes useful to express energy and coenergy in terms of magnetic circuit and magnetic field parameters. These relationships are shown in Table 3.1. In terms of magnetic circuit parameters,  $\phi$ ,  $P$ , and  $F$  are the flux, permeance, and mmf associated with a particular block of magnetic material. In terms of magnetic field parameters, the energy and coenergy expressions in Table 3.1, apply to a differential size block of magnetic material, and therefore these expressions are more correctly called energy and coenergy densities.

### Energy and coenergy in doubly excited systems

For doubly excited systems such as that shown in Fig. 3.2a, expressions for energy and coenergy are more involved because energy is stored in both the self and mutual inductances. In particular, the calculation of energy stored in mutual inductance requires more rigor than the preceding analysis. As a result, only the final result is given here, and the interested reader is encouraged to consult other references such as McPherson and Laramore (1990) for more information.

TABLE 3.1 Energy and Coenergy Relationships

Parameter type	Energy	Coenergy
Electric circuit	$\frac{\lambda^2}{2L}$	$\frac{1}{2} Li^2$
Magnetic circuit	$\frac{\phi^2}{2P}$	$\frac{1}{2} PF^2$
Magnetic field	$\frac{B^2}{2\mu}$	$\frac{1}{2} \mu H^2$

The instantaneous power delivered to the magnetic field in Fig. 3.2 is

$$p = i_1 \frac{d\lambda_1}{dt} + i_2 \frac{d\lambda_2}{dt}$$

where the subscripts refer to the respective coils. Following a procedure similar to the singly excited case above, the energy stored in the magnetic field is

$$W = \frac{\lambda_{11}^2}{2L_1} + \frac{\lambda_{22}^2}{2L_2} + \frac{\lambda_{12}^2}{L_{12}} \quad (3.16)$$

where  $\lambda_{11} = N_1\phi_{11}$ ,  $\lambda_{22} = N_2\phi_{22}$ , and  $\lambda_{12} = N_1\phi_{12}$ . The coenergy stored follows as

$$W_c = \frac{1}{2}L_1i_1^2 + \frac{1}{2}L_2i_2^2 + i_1i_2L_{12} \quad (3.17)$$

Comparing (3.16) and (3.17), the advantage of using coenergy is apparent as the terms in (3.17) are much more obvious. In these equations, the first two terms are the energy and coenergy stored in the self inductances, respectively, and the last term is energy and coenergy stored in the mutual inductance.

### **Coenergy in the presence of a permanent magnet**

Because of its importance in brushless PM motors, it is important to consider the coenergy stored in the magnetic field of magnetic circuit containing a PM. For the magnetic circuit shown in Fig. 3.3, the coenergy stored is

$$W_c = \frac{1}{2}Li^2 + \frac{1}{2}(R + R_m)\phi_m^2 + Ni\phi_m \quad (3.18)$$

where  $\phi_m$  is the magnet flux linking the coil. In this expression, the first term is the coenergy stored in the self inductance, the second term is the coenergy stored due to the magnet alone, and the last is the coenergy due to mutual flux.

As will be discussed next, the torque produced by a motor is composed of two components, one due to the self inductance terms in (3.18) and the other due to the mutual terms. In a brushless PM motor, the torque due to mutual terms is desired and that due to self inductance terms is commonly parasitic.

## Force, Torque, and Power

The torque produced by a brushless PM motor is the most important quantity to be determined. Torque is a measure of the turning force that can be produced in a motor and represents the fundamental specification to be met in all applications.

### Basic relationships

Energy in a mechanical system is called work. Work is equal to the product of force and distance. More accurately it is the product of the displacement of an object and the component of the force along the direction of displacement. Thus a differential amount of mechanical energy can be written as

$$dW_m = F \, dx$$

where  $W_m$  is mechanical energy,  $F$  is the force in the  $x$  direction, and  $dx$  is a differential length in the  $x$  direction.

Power is the amount of work done per unit time, or the rate of change of energy with respect to time. Thus, from the above, mechanical power is given by

$$P_m = \frac{dW_m}{dt} = F \frac{dx}{dt} = Fv \quad (3.19)$$

where  $v$  is the velocity of motion.

When motion is confined to rotation, one deals with torque rather than force. The relationship between torque and force was discussed in Chap. 1 and is described in Fig. 1.4 and by (1.1). A tangential force  $F$ , acting at a radius  $r$ , produces a torque  $T$ , given by the product of the force and the length of the lever arm  $r$ , over which the force is acting, i.e.,  $T = Fr$ . In this case, a differential amount of work is given by

$$dW_m = F \, dx = Fr \, d\theta = T \, d\theta$$

where the relationship between circumferential distance and angular position,  $x = r\theta$ , has been used. Finally, as defined earlier, the mechanical power is

$$P_m = \frac{dW_m}{dt} = T \frac{d\theta}{dt} = T\omega \quad (3.20)$$

where  $\omega$  is the rotational speed in radians per second.

### Fundamental implications

Equations (1.5) and (3.20) play an important role in the design of motors. Since torque is proportional to diameter squared as stated in (1.5) and since by (3.20) power is directly proportional to torque, a motor having a larger diameter at which torque is generated will produce more mechanical power. Therefore, it appears that motor diameter should be maximized. However, there are a number of constraints that limit the diameter of a motor. The most obvious constraint is the physical space limitations dictated by a particular application. Other constraints are volume, mass, and inertia. The volume of a motor increases with the square of radius or diameter. Thus the ratio of output power to volume cannot be increased by increasing motor diameter. Since motor mass is proportional to its volume, the ratio of output power to mass cannot be increased either, unless the average mass density of the motor volume decreases as diameter increases. As diameter increases, it is usually possible to have an increasing proportion of the motor volume be composed of air. Therefore, some increase in power density is possible as diameter increases. The last constraint, inertia, is significant in applications requiring maximum torque to inertia ratio. The inertia of a rotor is proportional to the fourth power of its radius or diameter. Therefore, the torque to inertia ratio of a motor decreases as the square of rotor radius. Clearly, in cases where the inertia is to be minimized, a large diameter must be avoided.

Besides the significance of diameter, (1.5) and (3.20) indicate several other important points. Once a diameter is chosen, there are two ways to increase the power developed. The first is to increase the speed at which the motor operates. In most applications, the load speed is specified; therefore, the only way to increase power by increasing speed is to use some form of speed reduction between the motor and its load. While this is simple conceptually, speed reduction components add significant volume, mass, inertia, cost, and reduced reliability that must be weighed against the benefits of higher-speed operation. The other way to increase power for a fixed diameter is to increase the force density acting on the rotor. This is accomplished by increasing the electrical and magnetic operating points of the motor. Often these are referred to as the electric and magnetic loadings, respectively (Miller, 1989). Again, this does not come without constraints. Increasing the electrical operating point implies increasing the current supplied to the motor. This adds resistive heat loss to the system that increases as the square of current and that must be removed from the system. In a brushless PM motor, increasing the magnetic field operating point, requires more or higher-performance magnet material, or specialized motor construction to focus or concentrate flux into the air gap. As was discussed earlier, flux concentration geometrically increases the

amount of magnet material required. Moreover, ferromagnetic material is required to concentrate flux. The addition of this material increases the mass and volume of a motor.

It should be clear from the above discussion that getting the highest performance out of a motor for the least cost is not simple. When high performance is required, many physical constraints are pushed to their limits. As a result, high-performance motor design requires that all physical constraints be identified and included in the design process. Engineering practice suggests that any constraint not included in the design process will likely be pushed well beyond what is feasible.

### Torque from a macroscopic viewpoint

There are two general ways to determine the torque produced by a magnetic field. The first of these is based on taking a macroscopic viewpoint, a viewpoint that uses the concept of conservation of energy. This method requires that all electrical, magnetic, and mechanical losses in the motor be modeled as being external to the motor. What remains is a conservative system where no energy is lost. Any added electrical energy must contribute to the energy stored in the magnetic field and to the output mechanical energy. Stated in terms of a differential amount of added energy, conservation of energy requires that

$$dW_e = dW + dW_m$$

where  $dW_e$ ,  $dW$ , and  $dW_m$  are differential amounts of electrical, magnetic field, and mechanical energies, respectively.

Based on the above expression, it is possible to show that the torque can be related to the rate of change of field energy as

$$T = \left. \frac{-\partial W}{\partial \theta} \right|_{A=\text{constant}} \quad (3.21)$$

and can be related to the rate of change of field coenergy as

$$T = \left. \frac{\partial W_c}{\partial \theta} \right|_{i=\text{constant}} \quad (3.22)$$

The derivation of (3.21) and (3.22) can be found in many references, and the interested reader is encouraged to refer to them. As stated above, positive torque acts to decrease the stored energy at constant flux, and acts to increase coenergy stored at constant current.

Equations (3.21) and (3.22) apply to the general case. When restricted to the linear case, which is required to design motors analytically, these equations can be simplified. In addition, because coenergy is described in terms of current rather than flux linkage, (3.22) is the

most convenient expression to use. Since both equations give the same result when appropriate substitutions are made, only results using (3.22) will be given here.

Application of (3.22) to the mutual inductance case (3.17) gives

$$T = \frac{1}{2} i_1^2 \frac{dL_1}{d\theta} + \frac{1}{2} i_2^2 \frac{dL_2}{d\theta} + i_1 i_2 \frac{dL_{12}}{d\theta} \quad (3.23)$$

The significance of this equation is best discussed by considering each term individually. To do so, first assume that the system under investigation is singly excited, i.e.,  $i_2 = 0$ . In this case only the first term in (3.23) remains. The first term implies that the torque produced is a function of the square of the applied current, and therefore is not a function of the direction of current flow. This makes sense, since an electromagnet will attract a piece of steel irrespective of the direction of current flow. In addition, the first term implies that positive torque, or attraction, occurs whenever inductance is increasing. In other words, this torque term always acts to increase inductance or permeance (since  $L = N^2P$ ) and acts to decrease reluctance. As a result, this term is called reluctance torque. Thinking of the electromagnet example, this fact makes sense also, because the coil inductance and permeance of the magnetic circuit increase as the piece of steel is attracted closer to the electromagnet.

Next, if one assumes that  $i_1 = 0$ , rather than  $i_2$  as considered above, only the second term in (3.23) remains. Because of the similarity between the first and second terms, this torque term is also reluctance torque and has the same properties as the first term.

Finally, if the self inductances  $L_1$  and  $L_2$  are both constant as a function of position, only the last term in (3.23) remains. This term is due to the mutual flux or inductance between the two coils and is commonly called the mutual torque or alignment torque. This term exists only if there is some variation in the mutual inductance between the two coils as a function of position. In this case, positive torque acts to increase the mutual coupling between the two coils when the currents have the same sign, and acts to decrease it when the currents have the opposite signs. With reference to Fig. 3.2, positive torque is produced when the mutual fluxes add, and negative torque is produced when the mutual fluxes oppose each other. Alternatively, this property states the well-known axiom that *opposite magnetic poles attract and like poles repel*.

Application of (3.22) to the case of a mutually coupled coil and PM, (3.18) gives

$$T = \frac{1}{2} i^2 \frac{dL}{d\theta} - \frac{1}{2} \phi_m^2 \frac{dR}{d\theta} + Ni \frac{d\phi_m}{d\theta} \quad (3.24)$$

In this expression, the first two terms are the reluctance torque associated with the coil and magnet, respectively, and the third term is the alignment torque due to the mutual flux linking the magnet to the coil. The first term is identical to that in (3.23). The second term is a torque component proportional to the square of the flux leaving the magnet and is not a function of the polarity of the flux. The reason for the minus sign in front of this term is that inductance is inversely proportional to reluctance. Thus  $dL/d\theta$  is proportional to  $-dR/d\theta$ , making the first and second terms in (3.24) equivalent in terms of torque production. Since the mutual flux linkage between the flux leaving the magnet  $\phi_m$  and the coil is  $\lambda_m = N\phi_m$ , the last term in (3.24) is equivalent to the last term in (3.23) where  $\lambda_{12} = L_{12}i_2$ .

### Force from a microscopic viewpoint

As an alternative to the approach discussed above, it is possible to develop an expression for mutual force based on the known interaction between a moving point charge and a magnetic field. This relationship is described by the Lorentz force equation,

$$\mathbf{F} = q\mathbf{v} \times \mathbf{B}$$

where  $q$  is the charge value,  $v$  is the charge velocity,  $B$  is the flux density acting on the charge, and  $\times$  denotes the vector cross product of the velocity and flux density. Using the definition of the cross product, the magnitude of the resulting force is

$$F = qvB \sin \alpha \quad (3.25)$$

where  $\alpha$  is the angle between the  $v$  and  $B$  vectors. The direction of the force produced is shown in Fig. 3.8 and is given by the right-hand rule: *If the right hand is held so that the fingers curl from  $v$  to  $B$ , the extended thumb points in the direction of  $F$ .* Since maximum force is generated when  $v$  and  $B$  are perpendicular to each other, it is common practice to enforce this relationship in applications. As a result,  $\alpha = \pi/2$  is assumed in the following analysis.

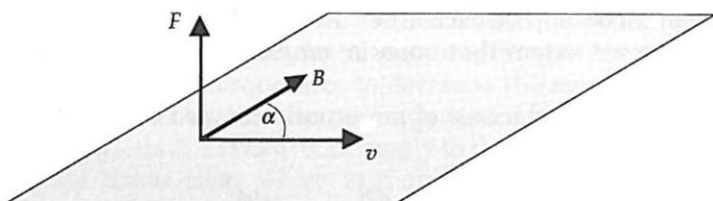


Figure 3.8 Graphical interpretation of the Lorentz force equation.

Equation (3.25) is applicable to motor design with further manipulation. Considering a differential charge element  $dq$ , and expressing velocity as  $dl/dt$ , where  $l$  is length along the path of motion, (3.25) expresses the differential force produced by the differential charge as

$$dF = dq \frac{dl}{dt} B$$

Next, recognizing current as the rate of change of charge with respect to time  $i = dq/dt$ , this expression can be written as

$$dF = iB dl$$

Based on this expression, the total force experienced by a wire conducting a current  $i$  in the presence of a magnetic field  $B$  is given by the integral

$$F = \int iB dl$$

If the wire is straight and exposed to a uniform magnetic field over a length  $L$ , this integral has the solution

$$F = BLi \quad (3.26)$$

This expression, known as the  $BLi$  law, is useful for computing the force or torque caused by the interaction of a magnetic field and a current-carrying wire. It is important to note that (3.26) is independent of the magnetic field produced by the current  $i$  and, as such, (3.26) expresses a mutual force component. The magnetic field produced by the current  $i$  is historically known as armature reaction (McPherson and Laramore, 1990; Nasar, 1987). The net magnetic field about the wire is the superposition of the external magnetic field  $B$  and that due to armature reaction. The presence of nonlinear magnetic material in the region where these two fields interact can cause superposition to be violated. In this case, the force generated, as given by (3.26), is dependent on the armature reaction field. Since steel often appears in the region where field interaction occurs, a potential reduction in generated force due to armature reaction must be considered in machine design.

### Reluctance and mutual torque

Based on the preceding discussion, it is apparent that torque is generated by two distinct mechanisms. If self inductance changes as a function of position, reluctance torque is generated. If mutual induct-

ance changes as a function of position, mutual or alignment torque is generated. Most motors are designed to develop torque using only one of these two torque production mechanisms. For example, induction motors, dc brush and brushless motors, and synchronous motors develop mutual torque, whereas switched reluctance motors are designed to utilize reluctance torque. In motors designed to produce mutual torque, reluctance torque is commonly parasitic. That is, any torque produced due to a variation in self inductance is undesired. The most common parasitic torque developed is called cogging torque, which is due to slotting on the stator or rotor of the motor. Cogging torque is the primary ripple component in the torque generated by a motor. In addition to cogging, there are a number of other sources of reluctance torque in a mutual torque motor. These sources are due to inevitable mechanical imperfections such as eccentricities and dimensional variations. Since constant torque is usually desired from a motor to produce smooth mechanical motion, parasitic torque components must be minimized.

### Example

To illustrate the calculation of force, consider the setup shown in Fig. 3.9. This setup is similar to that shown in Fig. 3.6, which was used to illustrate the computation of back emf. In Fig. 3.9, the voltage source creates a current in the sliding bar that interacts with the magnetic field directed into the paper. As was discussed earlier, the motion of the sliding bar induces a back emf  $e_b$  across the conducting bars as shown in the figure.

The force on the bar in Fig. 3.9 can be found using both the macroscopic and microscopic methods discussed above. Use of the microscopic method is straightforward. The  $BLi$  law (3.26) describes the force on the sliding bar. Using the right-hand rule, the direction of motion is to the right. Alternatively, the direction can be computed by noting that the force is directed toward the area where the external field  $B$

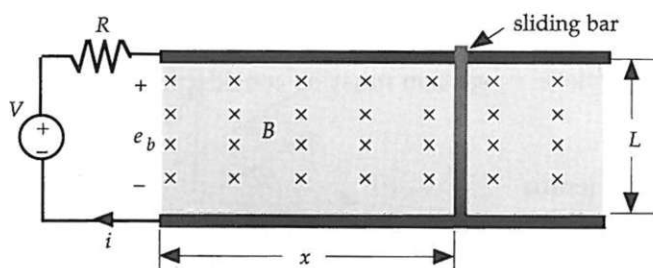


Figure 3.9 A conceptual linear motor/generator.

and the field generated due to current flow are in opposition or where the net field is weaker. From the figure, the fields are in opposition to the right of the bar; thus the force is directed to the right.

Using the macroscopic coenergy method, (3.24) applies to Fig. 3.9. The last term in (3.24) describes the mutual torque developed between a flux and a current-carrying coil. For linear motion this last term can be written as

$$F = Ni \frac{d\phi_m}{dx} \quad (3.27)$$

where  $\phi_m$  is the flux linking the coil. For the setup given in Fig. 3.9,  $N = 1$ , and  $\phi_m = BLx$ . By substituting these facts into (3.27), the force on the bar is again described by the  $BLi$  law.

The above application illustrates an important point that is apparent when the electrical and mechanical power in the system are computed. The electrical power delivered to the sliding bar is

$$P_e = e_b i = BLvi$$

where (3.12) has been used to describe the back emf  $e_b$ . The mechanical output power is found by applying (3.19),

$$P_m = Fv = BLiv$$

Since these last two expressions are both equal to  $BLvi$ , the output mechanical power is equal to the input electrical power. This implies that the power stored in the magnetic field is zero, which implies that the energy stored in the magnetic field is constant with respect to time.

This relationship between electrical and mechanical power holds in all cases of mutual torque or force production and is sometimes useful for finding the back emf or torque/force. Given either of these, the other can be found from

$$P_m = e_b i = T\omega = Fv \quad (3.28)$$

In addition to its utility in motor analysis, (3.28) has profound implications in motor design. According to (3.28), for a given mechanical output power, the required electrical input power can be composed of a high back emf at a low current, a high current at a low back emf, or some compromise in between. Of these choices, a high back emf at a low current is usually preferred because minimizing current tends to minimize motor drive losses. Winding  $I^2R$  losses, however, are not a function of the back emf level if the cross-sectional area occupied by the motor windings remains constant. As the number of turns increases to increase the back emf, winding wire size must decrease accordingly so that the increased number of turns fits into the space allotted.

## Brushless Motor Operation

The design of brushless motors is not a simple task. On the more general level, motor design requires knowledge of magnetics, mechanics, thermodynamics, electronics, acoustics, and material science. On a more specific level, it requires knowledge of the performance requirements and constraints imposed by the specific application area. Given this body of knowledge, motor design involves finding the optimal solution for the least effort and cost. This text focuses primarily on the magnetic aspects of motor design. Other general aspects listed above are considered in the design process, but detailed design information is not provided.

### **Assumptions**

Besides the performance requirements discussed above, other initial assumptions are necessary to more clearly define and focus the design of brushless PM motors. Some of these assumptions add restrictions and others identify conventional design techniques. Later, some of these assumptions will be relaxed.

### **Rotational motion**

It is assumed that motion is to be generated directly in the tangential or circumferential direction. No mechanical apparatus is used to convert linear motion to rotational motion.

### **Motor load**

The motor load is assumed to be such that operation above some base motor speed is not required. Therefore, design aspects that specifically

support constant power operation through field weakening are not considered here.

### **Motor drive**

It is assumed that an inverter is used to convert a dc bus voltage to the current waveforms needed for motor operation. It is also assumed that these waveforms need not be sinusoidal. As a result, the air gap flux distribution need not be a sinusoidal function of position as is commonly done in conventional motors driven directly from the ac power line.

It is well known that a sinusoidally distributed air gap flux produces a sinusoidal back emf, which in turn produces constant torque if sinusoidal currents are applied to the motor (Miller, 1989). While constant torque is usually desirable, sinusoidal currents and a sinusoidal flux distribution are just one way to produce constant torque. It is certainly the most convenient way for a motor driven directly from the ac power line. Though it will not be discussed here, when a motor is driven from an inverter, it is possible to supply the motor with a current waveform that produces constant torque for any reasonable back emf waveshape.

### **Slotting**

It is assumed that the stator will have slots containing the motor windings. The salient-pole, concentrated-winding construction shown in Fig. 1.10 will not be discussed. In motors without slots or poles, the windings are formed, potted, and attached to the stator back iron. Since the windings and potting material are nonmagnetic, the effective air gap of slotless machines is quite large. Because of this, a slotless machine requires longer, more massive magnets to establish a sufficient PC. The only disadvantage of having slots is that they add cogging torque that must be minimized to reduce noise and vibration.

### **Surface-mounted magnets**

It is initially assumed that the motor design will incorporate PMs that are exposed to the air gap. The reason for this assumption is that burying NdFeB and samarium-cobalt magnets in electrical steel offers few advantages. Magnets are buried for one of two reasons, either to concentrate flux across the air gap or to provide a means for implementing field weakening. As discussed earlier, the latter of these two reasons is not considered here.

Because NdFeB and samarium-cobalt magnets exhibit high remanence, little flux concentration is possible. As was discussed earlier

and illustrated in Fig. 2.12, the presence of slots focuses the air gap flux into the teeth between the bottoms of the slots. Given a ferromagnetic material saturation level near 1.8 T and a typical slot fraction of 50 percent, the maximum air gap flux density is roughly 0.9 T, which is near the remanence of NdFeB and samarium-cobalt magnets.

### Steel

It is assumed that the ferromagnetic material used in the motor is not operated in heavy saturation. In addition, it is assumed that the material can be adequately modeled as a highly permeable linear magnetic material. While this assumption is violated to some degree in every design, its use greatly simplifies motor design derivations. In addition, it is assumed that the steel used is laminated.

### Basic Motor Operation

A survey of brushless PM motors would show that they are constructed in many different ways, as described in Chap. 1. Most motors have radial air gaps, while some have an axial air gap. Some motors have two air gaps, while most have just one. In motors with two air gaps, the stator is sometimes female and the rotor male, while in others the opposite is true. In addition to these structural issues, some motors have a large number of magnets while others have as few as two. Most motors are constructed with three-phase windings because three phases minimizes the number of power electronic devices required to drive the motor.

Despite all the differences in brushless PM motor designs, their operation is uniformly based on the same principle. All brushless PM motors develop torque based on the Lorentz force equation (3.25), which can be rewritten in terms of torque as

$$dT = RI \, dl \times B \quad (4.1)$$

where  $dT$  is the differential torque developed at a radius  $R$  by a current  $I$  flowing in a differential length of wire  $dl$ , exposed to a magnetic field  $B$ , which emanates from a PM. Because torque is developed in the circumferential direction  $\theta$  the vector cross product in (4.1) dictates that the current and magnetic field travel in the axial direction  $z$  and radial direction  $r$  to produce torque in the most efficient manner. Thus cylindrical coordinates  $(r, \theta, z)$  are natural for motor design. If the magnetic field travels in the radial direction across an air gap, current must travel in the axial direction. Alternately, if the magnetic field travels in the axial direction across an air gap, current must flow in the radial direction. The only exception to this orientation rule between

$Idl$  and  $B$  occurs if ferromagnetic material is used to redirect the interaction between the magnetic field  $B$  and the magnetic field induced by current flow in the wire.

Because brushless PM motors operate based on (4.1) but their topologies vary, it is beneficial to discuss basic motor operation in terms of a coordinate system that can be applied to any specific topology. For this reason, linear translational motion is discussed here. Using this simple topology, many design parameters and issues such as flux linkage, back emf, force, winding approaches, self inductance, mutual inductance, winding resistance, conductor forces, cogging force, armature reaction, rotor-stator attraction, and core loss can be determined.

### Magnetic Circuit Model

To develop force and back emf expressions, consider the prototype linear translational motor cross section shown in Fig. 4.1. The structure shown is assumed to repeat indefinitely in both directions. In a rotational system producing torque, the two ends would meet halfway around the motor, giving a finite number of magnet poles. In Fig. 4.1, the rotor is composed of magnets alternating in polarity, separated by nonmagnetic spacers (which could be air) and attached to ferromagnetic *back iron*. The stator is composed of ferromagnetic back iron with slots containing the windings of one phase. The slots are oriented such that there is one slot per magnet, or one slot per pole per phase. For simplicity, slots for additional phases are not shown at this time.

The purpose of the rotor and stator back iron is to provide a magnet flux return path as illustrated about the center magnet in the figure. Flux paths for all other magnets follow accordingly. Because the flux from one magnet splits equally and couples to the two magnets adjacent to it, it is possible to model the entire motor in terms of one closed flux loop that repeats indefinitely. Given Fig. 4.1, the laminations forming the rotor and stator back iron are composed of sheets of material having

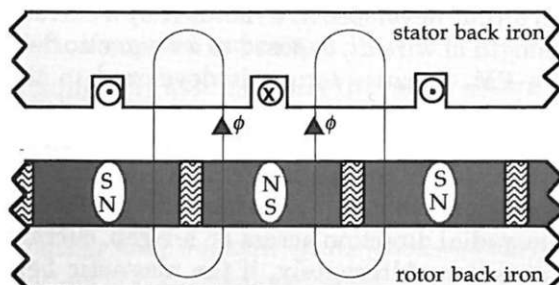


Figure 4.1 Basic translational permanent-magnet motor structure.

outlines as shown in Fig. 4.1 and oriented in a stack coming out of the page.

The magnetic circuit of one flux loop, as shown in Fig. 4.2, is composed of one-half of two magnets and the associated rotor and stator back iron behind the magnet halves. The magnetic field due to current in the slots is not considered in Fig. 4.2 since it does not contribute to the force and back emf generated. In the figure,  $R_r$  and  $R_s$  are the reluctances of the rotor and stator back irons, respectively,  $2R_g$  is the reluctance of the one-half of the air gap with compensation for slotting,  $\phi_r/2$  is the flux source of one-half of a magnet,  $2R_m$  is the reluctance of one-half of a magnet,  $R_{ml}$  is the reluctance modeling the flux leakage from magnet to magnet, and  $\phi_g/2$  is the air gap flux flowing through one-half of the air gap cross-sectional area. The reluctance of the non-magnetic gap formed by the adhesive holding the magnet to the rotor back iron is assumed to be included in  $R_r$ .

By considering  $R_r$  and  $R_s$  to be negligible with respect to  $R_g$  and  $R_{ml}$ , the magnet circuit can be simplified as shown in Fig. 4.3. Figure 4.3a shows  $R_r$  and  $R_s$  eliminated, and Fig. 4.3b adds the two magnet models in series and expresses all reluctances in terms of their equivalent permeances. Noting that  $P_{ml}$  can be combined with the magnet permeance  $P_m/4$  leads to Fig. 4.3c where  $\tilde{P}_m = P_m + 4P_{ml}$ . The remaining magnetic circuit resembles that considered in the Chap. 2 example in Fig. 2.23. By flux division the air gap flux is related to the magnet flux by

$$\frac{\phi_g}{2} = \frac{P_g/4}{P_g/4 + \tilde{P}_m/4} \frac{\phi_r}{2} \quad (4.2)$$

$$\phi_g = \frac{1}{1 + \tilde{P}_m/P_g} \phi_r$$

Given expressions for  $\tilde{P}_m$  and  $P_g$  the geometrical significance of (4.2) can be illustrated. These permeances can be computed with reference

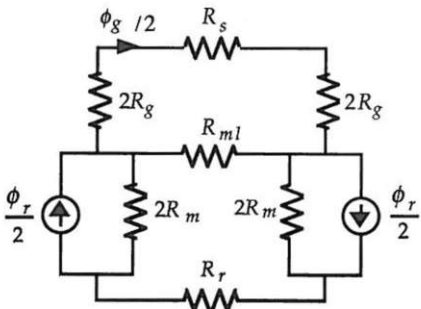
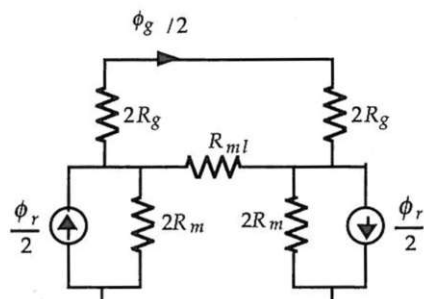
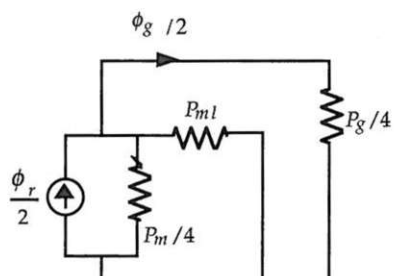


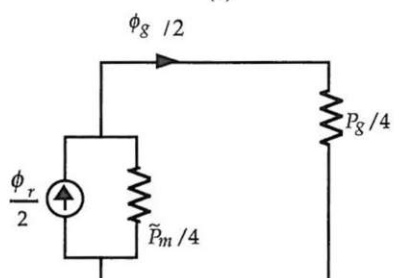
Figure 4.2 A magnetic circuit model for the structure in Fig. 4.1.



(a)



(b)



(c)

**Figure 4.3** Simplifications of the magnetic circuit in Fig. 4.2.

to Fig. 4.4. Figure 4.4a shows a section of the motor over one pole pitch. From this figure the magnet permeance is

$$P_m = \frac{\mu_R \mu_0 \alpha_m \tau_p L}{l_m} \quad (4.3)$$

where  $\alpha_m = \tau_m / \tau_p$  is the magnet fraction and  $L$  is the depth of the air gap into the page. An approximation to the magnet leakage flux is shown in Fig. 4.4b. This flux path shape is similar to that shown in

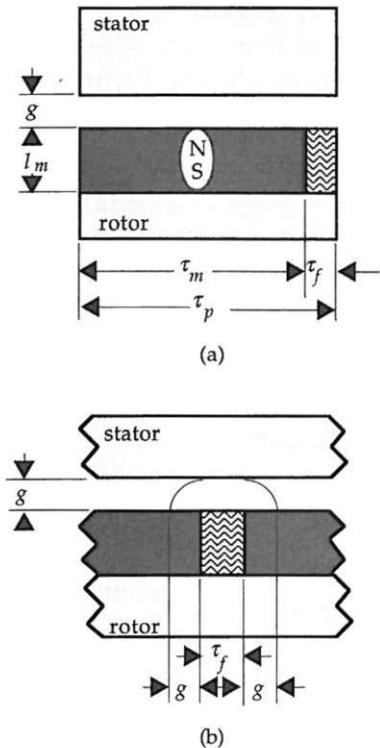


Figure 4.4 Magnet geometry and magnetic leakage flux.

Fig. 2.9, which from (2.11) gives a circular-arc straight-line permeance of

$$P_{ml} = \frac{\mu_0 L}{\pi} \ln \left[ 1 + \pi \frac{g}{(1 - \alpha_m)\tau_p} \right] \quad (4.4)$$

Combining (4.3) and (4.4) gives the effective magnet permeance of

$$\tilde{P}_m = P_m + 4P_{ml} = P_m k_{ml} \quad (4.5)$$

where the magnet leakage factor  $k_{ml}$  is

$$k_{ml} = 1 + 4 \frac{P_{ml}}{P_m} = 1 + \frac{4l_m}{\pi\mu_R\alpha_m\tau_p} \ln \left[ 1 + \pi \frac{g}{(1 - \alpha_m)\tau_p} \right] \quad (4.6)$$

Since a motor with lower magnet leakage flux gives higher performance, the closer (4.6) is to 1, the better. Based on (4.6), this occurs whenever the air gap length  $g$  is minimized with respect to the pole pitch  $\tau_p$ , or when the magnet aspect ratio  $l_m/\alpha_m\tau_p$  is minimized. In

actual application, the magnet aspect ratio is commonly kept below approximately 1/4, i.e., the magnet is at least four times wider than it is long, and the air gap length is minimized. The exact geometric values chosen are influenced by other design tradeoffs, making it impossible to identify an optimum  $\alpha_m$ .

The air gap permeance describes the net permeance seen by the magnet flux that enters the stator. Because this flux emanates from a cross-sectional area of  $(\alpha_m \tau_p - 2g)L$  and enters a stator cross-sectional area of  $\tau_p L$ , some approximation of the air gap permeance is required. Using some linear combination of these two areas in the standard permeance equation (2.6) is appropriate. Using  $\tau_p L$  overestimates the air gap permeance, whereas using  $(\alpha_m \tau_p - 2g)L$  underestimates it. To make things simple, the area is assumed to be the average of these two values, ignoring the  $-2gL$  term

$$A_g = \frac{\tau_p L(1 + \alpha_m)}{2} \quad (4.7)$$

With this approximation, the air gap permeance is

$$P_g = \frac{\mu_0 \tau_p (1 + \alpha_m) L}{2 g_e} \quad (4.8)$$

where  $g_e$  is the effective air gap length as described in Chap. 2 as

$$g_e = g k_c \quad (4.9)$$

where  $k_c$  is the Carter coefficient given by (2.12), (2.13), or (2.14). Quishan and Hongzhan (1985) have shown that when a permanent magnet appears at the air gap as shown in Fig. 4.1, the correct air gap value for computing the Carter coefficient is not the physical air gap but rather the effective length from the stator air gap surface to the rotor back iron. Thus, when computing (2.12), (2.13), or (2.14) in this case,  $g$  must be replaced by  $g + l_m / \mu_R$ .

Finally, substituting (4.3), (4.8), and (4.9) into (4.2) and simplifying gives the air gap flux as

$$\phi_g = \frac{1}{1 + \frac{2\mu_R \alpha_m k_{ml} k_c g}{(1 + \alpha_m) l_m}} \phi_r$$

This expression can be rewritten in terms of the permeance coefficient by recognizing that the flux concentration factor is given approximately by

$$C_\phi = \frac{A_m}{A_g} = \frac{\alpha_m \tau_p L}{\tau_p L(1 + \alpha_m)/2} = \frac{2\alpha_m}{1 + \alpha_m} \quad (4.10)$$

and by using the PC expression (2.27),  $P_c = l_m/(gC_\phi)$ , to give

$$\phi_g = \frac{1}{1 + \mu_R k_c k_{ml}/P_c} \phi_r \quad (4.11)$$

In terms of magnet and air gap flux densities, this expression becomes

$$B_g = \frac{C_\phi}{1 + \mu_R k_c k_{ml}/P_c} B_r \quad (4.12)$$

It is important to note that this flux density represents the average value crossing the air gap. When the stator is slotted, the actual flux density over the slots will be lower because of the longer flux path there. Taking the direction of flux flow into account, Fig. 4.5 shows a plot of the air gap flux density over a pair of magnet poles. Both the approximation given by (4.12) and a typical distribution with stator slotting are shown.

### Flux Linkage

Based on the magnetic circuit analysis conducted above, it is possible to determine the magnet flux linked by the stator phase winding as a function of rotor position. As shown in Fig. 4.1, the stator winding is formed by laying wires in the slots such that the current travels in

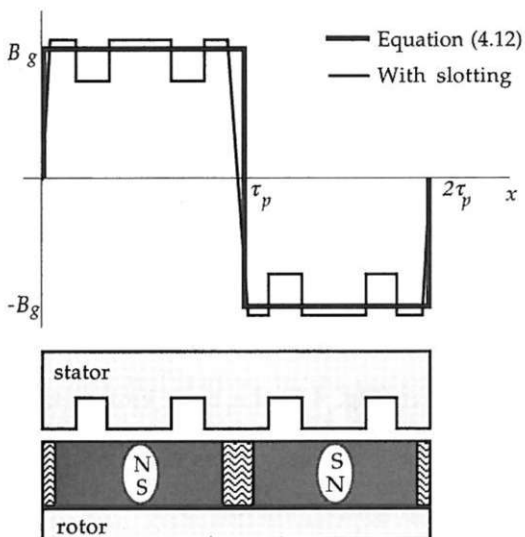


**Figure 4.5** Air gap flux density with and without slotting.

opposite directions in adjacent slots. How the wires are connected together to form the phase winding is not unique but depends upon constraints imposed by the power source used to supply the phase current. Rather than discuss these issues at this time, let the slots be wound in pairs, forming coils. Thus all the wire turns that leave the leftmost slot in Fig. 4.1 return through the center slot and those that leave the right slot return through the slot to its right (not shown). Using this simple case, the flux linkage of other configurations is found in a straightforward manner.

To determine the flux linkage as a function of position, consider the flux linked by a single coil and a pair of magnets as shown in Fig. 4.6. In Fig. 4.6a, the magnet flux linking the coil is negative and a maximum. It is a maximum because flux over one entire magnet face is passing through the coil, and it is negative because the direction of the flux is opposite to flux created by coil current. Analytically the flux linkage is equal to  $-n_s\phi_g$ , where  $n_s$  is the number of turns per slot and  $\phi_g$  is air gap flux as given by (4.11). In Fig. 4.6b, no net magnet flux is linked by the coil since one-half of the flux travels in each direction through the coil. In Fig. 4.6c, the magnet flux is a positive maximum  $n_s\phi_g$ . Between these points, the flux linked varies approximately linearly with deviations due to the magnet spacers, magnet to magnet flux leakage, and stator slotting. The exact flux linkage distribution with respect to position can only be determined by more rigorous analysis, e.g., using finite element analysis. Using this linear approximation, the spatial flux linkage distribution is shown in Fig. 4.7. The (a), (b), and (c) designations at the bottom of the figure are associated with the corresponding rotor positions shown in Fig. 4.6.

The period of the flux linkage waveform is defined as the electrical period of the motor. This distance is equal to  $2\pi$  electrical radians as defined in Chap. 1 and is physically equal to twice the pole pitch  $\tau_p$ . Therefore, one pole pitch is equal to  $\pi$  electrical radians as shown in Fig. 4.7. In addition, if there are a total of  $N_m$  magnets interacting with  $N_m/2$  coils all connected in series, the flux linked has a peak value  $N_m/2$  times greater than that shown in the figure.

## Back EMF

Given the flux linkage distribution in Fig. 4.7, the back emf voltage induced in a stator coil due to the magnet flux crossing the air gap is found by applying (3.9). Rewriting (3.9) using the chain rule for differentiation gives

$$e_b = \frac{d\lambda}{dt} = \frac{dx}{dt} \frac{d\lambda}{dx} = v \frac{d\lambda}{dx} \quad (4.13)$$

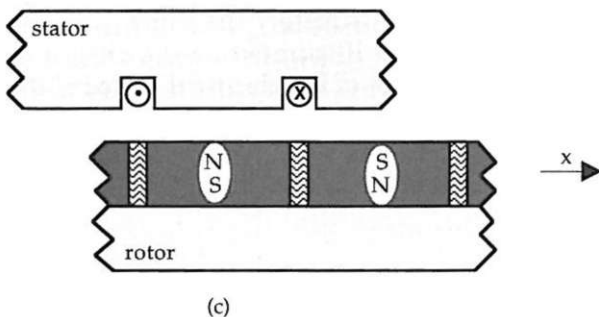
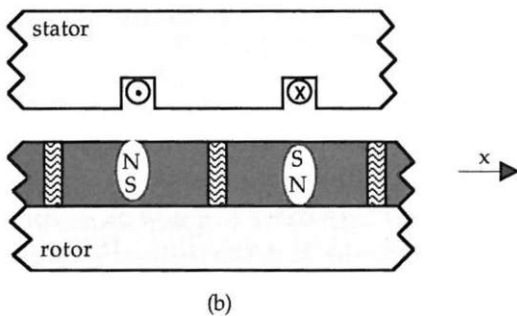
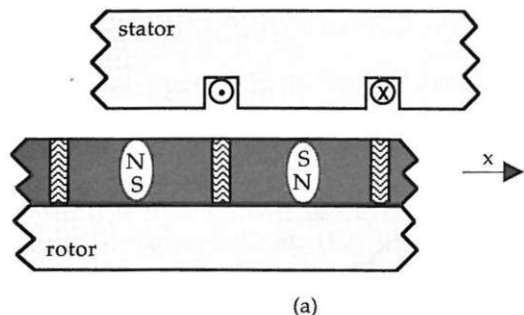


**Figure 4.6** Relative motion of the rotor.

Thus back emf is given by the product of velocity and the rate of change in flux linkage with respect to position. Applying (4.13) to the distribution shown in Fig. 4.7 and assuming that there are  $N_m$  magnets and  $N_m/2$  coils connected in series gives the back emf distribution shown in Fig. 4.8. Here, the magnitude of the back emf is

$$|e_b| = E_b = \frac{N_m}{2} \frac{2n_s \phi_g}{\tau_p} v = N_m n_s B_g L v \quad (4.14)$$

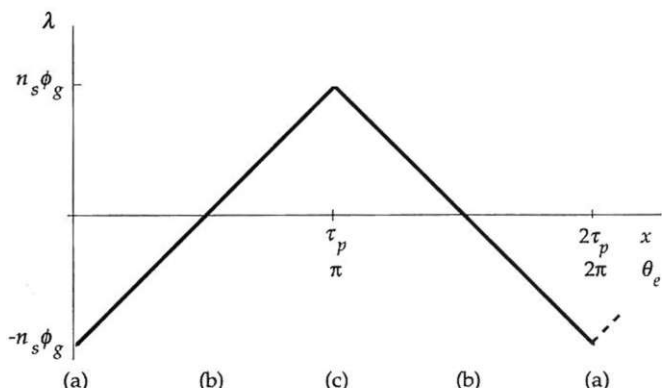


Figure 4.7 Flux linkage due to rotor motion.

where  $\phi_g = B_g \tau_p L$  has been used in the last form. Since the flux linkage shown in Fig. 4.7 applies to  $N_m/2$  coils of  $n_s$  turns, (4.14) and Fig. 4.8 also apply to  $N_m/2$  coils. Clearly (4.14) is simply an application of the  $BLv$  law discussed in Chap. 3, where there are now  $N_m n_s$  conductors exposed to  $B_g$  over a length  $L$  moving at a velocity  $v$ . The (a), (b), and (c) designations in Fig. 4.8 are associated with the corresponding rotor positions shown in Fig. 4.6.

Since the flux linkage distribution is only approximately linear, the back emf distribution shown in Fig. 4.8 exists in the ideal case only. The actual distribution has approximately the same peak amplitude but has smoother transitions, as illustrated by the shaded curve in Fig. 4.8. Furthermore, the concept of the electrical period of the motor makes intuitive sense now, since the back emf is an electrical signal having a period of  $2\pi$  electrical radians.

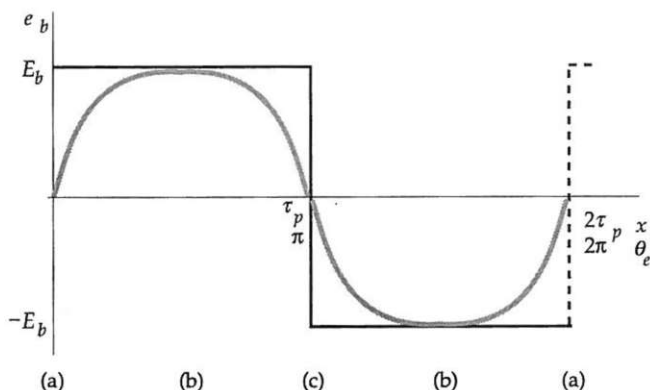


Figure 4.8 Induced back emf due to rotor motion.

## Force

The force generated in the  $x$  direction by the linear motor is easily computed using both the macroscopic and microscopic approaches. In the macroscopic case, the force is equal to (3.24) with the obvious change in interpretation from torque to force. The benefit of this approach is that it describes all three possible sources of force. The microscopic approach, on the other hand, gives only the mutual force produced as described by (3.26). In addition to these two approaches, (3.28) can be used once the back emf is known.

Since the back emf is known, application of (3.28) gives a force distribution identical to the back emf distribution as shown in Fig. 4.9 with a magnitude of

$$|f_m| = F_m = N_m n_s B_g L_i \quad (4.15)$$

where  $i$  is the current flowing in the coil. As before the (a), (b), and (c) designations in Fig. 4.9 are associated with the corresponding rotor positions shown in Fig. 4.6. In addition inspection of (4.15) reveals that it is simply the application of the  $BLi$  law discussed in Chap. 3. By comparing these two figures, the generation of force becomes apparent. Current flowing in the coil in Fig. 4.6 produces a magnetic field directed away from the air gap according to the right-hand rule; i.e., the stator surface at the air gap is a magnetic south pole. With this in mind, the left magnet in Fig. 4.6a is attracted to the magnetic south pole, generating positive force as shown in Fig. 4.9. For the position shown in Fig. 4.6c, the rotor and stator are aligned and the force is zero. In addition, deviations from this position create a restoring force, given by the sign change at (c) in Fig. 4.9, that drives the rotor and stator

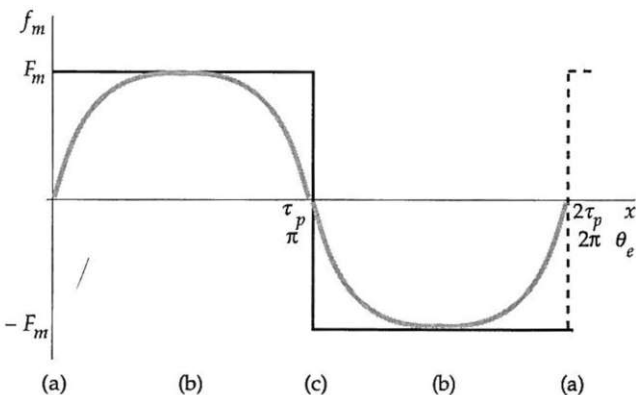


Figure 4.9 Force generated due to rotor motion.

back into alignment. This phenomenon was first discussed qualitatively in Chap. 1, where the zero force points are called detent positions.

Before moving on, it is important to note that Fig. 4.9 represents an idealization. In reality, the force will not have areas where its slope is infinite, but rather the force will have finite slope just as the back emf does. These characteristics are due to the finite spacing between the magnets, flux leaking from magnet to magnet, and stator slotting. The shaded curve in Fig. 4.9 represents a more realistic force distribution.

### Multiple phases

Figures 4.8 and 4.9 along with (4.14) and (4.15) describe the back emf and force generated due to current in slots. From Fig. 4.9 it is clear that smooth motion is not possible with this simple setup since the force generated is zero periodically. To generate continuous motion it must be possible to generate unidirectional force at all times. The fact that the force is negative one-half of the time in Fig. 4.9 is not a problem, as positive force can be generated by changing the direction of current flow in the winding at the appropriate time.

The trick to producing unidirectional force is to add additional current-carrying slots to the stator that are physically offset from one another such as that shown in Fig. 4.10. This figure shows a two-phase motor section, where additional slots are placed halfway between those of the original slots. The force and back emf due to this phase winding are identical to that of the original winding, except that it is shifted in position by  $\tau_p/2$  as shown in Fig. 4.11. Now unidirectional force can be produced because current can be applied to whichever phase winding is not at or near a detent position.

This multiple-phase trick works whenever the number of phases is greater than one, with two- and three-phase motors being the most common in practice. Since all phases have the same back emf and force distributions, it is convenient to continue this analysis by considering just one phase as shown in Fig. 4.1.

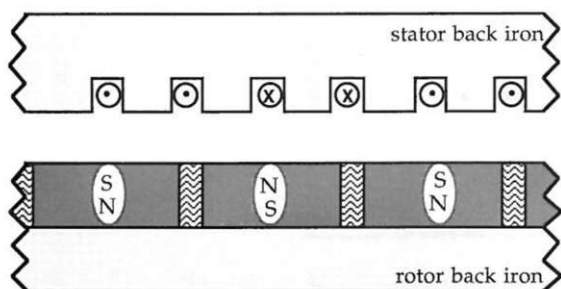
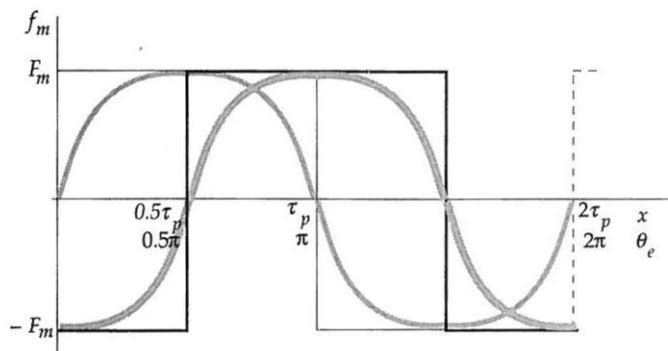


Figure 4.10 A two-phase motor structure.



**Figure 4.11** Force generated due to two phases.

### Winding Approaches

Before considering specific winding approaches it is convenient to define the winding terms turn, coil, and group (Liwschitz-Garik and Whipple, 1961). Two conductors exposed to the air gap flux make one turn. One turn is usually composed of a single wire making a loop so that both ends of the turn meet. A coil is composed of one or more series-connected turns all linked to the same flux. Thus multiple turns through the same pair of slots make one coil. All coils from a single phase that interact with the flux of a single rotor magnet are called a group. With this definition, the total number of groups in a motor is equal to the product of the number of phases and the number of rotor poles.

As shown in Fig. 4.1, it is assumed that the stator is constructed with one slot for each magnet and for each phase, i.e., one slot per pole per phase. As a result, each slot contains the windings of a single phase only. It is also assumed that all the coils making up a single phase winding are connected in series. Connection in parallel is possible but not common in practice because any mismatch in the back emf induced in each parallel coil leads to loss, producing circulating currents among the coils. This phenomenon is best understood with the help of the circuit shown in Fig. 4.12, where each parallel branch in the circuit represents a distinct coil in the motor. The simplification of this circuit, shown in Fig. 4.12b, shows that the coil-to-coil circulating current  $i_c$  is due to the net back emf voltage between the coils  $e_{b1} - e_{b2}$ . These are two primary ways that this voltage is nonzero. If the two coils occupy different slots under the same magnet pole, their respective back emf's will be out of phase with each other, giving a nonzero net voltage. On the other hand, if the coils occupy different slots under different magnet poles, the back emf's may have different amplitudes depending on the amount of mismatch in the magnetization of the two

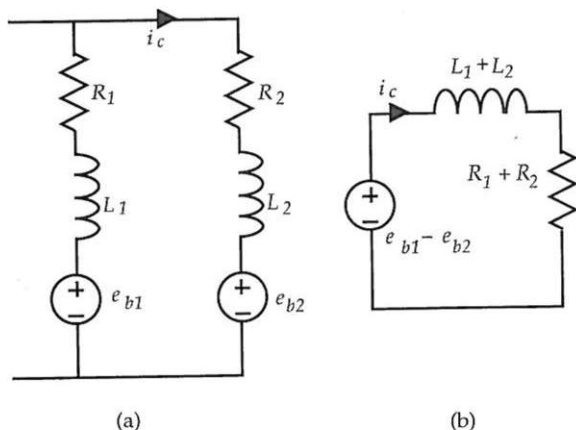


**Figure 4.12** Circuit model of parallel-connected windings.

magnets. Although any mismatch in the coil back emf's is typically small, the resulting circulating current nonetheless does produce ohmic loss in the coil resistance that can be easily avoided.

Given these restrictions, there are numerous ways to wind a motor since the back emf and force distributions shown in Figs. 4.8 and 4.9 are strictly a function of the windings in the slots and not a function of how the windings are treated beyond the slot ends, i.e., in the end turns. Think about it: The  $BLi$  law doesn't know or even care about the end turns; it only cares about what happens to the windings in the slots.

In general, the winding of a single phase can be composed of single- or double-layer coils and have a lap or wave topology (Liwschitz-Garik and Whipple, 1961; Nasar, 1987). Three possible winding approaches used in brushless PM motors are the single-layer lap winding, the double-layer lap winding, and the single-layer wave winding. The actual winding approach chosen for a given motor is a function of many things including economics. For example, high-volume motor production dictates the use of an approach that can be mechanized as opposed to an approach that requires hand winding. For a more thorough discussion of winding approaches and machine winding see Hendershot (1991) and Liwschitz-Garik and Whipple (1961).

### **Single-layer lap winding**

Top and side views of a single-layer lap winding are shown in Fig. 4.13. This is the winding approach that was considered earlier in the development of flux linkage, back emf, and force equations. The winding is single-layered because each slot contains only one coil, making

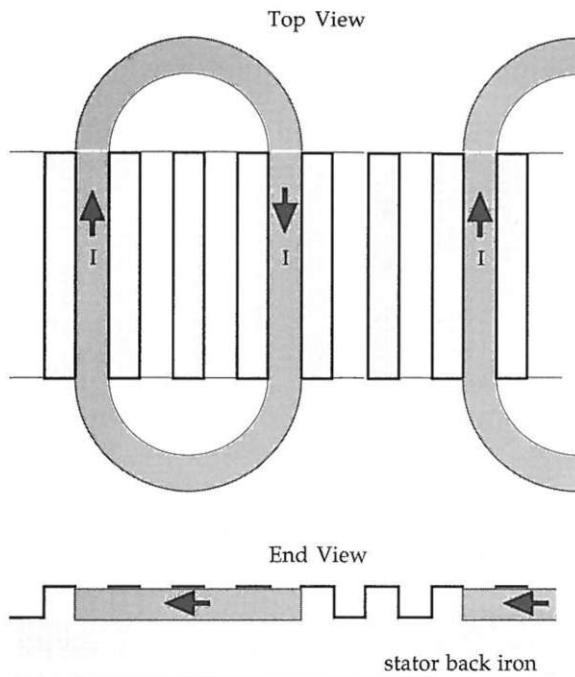


**Figure 4.13** Single-layer lap winding.

the number of turns per coil  $n_c$  equal to the number of turns per slot  $n_s$ . It is called a lap winding because each coil is composed of multiple turns with each turn lapped on top of each other. The phase winding is completed by connecting the individual coils in series.

### Double-layer lap winding

Top and side views of a double-layer lap winding are shown in Fig. 4.14. This winding is said to be double-layered because each slot of a single phase contains two coils carrying current in the same direction. As before, it is called a lap winding because each coil is composed of multiple turns with each turn lapped on top of each other. Since there are two coils per slot, the number of turns per slot  $n_s$  is equal to twice the number of turns per coil  $n_c$ . In this winding, the end turns are distributed on both ends of the motor.

### Single-layer wave winding

Top and side views of a single-layer wave winding are shown in Fig. 4.15. In this case, the winding is composed of a single multiple-turn coil that snakes its way alternately back and forth through the slots of a single phase. As a result, the number of turns per coil and the

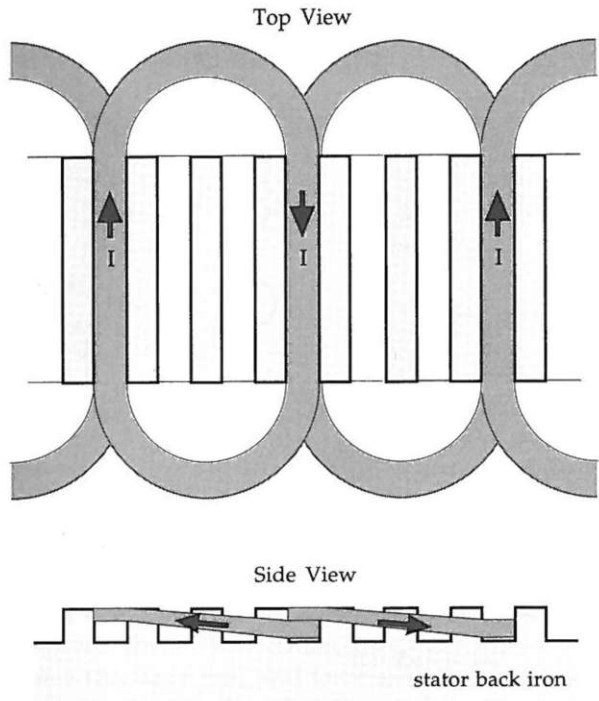


**Figure 4.14** Double-layer lap winding.

number of turns per slot are equal. In addition, as opposed to the lap winding, the end turns alternate from one end of the motor to the other.

### Self Inductance

The inductance of a phase winding is related to the energy or coenergy stored in the magnetic field generated solely by current flowing in the winding. Since the magnets on the rotor generate flux independent of the winding current, they do not contribute to the self inductance. An example of the current-induced magnetic field is shown in Fig. 4.16. As given in Table 3.1, if the energy or coenergy stored in the magnetic field can be computed, (3.15) can be used to find the self inductance. Clearly, there are several components to the winding self inductance because there is (co)energy stored in four distinct areas. These areas are the back iron, the air gap, the slots, and the end turns. Rather than sum the (co)energy stored everywhere and find the total self inductance, it is common to find the individual inductances, then sum them as necessary to get the total self inductance.

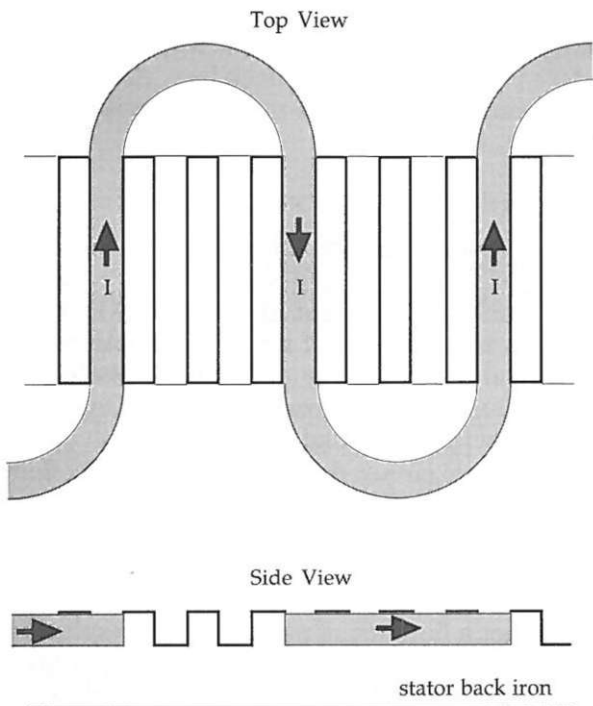


Figure 4.15 Single-layer wave winding.

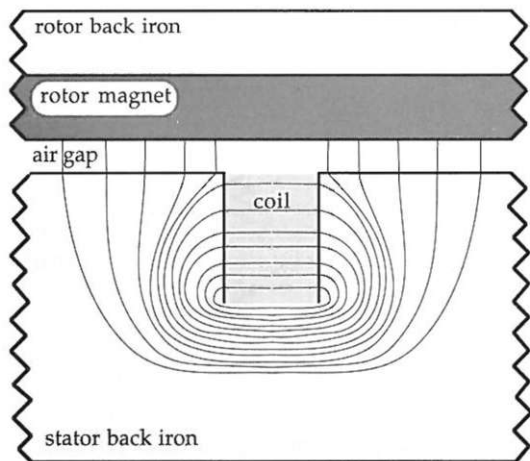


Figure 4.16 Magnetic field distribution due to coil current.

Of the individual components, the inductance due to the magnetic field in the back iron is insignificant compared with the other areas because of the high relative permeability of the back iron. As a result, the three major components contributing to the self inductance are the air gap, the slots, and the end turns.

### Air gap inductance

Air gap inductance is defined as the inductance due to flux crossing the air gap as shown in Fig. 4.16. The air gap inductance of a single coil can be found using a number of different approaches, which all lead to the same result given the same set of initial assumptions. In this work, the air gap inductance is found by determining the reluctance seen by the coil due to flux flowing across the air gap. Once this is determined, the air gap inductance is found by applying (3.3). With reference to Fig. 4.1, the magnetic circuit describing air gap flux flow due to coil current is shown in Fig. 4.17a. The magnet flux source does not appear in this circuit because it does not contribute to the self inductance. In addition, since the magnets and the spacers between them have essentially the same relative permeability, the magnet reluctance  $R_m$  in Fig. 4.17a is not a function of position. As a result, the air gap inductance itself is a constant and not a function of position. By assuming as before that the rotor and stator relative permeabilities are high, the rotor and stator back iron reluctances are zero and the circuit simplifies to that shown in Fig. 4.17b.

Given the magnetic circuit shown in Fig. 4.17b, the air gap inductance of a single coil, or pair of slots, is found using (3.3) as

$$L_g = \frac{n_s^2}{2(R_g + R_m)}$$

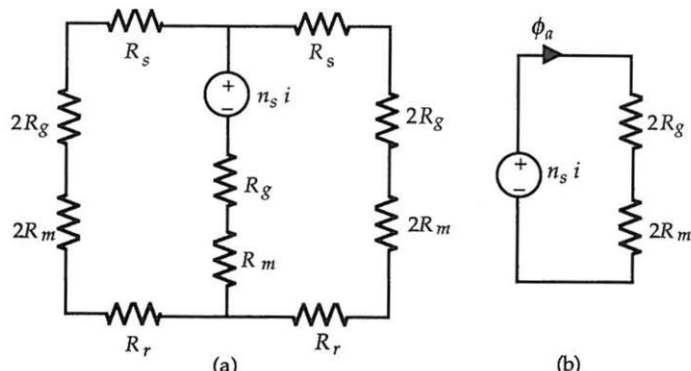


**Figure 4.17** Magnetic circuits for computing air gap flux due to coil current.

Substituting the air gap reluctance and lumping the magnet spacer reluctance in with the magnet reluctance, this equation becomes

$$L_g = \frac{n_s^2 \mu_R \mu_0 L \tau_p}{2(l_m + \mu_R g_e)} \quad (4.16)$$

The total air gap inductance is found by multiplying (4.16) by the number of coils connected in series  $N_m/2$ . It is worth noting that the air gap inductance is relatively small because of the low recoil permeability and large length of the PM with respect to the air gap.

### Slot leakage inductance

The magnetic field crossing through the windings in the slot, as shown in Fig. 4.16, is yet another component of the winding self inductance. This inductance, called the slot leakage inductance, is highly dependent upon the slot shape and the distribution of the windings in the slot (de Jong, 1989; Liwschitz-Garik and Whipple 1961; Nasar, 1987). For simplicity, only rectangular-shaped slots are considered at the present time. The slot leakage inductance of other slot geometries is easily computed once the basic rectangular slot leakage inductance is understood.

Several assumptions are required to calculate slot leakage inductance. The first is that the turns are uniformly distributed throughout the slot area. A second assumption is that the magnetic field crosses the gap parallel to the rotor-stator air gap as shown in Fig. 4.16. Given these assumptions, there are two general ways to compute the slot leakage inductance. One approach integrates the incremental inductance or permeance to find the total inductance, while the other uses the coenergy approach described earlier. The latter approach is based on the coenergy equality

$$W_c = \frac{1}{2} L i^2 = \int_{\text{vol}} \frac{1}{2} \mu_0 H^2 dV$$

By computing the rightmost coenergy expression above over the slot volume, the slot leakage inductance per slot is given by

$$L_s = \frac{\int_{\text{vol}} \mu_0 H^2 dV}{i^2} \quad (4.17)$$

Consider the rectangular slot cross section shown in Fig. 4.18. The mmf at the top of the slot is equal to  $n_s i$ , while at the bottom of the slot the mmf is zero. Using these facts and the fact that the turns are

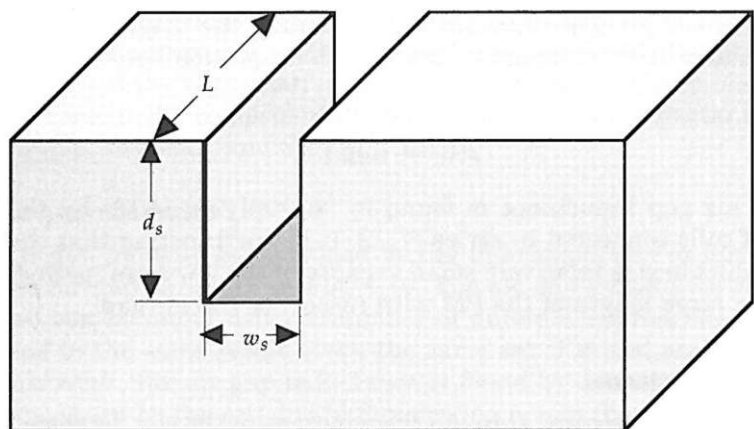


Figure 4.18 Generic slot geometry.

uniformly distributed in the slot, the magnetic field intensity crossing the slot increases linearly from the slot bottom to the slot top. Therefore, the slot field intensity can be written as

$$H(x) = \frac{n_s i}{w_s} \frac{x}{d_s} \quad (4.18)$$

where  $x$  is the distance from the bottom of the slot. Substitution of (4.18) into (4.17) and simplifying leads to the slot leakage inductance expression per slot of

$$L_s = \left( \frac{n_s^2}{3} \right) \frac{\mu_0 d_s L}{w_s} \quad (4.19)$$

This expression makes sense because a comparison with (3.3) shows that the slot leakage inductance is equal to one-third the product of the square of the number of terms and the slot permeance  $\mu_0 d_s L / w_s$ . The factor of one-third appears simply because the magnetic field is not constant over the slot height but rather increases linearly as given by (4.18). The total slot leakage inductance is the sum of that due to all slots that are wound in series. For the construction considered here, the total slot leakage inductance is  $N_m$  times larger than that given in (4.19).

### End turn leakage inductance

The magnetic field about the coil not contained in the slots, i.e., the end turns, is the last term contributing to the coil self inductance. The value of this end turn leakage inductance is difficult to determine

because the layout of the end turns is subject to few restrictions and a set magnetic field distribution is impossible to define. As a result, the end turn inductance is often roughly approximated, e.g., Liwschitz-Garik and Whipple (1961).

The approach followed here for computing end turn leakage inductance is to use the coenergy approach, expressed by (4.17), and to assume that the magnetic field is distributed about the end turns in the same way that it is about an infinitely long cylinder having a surface current  $I$ , as illustrated in Fig. 4.19.

If the current  $I$  is equal to  $ni$ , then from (4.17) the inductance of a section of the cylinder of length  $Z$  out to a radius  $R$  is

$$L = \frac{\mu_0 Z n^2}{2\pi} \ln \left( \frac{R}{r} \right) \quad (4.20)$$

Application of this expression to find the end turn leakage inductance requires finding appropriate values for  $Z$ ,  $R$ , and  $r$ . If the end turns are semicircular as shown in Fig. 4.20, then these parameters can be approximated by

$$Z = \frac{\pi \tau_p}{2}$$

$$R = \frac{\tau_p}{2}$$

$$r_s = \sqrt{\frac{d_s w_s}{\pi}} \quad (4.21)$$

$$r_d = \sqrt{\frac{d_s w_s}{2\pi}}$$

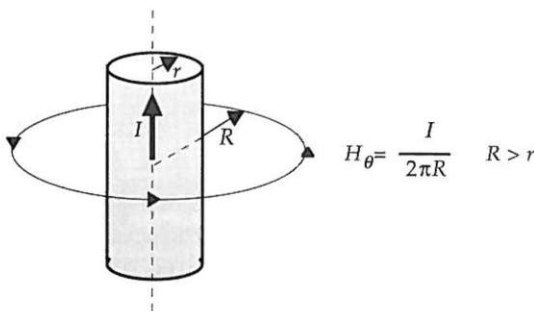


**Figure 4.19** Magnetic field about a cylindrical conductor.

## Mutual Inductance

The mutual inductances between the phases of a brushless PM motor are typically small compared with the self inductance. Just as the self inductance has three components, the mutual inductance does also. Of these components, the air gap mutual inductance is the most significant. The mutual slot leakage inductance is negligible because of the relatively high permeability of the stator teeth and back iron, and the end turn mutual inductance is extremely difficult to model because end turn placement is not well defined and the field distribution about the windings is difficult to define. As a result, only the air gap mutual inductance will be discussed here.

Mutual inductance is defined in terms of the flux linked by one coil due to the current in another. Air gap mutual inductance is a function of the relative placement of the slots and therefore is a function of the number of phases in the motor. In general, mutual inductance of the  $j$ th phase due to current in the  $k$ th phase is

$$M_{jk} = \left. \frac{\lambda_j}{I_k} \right|_{I_j=0} \quad (4.24)$$

Given (4.24), air gap mutual inductance can be found based on winding topology and symmetry. For simplicity, only the two- and three-phase cases will be considered because they are the most common in applications. Mutual inductances for motors with more than three phases follow the same reasoning but require more careful analysis.

Consider the two-phase motor as shown in Fig. 4.21, where  $\phi_a$  is the air gap flux created by current flowing in phase  $a$ . This flux couples to phase  $b$  in such a way that one-half is coupled in one direction and the other half is coupled in the opposite direction. Thus the net flux coupled

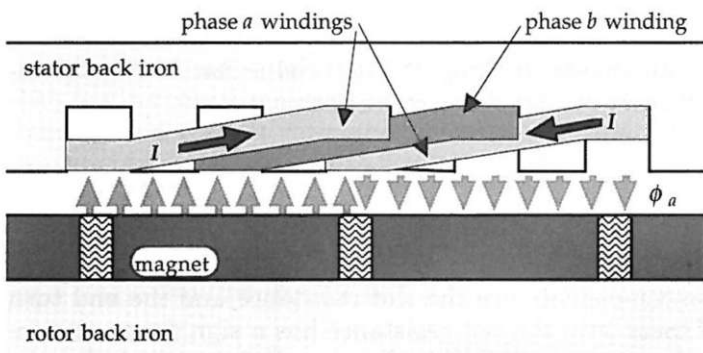
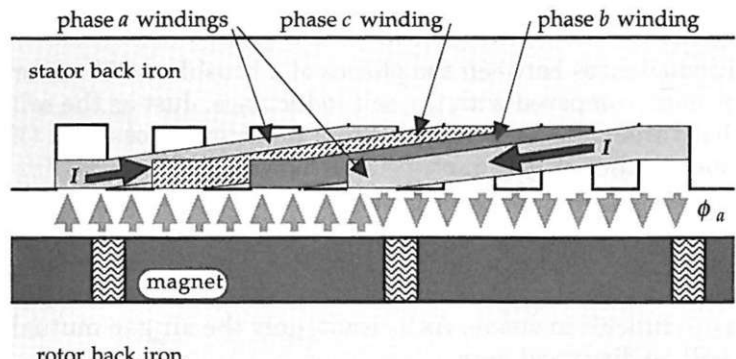


Figure 4.21 Mutual coupling between two phases.



**Figure 4.22** Mutual coupling among three phases.

to phase *b* is zero and the air gap mutual inductance is zero. Consequently, the mutual inductance of a two-phase motor has an end turn contribution only, which is extremely difficult to determine.

For the three-phase case, consider Fig. 4.22. Here the air gap flux created by current flowing in phase *a* is coupled to phases *b* and *c* such that two-thirds of the flux is coupled in one direction and one-third is coupled in the opposite direction. Thus the net flux linked to the other phases is one-third that linked to phase *a* itself. Since the self inductance of phase *a* is linearly related to the flux created by phase *a*, the ratio of the air gap mutual and self inductances is one-third (Miller, 1989), i.e.,

$$M_g = \frac{L_g}{3} \quad (4.25)$$

By symmetry, this equation applies to all phases of the motor. For motors with more phases, the mutual inductance is clearly different between different phases, making the determination of mutual inductance straightforward but more cumbersome.

## Winding Resistance

The resistance of a motor winding is composed of two significant components. These components are the slot resistance and the end turn resistance. Of these two, the slot resistance has a significant ac component, while the end turn resistance does not. Before considering the ac component, it is beneficial to consider the dc winding resistance.

## DC resistance

Resistance in general is given by the expression

$$R = \frac{\rho l_c}{A_c} \quad (4.26)$$

where  $l_c$  is the conductor length,  $A_c$  is the cross-sectional area of the conductor, and  $\rho$  is the conductor resistivity. For most conductors, resistivity is a function of temperature that can be linearly approximated as

$$\rho(T_2) = \rho(T_1)[1 + \beta(T_2 - T_1)] \quad (4.27)$$

where  $\rho(T_1)$  is the resistivity at a temperature  $T_1$ ,  $\rho(T_2)$  is the resistivity at a temperature  $T_2$ , and  $\beta$  is temperature coefficient of resistivity. For annealed copper commonly used in motor windings,  $\rho(20^\circ\text{C}) = 1.7241 \times 10^{-8} \Omega \cdot \text{m}$ , and  $\beta = 4.3 \times 10^{-3} \text{ }^\circ\text{C}^{-1}$ .

Using (4.26), the slot resistance of a single slot containing  $n_s$  conductors connected in series is

$$R_s = \frac{\rho n_s^2 L}{k_{cp} w_s d_s} \quad (4.28)$$

where  $L$  is the slot length,  $w_s$  and  $d_s$  are the slot width and height, respectively, and  $k_{cp}$ , the conductor packing factor, is the ratio of cross-sectional area occupied by conductors to the entire slot area. Although at first it doesn't seem appropriate for the resistance to be a function of the square of the number of turns, (4.28) is correct because there are  $n_s$  conductors, each occupying  $1/n_s$  of the slot cross-sectional area.

As with the end turn inductance, the end turn resistance is a function of how the end turns are laid out. By making a semicircular end turn approximation as shown in Fig. 4.20, it is possible to closely approximate the end turn resistance. Inspection of Figs. 4.13, 4.14, and 4.15 shows that the total end turn resistance of the single- and double-layer winding configurations is equal. While the single layer wave winding has half as many end turn bundles, it has twice as many turns per bundle, and the net resistance is essentially the same. Therefore, a wave winding is assumed in the following calculation of end turn resistance.

Each end turn bundle has  $n_s$  conductors having a maximum length of  $0.5\pi r_p$ . Thus application of (4.26) gives the approximate resistance of a single end turn bundle as

$$R_e = \frac{\rho \pi r_p n_s^2}{2 k_{cp} w_s d_s} \quad (4.29)$$

A comparison of (4.29) with (4.28) shows that the only difference between the end turn resistance and the slot resistance is the conductor length. Since the end turns do not contribute to force production but do dissipate power, it is beneficial to minimize the end turn length. This is accomplished by maximizing  $L$  and minimizing  $\tau_p$ . The total dc resistance of a motor winding is the sum of the slot and end turn components.

### AC resistance

As described in Chap. 2, when conductive material is exposed to an ac magnetic field, eddy currents are induced in the material in accordance with Lenz's law. Given the slot magnetic field as described by (4.18) and as shown in Fig. 4.16, significant eddy currents can be induced in the slot conductors. The power loss resulting from these eddy currents appears as an increased resistance in the winding.

To understand this phenomenon, consider a rectangular conductor as shown in Fig. 4.23. The average eddy current loss in the conductor due to a sinusoidal magnetic field in the  $y$  direction is given approximately by (Hanselman, 1993)

$$P_{ec} = \frac{1}{12} \sigma L w_c h^3 \omega^2 \mu_0^2 H_m^2 \quad (4.30)$$

where  $\sigma = 1/\rho$  is the conductor conductivity and  $H_m$  is the rms field intensity value. Since skin depth is defined as

$$\delta = \sqrt{\frac{2}{\omega \mu_0 \sigma}} \quad (4.31)$$

(4.30) can be written as

$$P_{ec} = \frac{L w_c h^3}{6 \sigma \delta^4} H_m^2 \quad (4.32)$$

Using this expression it is possible to compute the ac resistance of the slot conductors. If the slot conductors are distributed uniformly in the

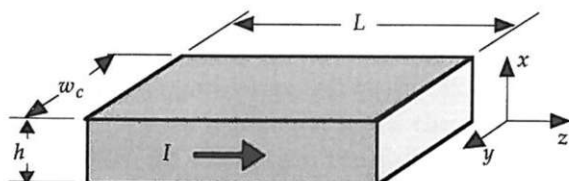


Figure 4.23 Rectangular conductor geometry.

slot, substitution of the field intensity, (4.18), into (4.32) and summing over all  $n_s$  conductors gives a total slot eddy current loss of

$$P_e = \left( \frac{d_s L h^2 n_s^2}{9\sigma\delta^4 w_s} \right) I^2 \quad (4.33)$$

where  $I$  is the rms conductor current. Since the power dissipated by a resistor is  $I^2 R$ , the fraction term in (4.33) is the effective eddy current resistance  $R_{ec}$  of the slot conductors. Using (4.28), the total slot resistance can be written as

$$R_{st} = R_s + R_{ec} = R_s(1 + \Delta_e) \quad (4.34)$$

In this equation,  $\Delta_e = R_{ec}/R_s$  is the frequency-dependent term. Using (4.28) and (4.33), this term simplifies to

$$\Delta_e \equiv \frac{R_{ec}}{R_s} = \frac{1}{9} \left( \frac{d_s}{\delta} \right)^2 \left( \frac{h}{\delta} \right)^2 \quad (4.35)$$

This result is somewhat surprising, as it shows that the resistance increases not only as a function of the ratio of the conductor height to the skin depth but also as a function of the slot depth to the skin depth. Thus, to minimize ac losses, it is desirable to minimize the slot depth as well as the conductor dimension. For a fixed slot cross-sectional area, this implies that a wide but shallow slot is best. As discussed earlier, wide slots increase the effective air gap length and increase the flux density at the base of the stator teeth. Both of these decrease the performance of the motor. Thus a performance tradeoff is identified.

## Armature Reaction

Armature reaction refers to the magnetic field produced by currents in the stator slots and its interaction with the PM field. An illustration of the armature reaction field is shown in Fig. 4.16. Ideally, the magnetic field distribution within the motor is the linear superposition of the PM and winding magnetic fields. In reality, the presence of saturating ferromagnetic material in the stator can cause these two fields to interact nonlinearly. When this occurs, the performance of the machine deviates from the ideal case discussed in the above sections. For example, if the stator teeth are approaching saturation due to the PM magnetic field alone, then the addition of a significant armature reaction field will thoroughly saturate the stator teeth. This increases the stator reluctance and the magnet-to-magnet flux leakage, which drives the PM to a lower PC and lowers the amount of force produced by the motor.

In addition to the nonlinear effects described above, the armature reaction magnetic field determines the movement of the magnet operating point under dynamic operating conditions, as depicted in Fig. 4.20 and repeated in Fig. 4.24. To illustrate this concept, consider Fig. 4.17, where  $\phi_a$  is the air gap flux due to armature reaction. This flux is superimposed over the flux emanating from the PM. Dividing this flux by the area it encompasses gives the armature reaction flux density  $B_a$ , which is easily found as

$$B_a = \frac{n_s \mu_R \mu_0}{2(l_m + \mu_R g)} i \quad (4.36)$$

Just as the air gap inductance is relatively small for a surface-mounted PM configuration,  $B_a$  is also relatively small. Typically,  $B_a$  is in the neighborhood of 10 percent of the magnet flux density crossing the air gap. The low recoil permeability and long relative length of the PM make  $B_a$  small. Depending upon the relative position of the coil and PM, the magnet operating point varies between  $(B_m - B_a)$  and  $(B_m + B_a)$ .

With reference to Figs. 4.6 and 4.24, operation at  $(B_m - B_a)$  occurs when the rotor and stator are aligned as shown in Fig. 4.6a. Likewise, operation at  $(B_m + B_a)$  occurs at an alignment as shown in Fig. 4.6c.

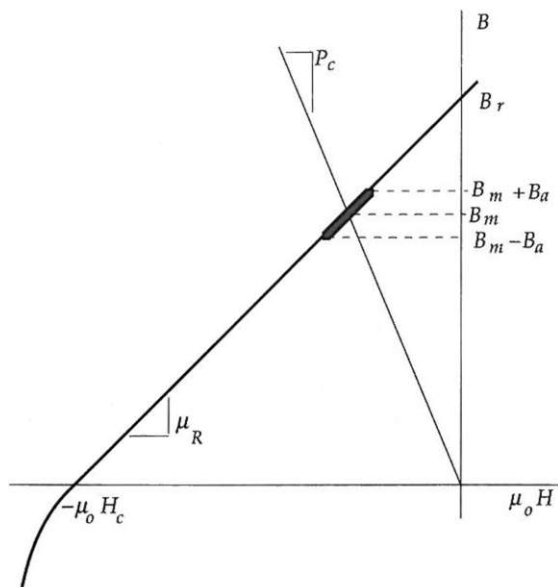


Figure 4.24 Dynamic magnet operation due to coil current.

Under normal operating conditions, the motor does not reach either of these extremes because the phase winding is normally not energized at either extreme. Under fault conditions, however, it is possible for the operating point to vary much more widely than that shown in the figure. In particular, if a fault causes the phase current to become unlimited, the armature reaction flux density (4.36) will increase dramatically and the potential for magnet damage exists.

Of the two extremes, operation at  $(B_m - B_a)$  is the most critical since irreversible demagnetization of the PM is possible if  $B_a$  is large and the PM is operating at an elevated temperature where the demagnetization characteristic has a knee in the second quadrant. In addition to possible demagnetization, the magnitude of  $B_a$  determines the hysteresis loss experienced by the PM. In the process of traversing up and down the demagnetization characteristic as the rotor moves, the actual trajectory followed is a minor hysteresis loop. The size of this hysteresis loop and the losses associated with it are directly proportional to the magnitude of the deviation in flux density experienced by the PM. Thus keeping  $B_a$  small is beneficial to avoid demagnetization and to minimize heating due to PM hysteresis loss.

Finally, in addition to the flux density crossing the air gap due to armature reaction, the slot current also generates a magnetic field across the slots as described earlier in the discussion of slot leakage inductance. Of greatest importance is the peak flux density crossing a slot. Based on Fig. 4.18 and (4.18) the peak flux density leaving the sides of the slot walls, i.e., the tooth sides, occurs at the slot top and is given by

$$|B_s|_{\max} = \frac{\mu_0 n_s}{w_s} i \quad (4.37)$$

Because flux is continuous just as current is in an electric circuit, this flux density exists within the tooth tip also. This peak value contributes to tooth tip saturation, since saturation is a function of the net field magnitude at the tooth tip, given approximately as  $(B_s^2 + B_g^2)^{1/2}$ , where  $B_g$  is the air gap flux density.

## Conductor Forces

According to the  $BLi$  law (3.26), a conductor of length  $L$  carrying a current  $i$  experiences a force equal to  $BLi$  when it is exposed to a magnetic field  $B$ . Likewise, from (3.23) force is generated that seeks to maximize inductance when current is held constant. These two phenomena describe torque and force production in motors. In addition they are useful for describing other forces experienced by the slot-bound

conductors. In this section the forces experienced by the motor windings will be discussed. The fundamental question to be resolved is "How much effort is required to keep the motor windings in the slots?" As will be shown, little effort is required because the conductors experience forces that seek to keep them there.

### Intrawinding force

Since a stator slot contains more than one current-carrying conductor, the conductors experience a force due to the interaction among the magnetic fields about the individual conductors. It is relatively easy to show that when two parallel conductors carry current in the same direction they are attracted to each other and when the current directions are opposite the conductors repel each other as shown in Fig. 4.25. This follows from the fact discussed in the example in Chap. 2, whereby the direction of motion is toward the area where the magnetic fields cancel and away from where they add. Since all conductors in a slot carry current in the same direction, the slot conductors seek to compress themselves.

### Current induced winding force

Since the windings seek to stay together in a slot, it is important to discuss the forces that act on the conductors as a whole. One source of force is the current in the winding itself. Given the discussion of slot leakage inductance and the fact that force always acts to increase inductance, it is apparent that the winding as a whole experiences a force that drives the winding to the bottom of the stator slot. This force is easily understood by considering what happens to the slot leakage inductance if the winding is pulled partway out of the slot as shown in Fig. 4.26. In this case the bottom of the slot contributes nothing to the slot inductance and the magnetic field at the top of the winding is no longer focused by the slot walls. Both of these decrease the slot leakage inductance, and thus the winding as a whole must experience a force that draws the winding into the slot. An expression for the

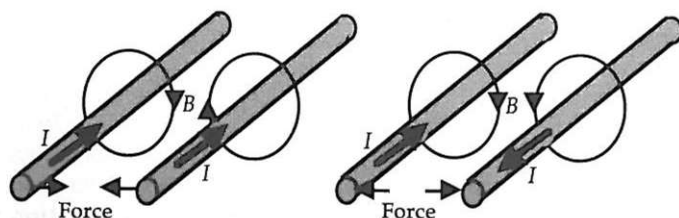


Figure 4.25 Force between current-carrying conductors.

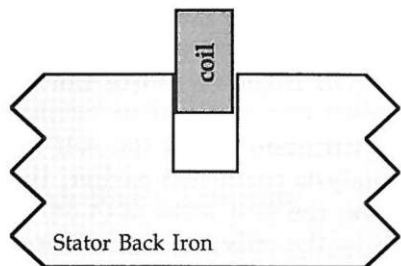


Figure 4.26 A winding partially removed from a slot.

magnitude of this force can be found in Gogue and Stupak (1991) and Hague (1962).

### Permanent-magnet induced winding force

As derived from the Lorentz force equation, the  $BLi$  rule implies that the force generated by the construction shown in Fig. 4.1 is between the PM magnetic field and the current-carrying conductors in the slots. While this interpretation gives the correct result that agrees with the macroscopic approach, the burying of conductors in slots transfers the force to the slot walls (Gogue and Stupak, 1991). That is, the conductors themselves do not experience the force generated by the PMs, but rather the steel teeth between the slots feel the pull. As a result, the windings are not drawn out of the slots by the PMs.

### Summary

To summarize, when windings appear in the slots in a motor, they do not experience any great force trying to pull them out. On the contrary, current flow in the conductors promotes their cohesion and generates a force driving them away from the slot opening, toward the slot bottom.

### Cogging Force

In the force derivation considered earlier, only the mutual or alignment force component was considered. In an actual motor, force is generated due to both reluctance and alignment components as described by Eq. (3.24) for the rotational case. For the translational case considered here, (3.24) can be rewritten as

$$F = \frac{1}{2} i^2 \frac{dL}{dx} - \frac{1}{2} \phi_g^2 \frac{dR}{dx} + Ni \frac{d\phi_g}{dx} \quad . \quad (4.38)$$

The last term in (4.38) is identical to (3.27) and is the alignment force of the linear motor. The first two terms in (4.38) are reluctance com-

ponents for the coil and magnet, respectively. Since these reluctance forces are not produced intentionally, they represent forces that must be eliminated or at least minimized so that ripple-free force can be produced.

The first term in (4.38) is due to the variation of the coil self inductance with position. Based on the analysis conducted earlier, the coil self inductance is constant. Therefore, the first term in (4.38) is zero, leaving the second term in (4.38) as the only reluctance force component. Because of its significance, this force is called cogging force and is identified as

$$F_{\text{cog}} = -\frac{1}{2} \phi_g^2 \frac{dR}{dx} \quad (4.39)$$

where  $\phi_g$  is the air gap flux and  $R$  is the net reluctance seen by the flux  $\phi_g$ . The primary component of  $R$  is the air gap reluctance  $R_g$ . Therefore, if the air gap reluctance varies with position, cogging force will be generated. Based on this equation, cogging force is eliminated if either  $\phi_g$  is zero or the variation in the air gap reluctance as a function of position is zero. Of these two, setting  $\phi_g$  to zero is not possible since  $\phi_g$  must be maximized to produce the desired motor alignment force. Thus cogging force can only be eliminated by making the air gap reluctance constant with respect to position. In the next chapter, techniques for cogging force reduction will be considered in depth.

On an intuitive level, cogging force is easy to understand by considering Fig. 4.27. In this figure, the rotor magnet is aligned with a maximum amount of stator teeth and the reluctance seen by the magnet flux is minimized, giving a maximum inductance. If the magnet is moved slightly in either direction, the reluctance increases because more air appears in the flux path between the magnet and stator back

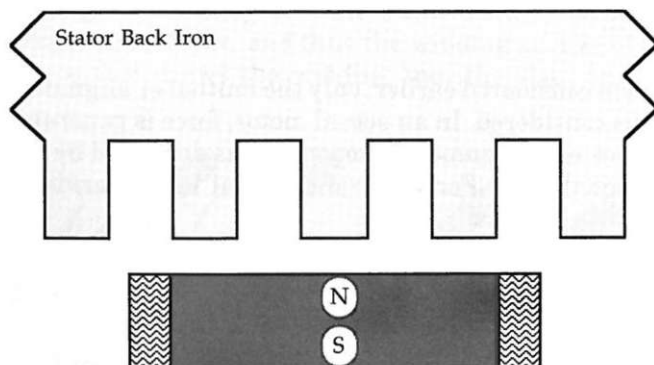


Figure 4.27 Cogging force due to slotting.

iron. This increase in reluctance generates a force according to (4.39) that pushes the magnet back into the alignment shown in the figure. This phenomenon was first discussed in Chap. 1, where a rotating magnet seeks alignment with stator poles as shown in Fig. 1.6.

### Rotor-Stator Attraction

In addition to the  $x$ -direction alignment and cogging forces experienced by the rotor, rotor-stator attractive force is also created by the topology shown in Fig. 4.1. That is, an attractive force is generated that attempts to close the air gap and bring the rotor and stator into contact with each other. This force is given by an expression similar to the cogging force expression (4.39),

$$F_{rs} = \frac{1}{2} F_g^2 \frac{dP_g}{dg}$$

In this situation, however, the force is proportional to the rate of change of the air gap permeance with respect to the air gap length. By assuming that the air gap permeance is modeled as  $P_g = \mu_0 A_g / g$ , the above equation can be simplified to give the attractive force per square meter as

$$f_{rs} = \frac{B_g^2}{2\mu_0} \quad (4.40)$$

where  $B_g$  is the air gap flux density.

The force density given by (4.40) is substantial. In applications, the rotor and stator are held apart mechanically. Thus, in some motor topologies, this force creates mechanical stress that must be taken into account in the design. However, in many topologies, this force is balanced by an equal and opposite attractive force due to symmetry. In this case, the mechanical stress is ideally zero but in reality is greatly reduced.

### Core Loss

The power dissipated by core loss in the motor is due to the changing magnetic field distribution in the stator teeth and back iron as the rotor moves relative to the stator and as current is applied to the stator slots. Since the magnetic field in the rotor is essentially constant with respect to time and position, it experiences no core loss. The amount of core loss dissipated can be computed in a number of different ways depending upon the desired modeling complexity. The simplest method

is to assume that the flux density in the entire stator volume experiences a sinusoidal flux density distribution at the fundamental electrical frequency  $f_e$ . In this case, the core loss is

$$P_{cl} = \rho_s V_s \Gamma_{bi} \quad (4.41)$$

where  $\rho_s$  is the mass density of the stator material,  $V_s$  is the stator volume, and  $\Gamma_{bi}$  is the core loss density of the stator back iron material. This last parameter is a function of the peak flux density experienced by the material as well as the frequency of its variation. As discussed in Chap. 2, this parameter is often given graphically, as shown in Fig. 2.15.

A second approach is to consider the stator teeth and back iron separately, since they typically experience a different peak flux density. Given an estimate of these flux densities, (4.41) is applied to each partial volume separately and the results summed to give the total core loss.

Yet another method takes an even more rigorous approach (Slemon and Liu, 1990). Like the last approach, the stator teeth and back iron are considered separately. However, in this approach the hysteresis and eddy current components are considered separately. In addition, the flux density distribution is not assumed to be sinusoidal, but rather as a piecewise linear function determined by the motor geometry. Because of the significant development required, this method will not be developed here.

## Summary

This concludes the presentation of the basic theory of brushless PM motor operation and the computation of fundamental parameters. The analysis presented in the above sections provides a basis for the design of actual brushless PM motors. By simple coordinate changes, the analysis applies to both axial and radial motors. For axial motors, the magnets are positioned to direct flux in an axial direction interacting with radial, current-carrying slots. As stated earlier, this conforms to the requirements of the Lorentz force equation for the generation of circumferential force, or torque. In radial motors, the directions of the magnet flux and current are switched. Magnet flux is directed radially across an air gap to interact with current in axially oriented slots.

## Fundamental Design Issues

Before discussing specific motor topologies, it is beneficial to discuss fundamental design issues that are common to all topologies. These issues revolve around the motor force equation, (4.15), which is illus-

trated in Fig. 4.28. In addition, the product  $n_s i$  in (4.15) is recognized as the total slot current and is replaced by  $I_s$ .

Each term in the force expression in Fig. 4.28 has fundamental implications which are issues to be considered in the design of brushless PM motors. In the following, the significance of each term is discussed.

### Air gap flux density

Increasing the air gap flux density increases the force generated. The amount of flux density improvement achievable is limited by the ability of the stator teeth to pass the flux without excessive saturation. Any increase in the flux density requires an increase in the PC of the magnetic circuit or the use of a magnet with a higher remanence. Increasing the PC implies increasing the magnet length or decreasing the effective air gap length. Manufacturing tolerances do not allow the physical air gap length to get much smaller than approximately 0.3 mm (0.012 in). In addition, decreasing the air gap length increases the cogging force.

### Active motor length

The active motor length can be increased to improve the force generated. However, doing so increases the mass and volume of the motor. A further consequence is that the resistive loss also increases, since longer slots require longer wire. Therefore, increasing the motor active length does not improve power density or efficiency. As a result, motor length is often chosen as the minimum value required to meet a given force specification.

### Number of magnet poles

Increasing the number of magnet poles increases the force generated by the motor. Increasing the number of poles in a fixed area implies decreasing the magnet width to accommodate the additional magnets.

$$F_m = N_m B_g L I_s$$

The diagram illustrates the permanent magnet motor force equation  $F_m = N_m B_g L I_s$ . Five parameters are shown with arrows pointing to the equation:

- Peak Force**: Points to the leftmost term  $N_m$ .
- Number of Magnet Poles**: Points to the first term  $N_m$ .
- Active Motor Length**: Points to the second term  $B_g L$ .
- Air Gap Flux Density**: Points to the third term  $B_g$ .
- Slot Current**: Points to the fourth term  $I_s$ .

Figure 4.28 The permanent magnet motor force equation.

This increases the relative amount of magnet leakage flux, causing  $k_{ml}$  to increase, which in turn decreases the air gap flux density (4.12). Thus the increase in force does not increase indefinitely. Sooner or later the force will actually decrease with an increase in magnet poles. This implies that there is some optimum number of magnet poles.

In addition to its effect on the magnet leakage, an increase in the number of magnet poles decreases the motor pole pitch, which corresponds to shorter end turns. In turn, this implies that the end turn resistive loss and leakage inductance are minimized. All of these consequences are beneficial. Shorter end turns lead to less resistive loss, which increases efficiency and decreases the thermal management burden. The decreased inductance makes the motor easier to drive.

A further consequence of increasing the number of magnet poles is that the motor drive frequency is directly proportional to the number of poles by (1.3). This increase in the drive frequency increases the core loss in the motor since the flux in the ferromagnetic portions of the motor alternates direction at the drive frequency. This tends to decrease the motor and drive efficiency.

Yet another consequence of increasing the number of magnet poles is that the required rotor and stator back iron thickness decreases. This occurs because as the magnets become narrower the amount of flux to be passed by the back iron decreases.

To summarize, increasing the number of magnet poles is beneficial up to the point where magnet leakage flux, core loss, and drive frequency requirements begin to have a significant detrimental effect on motor performance.

### Slot current

The total slot current is the last term contributing to the motor force. Since the slot current is the product of the number of turns per slot and the current per turn, the effect of the slot current can be assessed by considering each component.

Inductance increases as the square of  $n_s$ ; therefore, the motor becomes more difficult to drive as  $n_s$  increases. On the other hand, for a given motor force, an increase in  $n_s$  can be coupled with a decrease in conductor current. This decreases the resistive winding loss, which increases the motor efficiency.

Increasing the number of turns per slot while holding the current per turn constant will increase the generated force. If the conductor size is constant, the slot cross-sectional area grows as  $n_s$  increases. This increase in slot area increases the slot fraction and the mass of the stator back iron, both of which have a detrimental effect on power density.

Increasing the slot current increases the armature reaction field. This increases the core loss in the magnets and potentially decreases the air gap flux density due to stator saturation. In addition, increasing the slot current while holding the slot cross-sectional area fixed increases the current density, which increases the resistive winding loss.

### Electric versus magnetic loading

In the above discussion, the fundamental conflict between a high air gap flux density and a high slot current appears in a number of the arguments. If one gets too high, the other must decrease. For example, as the current increases, more slot area is required to maintain constant resistive loss and the maximum air gap flux density decreases. This tradeoff can be visualized by considering Fig. 4.29, where the maximum air gap flux density and slot current are plotted vs. the slot fraction. In Fig. 4.29, the maximum air gap flux density decreases as the slot width increases because magnetic saturation limits the flux carrying capacity of the teeth. Likewise, the maximum slot current increases with increasing slot width. Since the force generated is a function of the product of the flux density and slot current, maximum force is generated when the slot fraction is somewhere near one-half (Sebastian, Slement, and Rahman, 1986).

### Dual Air Gap Motor Construction

In high power density motor design, the goal is to circumvent or improve the tradeoff between electrical and magnetic loading by finding a way to increase one in a manner that does not diminish the other. One simple method of doubling the current without decreasing the air gap flux density is to employ double air gap construction as shown in Fig. 4.30.

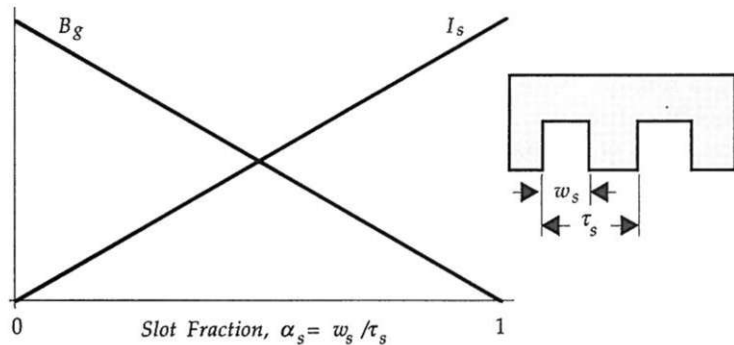


Figure 4.29 Magnetic vs. electric loading as a function of slot fraction.

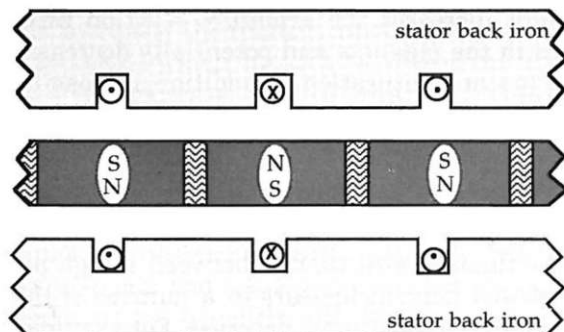
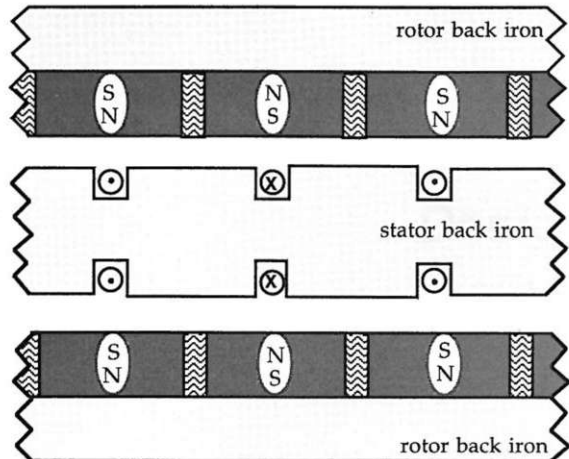


Figure 4.30 Preferable dual air gap construction.

Comparing this figure with the single air gap case in Fig. 4.1, this construction replaces the rotor back iron with a second air gap and a second stator. By doing so, the magnet flux on the opposite side of the magnets, which was not used to produce force before, is now used to produce force by interacting with slot current on the lower stator. In essence, the available slot area has doubled without changing the original air gap and stator back iron. This construction doubles the force generated because it has twice as many current-carrying turns. However, it does not significantly change the overall motor efficiency, as the resistive losses have doubled also. The power density of the dual air gap motor is greater but not double that of the single air gap motor. While the rotor back iron is replaced with another stator of approximately the same mass, the magnet length in the dual air gap motor must be twice that of the single air gap motor to maintain the same magnetic operating point or PC. Thus the doubling of the magnet mass keeps the dual air gap motor from achieving twice the power density. In terms of thermal performance, this construction does not differ from the single air gap case. By adding a second stator back iron, the area available for heat removal doubles with the doubling in slots.

Inspection of Fig. 4.30 shows that the rotor is male and the stators as a whole are female. With this in mind, it is possible to conjecture that the complementary situation, i.e., a male stator and female rotor, may offer the same performance improvement. This construction, depicted in Fig. 4.31, clearly suffers in a number of ways. First, the amount of back iron required is high, which eliminates the power density improvement achieved with the construction shown in Fig. 4.30. Perhaps more importantly, by having the stator sandwiched between the two rotors, heat removal is much more difficult. In Fig. 4.31, the heat-producing stators are separated and on the outside, where heat removal is more easily accomplished. In the alternate construc-



**Figure 4.31** Less desirable dual air gap construction.

tion, however, all the heat-producing windings are concentrated in one area and that area is isolated from the motor frame.

Despite the weaknesses of the alternate construction, one manufacturer has built motors utilizing this topology (Huang, Anderson, and Fuchs, 1990). To reduce the motor mass and regain power density, they removed the stator back iron. While this does make the alternate construction comparable in mass with the preferred construction shown in Fig. 4.30, removal of the stator back iron has two major consequences. The primary consequence is that heat removal from the stator is even more difficult because the high thermal conductivity of the stator back iron has been replaced with potting material of lower thermal conductivity. In addition, the magnet length and thus mass must be increased because the lack of stator back iron increases the effective air gap and dramatically reduces the PC.

## Summary

This concludes the discussion of brushless motor operation. In this chapter, basic assumptions were presented to define and focus the discussion toward the fundamental features of brushless PM motors. For simplicity and generality, basic motor operation was discussed in terms of a linear translational motor. From this information, fundamental design issues were identified and dual air gap construction was discussed as a way to maximize power density. Given this body of information, it is now possible to discuss common design variations.

## Design Variations

Brushless motors are seldom designed as described in Chap. 4. Numerous minor and sometimes major differences are implemented in actual motors to improve their performance in a variety of ways depending on the intended application. In this chapter, many design variations will be illustrated. Since the cylindrical, radial flux motor configuration appears so frequently, it will be used to illustrate the points made in this chapter. It is important to note that all possible design variations are not described here. There are an infinite number of variations resulting from an infinite number of assumptions and performance tradeoffs. Many of these variations are the result of years of engineering effort and insight. As a result, this chapter considers only common design variations. Based on these, the fundamental properties of most design variations can be determined.

### Rotor Variations

In Chap. 4, the rotor magnets alternated in polarity and appeared at the rotor surface. While this is a popular configuration, certainly others are possible, as shown in Fig. 5.1. In all cases, the rotor's purpose is to provide the magnetic field  $B$  for the  $BLi$  law (3.26). Cost is usually the determining factor in the choice of rotor construction. Permanent-magnet material and the handling of PMs represent a major cost item in the construction of brushless PM motors. Therefore, it is not uncommon to choose a less expensive rotor design, even if it leads to lower performance.

In Fig. 5.1a, every other magnet is replaced with an extension of the rotor back iron. Essentially, the flux from the inner south magnet poles is wrapped around to become the adjacent magnet pole at the rotor surface. This consequent pole design (Hendershot, 1991) reduces the

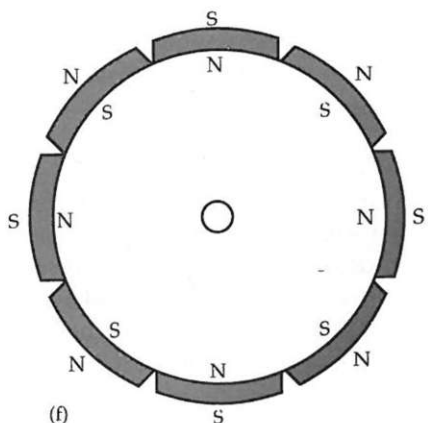
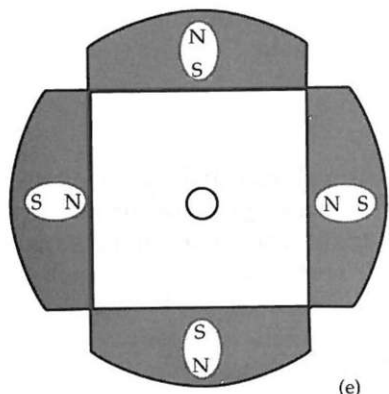
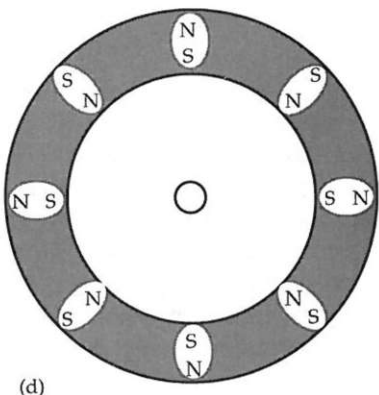
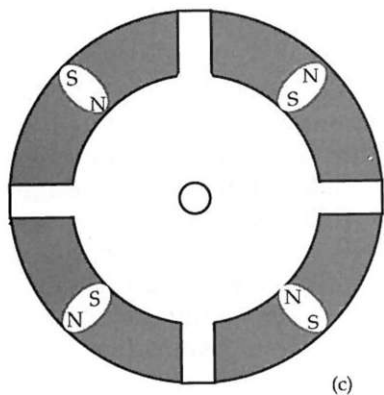
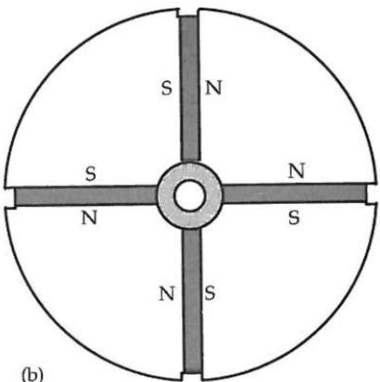
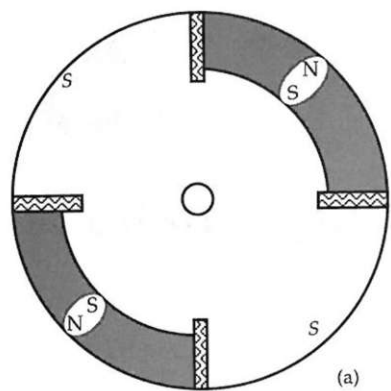


Figure 5.1 Rotor design variations.

number of magnets by one-half but requires the remaining magnets to be longer to maintain a sufficient PC. This rotor construction offers no performance enhancement but can be less expensive to produce since the number of magnets is cut by one-half. The most important magnetic difference in this configuration is that the air gap inductance is now a function of position since the permeability of the consequent poles is much greater than that of the magnets. This variation can lead to a substantial reluctance torque.

Figure 5.1b illustrates a popular form of an interior PM rotor. Here the magnets appear orthogonal to the air gap, rather than facing it, and the magnet flux is directed to the air gap through electrical steel. The primary reason for this structure is that flux concentration is possible if the surface area of the magnets exceeds that of the block of steel at the air gap. This configuration is popular when higher performance is desired when using inexpensive ferrite magnets. As with Fig. 5.1a, the air gap inductance is now at least a small function of rotor position.

In Fig. 5.1c, the nonmagnetic spacer between the magnets is replaced by electrical steel. The purpose of this steel is to add a reluctance torque component to the motor output. If designed properly, a significant improvement in motor output is possible (Sebastian and Slemmon, 1987). Based on the figure, one might think that the steel spacers act to divert substantial magnet flux away from the air gap. This is not true, however, because magnets have an anisotropic permeability that gives them a very low permeability perpendicular to the direction of magnetization.

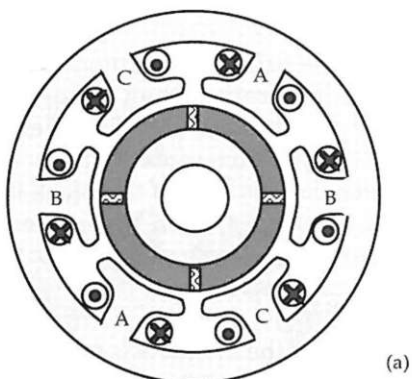
Figure 5.1d shows a rotor with no spacers at all. In this case, the rotor is constructed from a single piece of bonded magnet material, which is magnetized with alternating magnet poles to mimic the basic configuration considered originally. The primary advantage of this construction is its very low cost. With the low cost comes the low relative performance of bonded magnetic material.

Finally, Fig. 5.1e,f show two common variations of the surface-mounted magnet configuration considered in Chap. 4. Figure 5.1e shows loaf-shaped magnets and Fig. 5.1f shows magnets with parallel sides. Both of these variations exist as potentially cheaper alternatives to the more ideal radial arc magnet shown in Fig. 2.22.

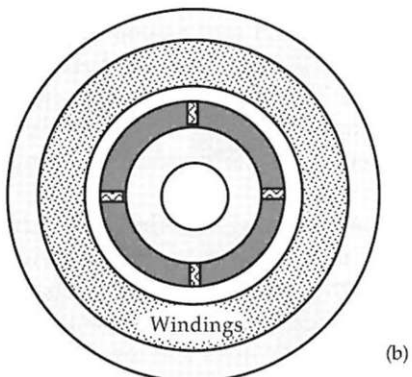
Analysis of a motor having any of these rotor constructions follows the same general approach as that described in Chap. 4. Any even number of rotor magnets can be used. Once a suitable magnetic circuit model for the rotor is found, all parameters and performance specifications can be computed. Under most circumstances, the rotor is modeled by an equivalent radial arc magnet and the analysis conducted in Chap. 4 is directly applied.

## Stator Variations

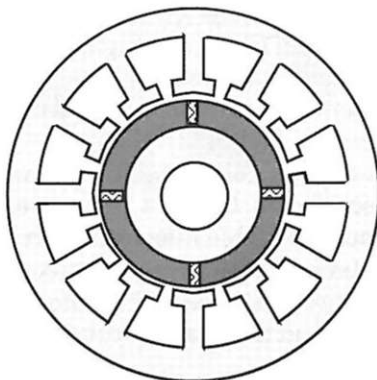
Compared with rotor variations, variations in stator construction are much more numerous and common. Some typical variations are shown in Fig. 5.2. In all cases, the stator's purpose is to guide the air gap flux past the stator windings that carry the current  $i$  for the  $BLi$  law.



(a)



(b)



(c)

Figure 5.2 Stator design variations.

Figure 5.2a shows the salient-pole or solenoidal-winding construction discussed in Chap. 1. A benefit of this construction is short end turns since windings are formed around individual poles. In addition, there is usually less coupling between phases. The disadvantage of this construction is that each phase winding does not interact simultaneously with all rotor magnets, which can lead to lower performance.

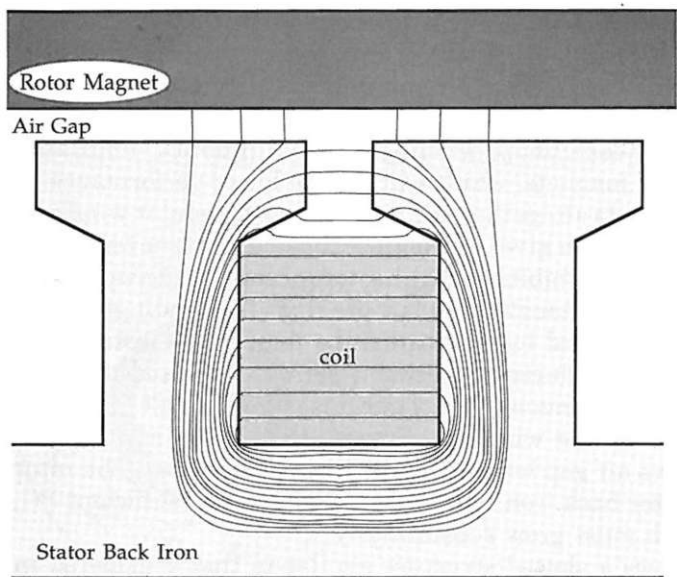
Eliminating the slots altogether and distributing the stator windings inside the stator back iron gives the slotless construction shown in Fig. 5.2b. This construction exhibits no cogging torque but does have several disadvantages. First, although there is more room for windings in this construction, the electrical loading cannot be increased substantially because the thermal conductivity between the windings and the back of the stator back iron is much lower. Thus it is more difficult to remove the heat produced by the windings. Second, the lack of stator teeth makes the effective air gap length equal to the distance from the rotor surface to the stator back iron. Therefore, to maintain a sufficient PC, the magnet length must grow substantially.

Figure 5.2c shows a slotted structure similar to that considered in Chap. 4. Here, however, the slots are not rectangular but rather have *shoes* on them at the air gap. The purpose of these shoes is to reduce the variation in air gap permeance as a function of position, thereby reducing cogging torque. This construction is so common that it will be discussed at length.

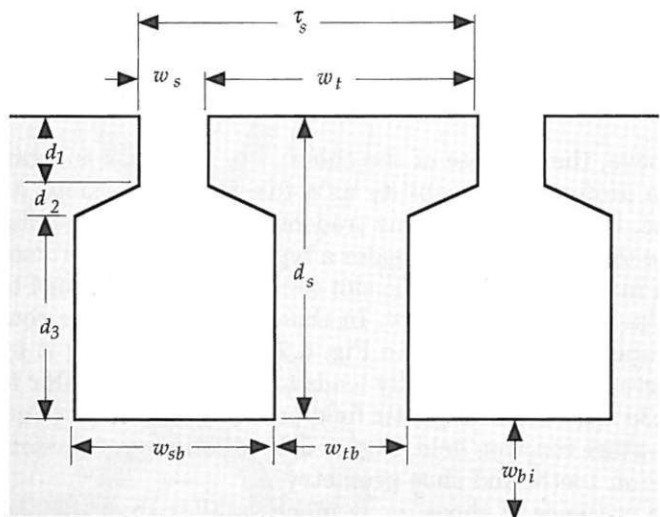
### Shoes and Teeth

As mentioned above, the purpose of the shoes is to make the air gap appear to have a uniform permeability as a function of position. As could be expected, there are numerous tradeoffs involved in shoe design. To illustrate these tradeoffs, consider a typical slot and shoe cross section as shown in Fig. 5.3, where the slot conductors are assumed to fill the rectangular portion of the slot. In those cases where the conductor area is trapezoidal as shown in Fig. 5.2c, approximating it by an equivalent rectangular area usually leads to little error. Similar to Fig. 4.16, Fig. 5.3a shows the magnetic field produced due to slot current, i.e., the armature reaction field. Figure 5.3b identifies parameters associated with slot, tooth, and shoe geometry.

Because of the presence of shoes,  $w_s$  is much smaller than the slot width at the slot bottom  $w_{sb}$ , which was the slot width considered in Chap. 4. As a result, the Carter coefficient is smaller than that discussed earlier. More importantly, the shoe area increases the slot leakage inductance. Here the slot leakage inductance has three components, the distributed inductance computed earlier (4.19), the inductance of the area leading to the shoe tip, and the inductance of



(a)



(b)

**Figure 5.3** (a) Magnetic field distribution due to coil current, and (b) associated slot geometry.

the shoe tip area. Using the inductance expression (3.3) to describe these additional areas, the total slot leakage inductance becomes

$$L_s = n_s^2 \left[ \frac{\mu_0 d_3 L}{3w_{sb}} + \frac{\mu_0 d_2 L}{(w_s + w_{sb})/2} + \frac{\mu_0 d_1 L}{w_s} \right] \quad (5.1)$$

where  $L$  is the depth of the slot into the page and  $n_s$  is the number of turns in the slot. The terms inside the brackets in (5.1) are the respective permeances of the three slot areas. The first term represents the conductor area previously derived in (4.19). The second term approximates the sloping area as a rectangular area having height  $d_2$  and average width  $(w_s + w_{sb})/2$ , and the third term is the permeance of the shoe tip area. In some texts,  $\mu_0 L$  is factored out and the terms remaining inside the brackets are called slot constants (Nasar, 1987) or normalized permeances (Liwschitz-Garik and Whipple, 1961).

Clearly, if  $w_s$  is made very small (just large enough to slide a single conductor through), the third term in (5.1) can dominate the slot leakage inductance, making the phase inductance large. This high inductance is a mixed blessing. Under fault conditions, a high inductance limits the rate of change in current since  $di/dt = v/L$ , where  $v$  is the fault voltage and  $L$  is inductance. This increases the amount of time available for any fault-detection circuitry to respond to the fault. At the same time, high inductance makes the motor harder to drive because the rate at which current can be built up in a winding is limited by the same basic phenomenon. As a result, a tradeoff exists. As  $w_s$  decreases, the air gap permeance variation decreases, but the slot leakage inductance increases.

The value of the shoe tips depends on the high permeability of the ferromagnetic material composing the shoes and teeth. As the shoe tip becomes saturated, the uniformity of the air gap permeance deteriorates. In the worst case, the shoe tips become so saturated that they essentially appear as air, in which case they serve no benefit whatsoever. As discussed in the armature reaction section of Chap. 4, the air gap flux and the slot leakage flux both contribute to shoe saturation. Here the air gap flux density  $B_g$  enters the tooth-shoe face from the air gap and the slot leakage flux crosses from shoe to shoe perpendicular to the air gap, as shown in Fig. 5-3a. Because of flux continuity the net field magnitude within the shoe tip is  $(B_s^2 + B_g^2)^{1/2}$ , where  $B_s$  is the peak slot leakage flux density given by (4.37). With reference to (4.37),  $B_s$  is inversely proportional to  $w_s$ ; thus making  $w_s$  small also increases the likelihood of shoe tip saturation. While it is not clear from this analysis, the shoe depth  $d_1 + d_2$  is also important to minimize saturation. Intuitively,  $d_1 + d_2$  must be large enough so that the air gap flux entering the shoe tip does not have to turn sharply to proceed

down through the tooth body to the back iron. Typically, the show depth fraction  $\alpha_{sd} = (d_1 + d_2)/w_{th}$  is between 25 and 50 percent. The distribution of the shoe depth between  $d_1$  and  $d_2$  is not critical, but an optimum design can be determined with the aid of finite element analysis.

### Slotted Stator Design

When a slotted stator design is chosen, there are many combinations of slots, poles, phases, and windings that lead to acceptable motor design. As stated before, the primary purpose of the stator is to provide a structure that allows the  $B$  and  $i$  in the  $BLi$  law to interact to produce usable torque. Hence just about any slotted stator structure containing almost any distribution of windings will produce torque. In this most general setting, the torque and back emf produced must be computed by applying the  $BLi$  and  $BLv$  laws, respectively, to each coil in every winding. Clearly this is an overwhelming task to perform by hand, and the resulting design may be prohibitive to manufacture because of its complexity. Therefore, in practice only organized, economical design practices are considered.

The stator design considered in Chap. 4 is the simplest both conceptually and topologically. The rotor has an even number of magnets. That is, the number of magnet poles facing the air gap  $N_m$  is even, and the number of north-south pole pairs on the rotor is  $N_p = N_m/2$ . In addition, each stator slot contains the windings of a single phase; i.e., the windings are concentrated. Furthermore, the flux from each magnet pole interacts with one slot from each phase. That is, the number of slots per pole per phase  $N_{spp}$  is one.

General stator design allows more flexibility. The primary constraint on stator design is that the total number of stator slots be some even integer multiple of the number of phases, i.e.,

$$N_s = N_{sp}N_{ph} \quad (5.2)$$

where  $N_{sp}$  is the even integer number of slots per phase. This constraint guarantees that each phase has the same number of slots. No slots are left empty, both sides of each coil have slots to pass through, and no phase windings share the same slot. Beyond this constraint, the designer has a great deal of freedom. The number of slots per pole per phase,

$$N_{spp} = \frac{N_s}{N_m N_{ph}} = \frac{N_{sp}}{N_m} \quad (5.3)$$

need not be one. It can be greater than one and have a fractional component, e.g.,  $N_{spp} = 2\frac{1}{4}$ . When a fractional part appears, the motor

is said to be a fractional slot or fractional pitch motor as opposed to integral slot or integral pitch motor. Figure 5.4 illustrates this concept for three-phase motors having four magnet poles. The motor cross section shown in Fig. 5.4a is very commonly seen in practice. It has 12 slots, giving  $N_{spp} = 12/(4 \cdot 3) = 1$ . Figure 5.4b shows a fractional slot

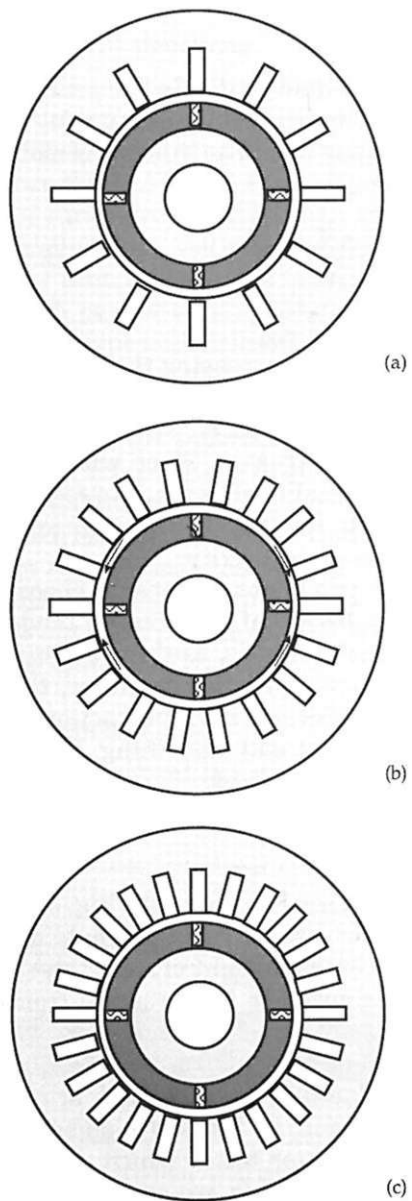


**Figure 5.4** Stators of varying slots per pole per phase: (a)  $N_{spp} = 1$ , (b)  $N_{spp} = 1.5$ , (c)  $N_{spp} = 2$ .

motor having 18 slots, or  $N_{spp} = 18(4 \cdot 3) = 1.5$ , and Fig. 5.4c shows an integral slot motor having 24 slots, or  $N_{spp} = 24/(4 \cdot 3) = 2$ .

There are several consequences of having  $N_{spp} > 1$ . When  $N_{spp} = 1$ , the number of turns per slot  $n_s$  for each phase is equal to the number of turns per pole per phase  $n_{tpp}$ . However, when  $N_{spp} > 1$ , the number of turns per phase interacting with each magnet pole is

$$n_{tpp} = N_{spp} n_s \quad (5.4)$$

Thus  $n_{tpp}$  turns produce the motor back emf and torque in the general case, not  $n_s$  as used in Chap. 4. In addition, it is sometimes useful to know the number of slots under each magnet pole. The number of slots per magnet pole is defined as

$$N_{sm} = N_{spp} N_{ph} = \frac{N_s}{N_m} \quad (5.5)$$

Clearly, when  $N_{spp}$  is fractional so is  $N_{sm}$  and  $n_{tpp}$ .

Based on the analysis conducted in Chap. 4, increasing the number of slots per pole per phase offers no apparent advantages but does have disadvantages. As  $N_{spp}$  increases, the total area of all slots remains the same but the area of individual slots decreases. Since windings tend to pack tighter in larger slots, having smaller slots tends to reduce the possible electrical loading. In addition, having more slots means having more coils, which increases winding complexity.

Despite these disadvantages, there are two major reasons for choosing  $N_{spp} > 1$ . First, as  $N_{spp}$  increases the back emf distribution tends to become more sinusoidal or more smooth. That is, as the windings of a given phase are distributed more widely around the stator, the harmonic content of the back emf decreases. Second, if  $N_{spp}$  is fractional, cogging torque is reduced in addition to back emf smoothing. These phenomena are clearly seen by considering examples.

### Fractional pitch cogging torque reduction

To illustrate cogging torque reduction, compare Fig. 5.4a with Fig. 5.4b and recall that cogging torque is produced by the rotor magnets attempting to align themselves with a maximum amount of stator steel. That is, cogging torque attempts to maximize the flux crossing from rotor to stator. In Fig. 5.4a, every rotor magnet is at the same relative position with respect to the stator teeth. Therefore, total cogging torque is equal to the algebraic sum of that produced by each magnet, or  $N_m$  times that of one magnet. On the other hand, in Fig. 5.4b, adjacent magnets are aligned differently with the stator teeth, which means the cogging torques produced by adjacent magnets are out of phase

with each other. This fact is shown in Fig. 5.4b by the arrows indicating the cogging torque direction produced by each magnet. In the ideal case, the cogging torque produced by each magnet is canceled by a net equal and opposite directed torque produced by the other magnets. In reality, this cancellation is never perfect, but a substantial reduction in cogging torque is possible.

### Back emf smoothing

To illustrate back emf smoothing due to  $N_{spp} > 1$ , compare the linear translational motor considered in Fig. 4.1 having  $N_{spp} = 1$  with the linear motor shown in Fig. 5.5 with  $N_{spp} = 2$ . Let the number of turns per slot in Fig. 5.5 be one-half that of Fig. 4.1 so that the total number of turns are equal in both cases. Using superposition, the back emf produced by the winding distribution in Fig. 5.5 is found by adding the contributions due to each pair of slots considered separately. Since each pair of slots is identical to that considered in Chap. 4, the back emf shape is identical to that found earlier with an amplitude reduction of one-half due to the fewer turns per slot here. Figure 5.6 shows the individual back emf waveforms as well as the resulting sum. The offset between the individual back emf waveforms is equal to the one slot pitch the coils are displaced. The ideal square wave assumption depicted in Fig. 5.6a does not show much visual smoothing even though Fourier analysis shows that the harmonic content is lower. However, in the realistic case where the individual back emf's have finite rise and fall times due to flux leakage as shown in Fig. 5.6b, more smoothing is apparent compared with the original back emf shown in Fig. 4.8 and repeated in Fig. 5.6c.

### Distribution factor

It is important to note that the peak back emf is equal for both  $N_{spp} = 1$  and  $N_{spp} = 2$  in the above example because the peak values of the

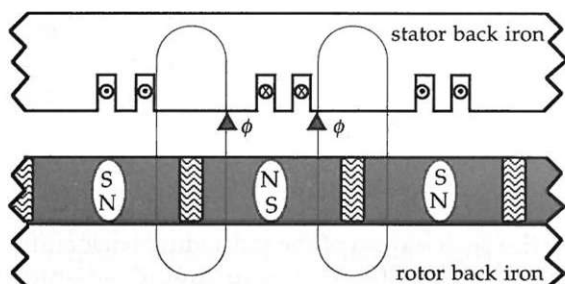
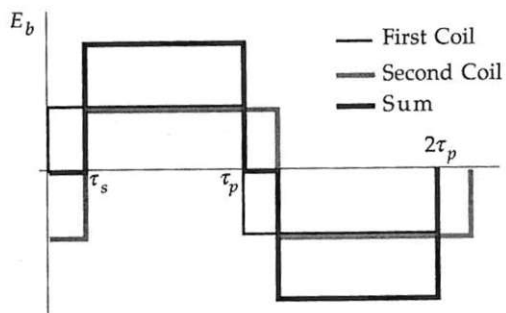
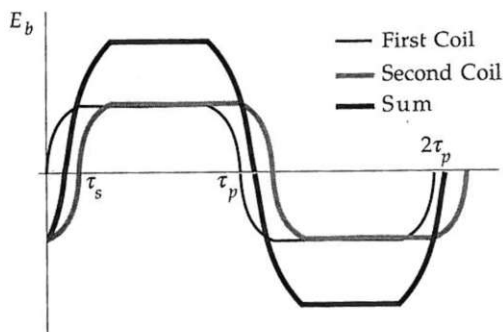


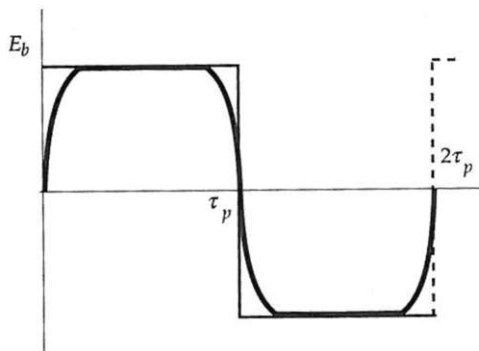
Figure 5.5 Translational motor structure having two slots per pole per phase.



(a)



(b)



(c)

**Figure 5.6** Back emf distribution due to two slots per pole per phase.

individual back emf's overlap. In reality, some reduction in peak back emf usually occurs because the peak values of the individual back emf's do not coincide as they do in Fig. 5.6c. Clearly, the amount of reduction is highly dependent on the shape of the back emf distribution. When the back emf is a pure sinusoid, the decrease in back emf is given by

the distribution factor (McPherson and Laramore, 1990; Nasar, 1987; Liwschitz-Garik and Whipple, 1961)

$$k_d = \frac{\sin(N_{spp}\theta_{se}/2)}{N_{spp} \sin(\theta_{se}/2)} \quad (5.6)$$

where

$$\theta_{se} = \frac{\pi N_m}{N_s} = \frac{\pi}{N_{spp} N_{ph}} = \frac{\pi}{N_{sm}} \quad (5.7)$$

is the slot pitch in electrical radians. For  $N_{spp} = 1$ ,  $k_d$  is equal to 1 as expected, and for the case  $N_{spp} = 2$ ,  $N_{ph} = 3$ ,  $k_d$  equals 0.966. Thus, for this latter case, the magnitude of the back emf is reduced to 96.6 percent of what it would be if the same number of turns occupied just one slot per pole per phase.

Despite the fact that (5.6) applies only when the back emf is sinusoidal, (5.6) is commonly used to approximate the back emf amplitude reduction for other distributions as well. The underlying reason for using this approximation is that it is better to have some approximation and be conservative rather than have none at all.

### Pitch factor

When  $N_{spp}$  is an integer, the distance between the sides of a given coil, i.e., the coil pitch  $\tau_c$ , is equal to the magnet pole pitch  $\tau_p$  as depicted in Fig. 5.4a. However, when  $N_{spp}$  has a fractional component, as in Fig. 5.4b, the coil pitch is less than the pole pitch and the winding is said to be *chorded* or *short-pitched*. In this case the relationship between the coil pitch and the pole pitch is given by the coil-pole fraction

$$\alpha_{cp} = \frac{\tau_c}{\tau_p} = \frac{\text{int}(N_{spp})}{N_{spp}} \quad (5.8)$$

where  $\text{int}(\cdot)$  returns the integer part of its argument. As a result of this relationship, the peak flux linked to the coil from the magnet is reduced simply because the net coil area exposed to the air gap flux density is reduced. The degree of reduction is given by the pitch factor  $k_p$ , which is the ratio of the peak flux linked when  $\tau_c < \tau_p$  to that when  $\tau_c = \tau_p$ . Because the peak flux linked determines the magnitude of the back emf through the *BLv* law (3.12), the pitch factor gives the degree of back emf reduction due to chording.

For the square wave flux density distribution considered in Chap. 4, the pitch factor is easily computed with the help of Fig. 5.7a. When  $\tau_c = \tau_p$ , the flux linked to the winding is  $\phi_g = B_g L \tau_p$ , where  $L$  is the length into the page, and when  $\tau_c < \tau_p$  the flux linked is  $\phi_g = B_g L \tau_c$ .

The ratio of these gives a pitch factor of

$$k_p = \frac{\tau_c}{\tau_p} = \frac{\theta_{ce}}{\pi} = \alpha_{cp} \quad (5.9)$$

where

$$\theta_{ce} = \pi\alpha_{cp} \quad (5.10)$$

is the coil pitch in electrical radians.

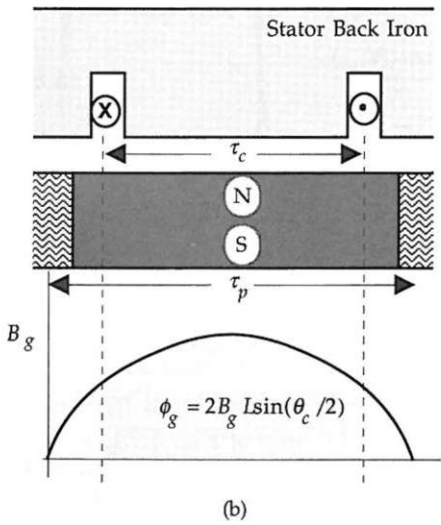
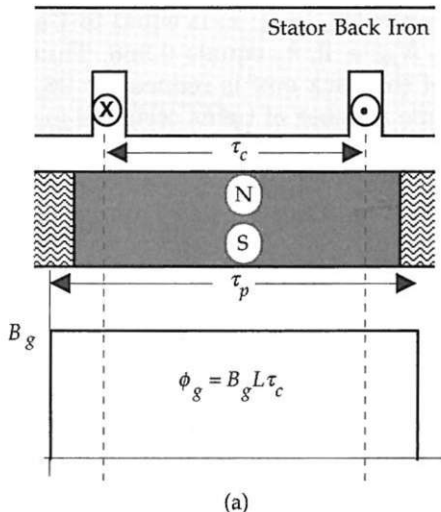


**Figure 5.7** Geometry for pitch factor computations.

For completeness, Fig. 5.7b shows the sinusoidal flux density distribution case. Using (2.2), the flux linked when  $\tau_c = \tau_p$  is  $\phi_g = 2B_g L$  and when  $\tau_c < \tau_p$  the flux linked is  $\phi_g = 2B_g L \sin(\theta_{ce}/2)$ . The ratio of these two values gives the pitch factor (McPherson and Laramore, 1990; Liwschitz-Garik and Whipple, 1961)

$$k_p = \sin\left(\frac{\theta_{ce}}{2}\right) \quad (5.11)$$

Of these two pitch factors, (5.9) gives the largest reduction in back emf amplitude. For example, if  $\alpha_{cp} = 0.75$ , (5.11) gives  $k_p = 0.92$ , whereas (5.9) gives  $k_p = 0.75$ . Thus, if the back emf deviates from sinusoidal, the use of (5.9) provides a more conservative approximation.

A final note worth making is that when  $N_{spp} > 1$ , the air gap inductance and mutual air gap inductance are reduced from what they would be when  $N_{spp} = 1$ . The slot and end turn leakage inductances remain unchanged. The degree of air gap inductance reduction is on the order of  $k_d$ . Since the air gap inductance is small with respect to the sum of the slot and end turn leakage inductances, more accurate estimation of the air gap inductance is usually not necessary. However, more accurate prediction of these inductance components can be found in Miller (1989).

## Cogging Torque Reduction

Cogging torque is perhaps the most annoying parasitic element in PM motor design because it represents an undesired motor output. As a result, techniques to reduce cogging torque play a prominent role in motor design.

As discussed in Chap. 4, cogging torque is due to the interaction between the rotor magnets and the slots and poles of the stator, i.e., the stator saliency. From (3.24) and (4.39), cogging torque is given by

$$T_{cog} = -\frac{1}{2} \phi_g^2 \frac{dR}{d\theta} \quad (5.12)$$

where  $\phi_g$  is the air gap flux and  $R$  is the air gap reluctance. Before considering specific cogging torque reduction techniques, it is important to note that  $\phi_g$  cannot be reduced since it also produces the desired motor mutual torque. More importantly, most techniques employed to reduce cogging torque also reduce the motor back emf and resulting desired mutual torque (Hendershot, 1991).

## Shoes

The most straightforward way to reduce cogging torque is to reduce or eliminate the saliency of the stator, thus the reason for considering a slotless stator design. In lieu of this choice, decreasing the variation in air gap reluctance by adding shoes to the stator teeth as shown in Fig. 5.2c decreases cogging torque. As discussed earlier in this chapter, shoes have both advantages as well as disadvantages. The primary advantage is that no direct performance decrease occurs. The primary disadvantage is increased winding inductance.

## Fractional pitch winding

Cogging torque reduction techniques minimize (5.12) in a number of fundamentally different ways. As discussed above, a fractional pitch winding reduces the net cogging torque by making the contribution of  $dR/d\theta$  in (5.12) from each magnet pole out of phase with those of the other magnets. In the ideal case, the net cogging torque sums to zero at all positions. In reality, however, some residual cogging torque remains.

## Air gap lengthening

Using the circular-arc, straight-line flux approximation, it can be shown that making the air gap length larger reduces  $dR/d\theta$  in (5.12), thereby reducing cogging torque. To keep the air gap flux  $\phi_g$  constant, the magnet length must be increased by a like amount to maintain a constant permeance coefficient operating point. Therefore, any reduction in cogging torque achieved through air gap lengthening is paid for in increased magnet length and cost and in increased magnet-to-magnet leakage flux.

## Skewing

In contrast to the fractional pitch technique, skewing attempts to reduce cogging torque by making  $dR/d\theta$  zero over each magnet face. This is accomplished by slanting or skewing the magnet edges with respect to the slot edges as shown in Fig. 5.8 for the translational case considered in Chap. 4. The total skew is equal to one slot pitch and can be achieved by skewing either the magnets or the slots. Both have disadvantages. Skewing the magnets increases magnet cost. Skewing the slots increases ohmic loss because the increased slot length requires longer wire. In addition, a slight decrease in usable slot area results. In both cases, skewing reduces and smooths the back emf and adds an additional motor output term.

Skewing can be understood by considering (5.12) and Fig. 5.8. As one progresses from the bottom edge of the magnet in the figure to the top edge, each component of  $R$ ,  $\Delta R(\theta)$  across the pole pitch  $\tau_p$  takes on all possible values between the aligned and unaligned extremes. Moreover, as the magnet moves with respect to the slots, the components of  $R$  change position, but the resulting total  $R = \sum \Delta R(\theta)$  remains unchanged. Therefore,  $dR/d\theta$  is zero and cogging torque is eliminated. Once again, in reality, cogging torque is not reduced to zero but can be reduced significantly.

As stated above, the benefits of skewing do not come without penalty. The primary penalty of skewing is that it too reduces the total flux linked to the stator windings. From Fig. 5.8, the misalignment between each magnet and the corresponding stator winding reduces the peak magnet flux linked to the coil. As before, this reduction is taken into account by a correction factor, called the skew factor  $k_s$ . For the square wave flux density distribution, the skew factor is

$$k_s = 1 - \frac{\theta_{se}}{2\pi} \quad (5.13)$$

where  $\theta_{se}$  is the slot pitch in electrical radians, (5.7). For a sinusoidal flux density distribution, the skew factor is (McPherson and Laramore, 1990; Nasar, 1987; Liwschitz-Garik and Whipple, 1961)

$$k_s = \frac{\sin(\theta_{se}/2)}{\theta_{se}/2} \quad (5.14)$$

Of these skew factors, (5.13) gives a greater reduction for a given slot pitch. However, both equations show that the performance reduction is minimized by increasing the number of slots. This occurs simply because increasing the number of slots reduces the slot pitch, which reduces the amount of skew required.

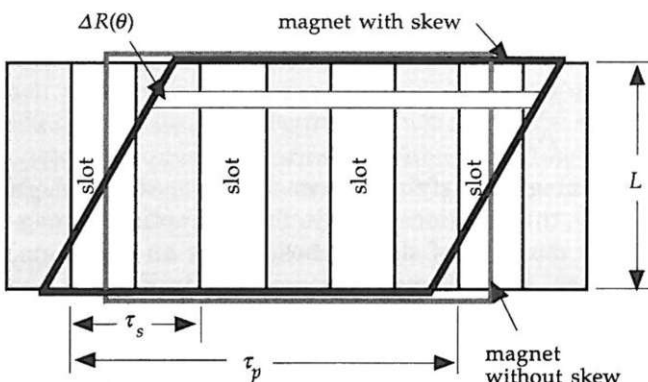


Figure 5.8 Geometry for skew factor computations.

A secondary and often neglected penalty of skewing is that it adds another component to the mutual torque, commonly a normal force (de Jong, 1989). According to the Lorentz force equation (3.25) and (4.1), the force or torque generated by the interaction between a magnetic field and a current-carrying conductor is perpendicular to the plane formed by the magnetic field and current as shown in Fig. 3.8. When magnets or slots are skewed, the force generated has two components, one in the desired direction and one perpendicular to the desired direction. In a radial flux motor as considered in this chapter, the additional force component is in the axial direction. That is, as the rotor rotates it tries to advance like a screw through the stator. This additional force component adds a small thrust load to the rotor bearings.

### Magnet shaping

Though not apparent from (5.12), magnet shape and magnet-to-magnet leakage flux has a significant effect on cogging torque (Prina, 1990; Li and Slemmon, 1988; Sebastian, Slemmon, and Rahman, 1986; Slemmon, 1991). The rate of change in air gap flux density at the magnet edges as one moves from one magnet pole to the next contributes to cogging torque. Generally, the faster the rate of change in flux density the greater the potential for increased cogging torque. This rate of change and the resulting cogging torque can be reduced by making the magnets narrower in width, i.e., decreasing  $\tau_m$ , or by decreasing the magnet length  $l_m$  as one approaches the magnet edges. In either case, the desired mutual torque decreases because less magnet flux is available to couple to the stator windings.

Detailed analysis of this approach to cogging torque reduction requires rigorous and careful finite element analysis modeling, which is beyond the scope of this text (Prina, 1990; Li and Slemmon, 1988). However, Li and Slemmon (1988) do provide an approximate expression for the optimal magnet fraction  $\alpha_m = \tau_m/\tau_p$  when the slot fraction is  $\alpha_s = w_s/\tau_s = 0.5$ ,

$$\alpha_m = \frac{n + 0.14}{N_{spp} N_{ph}} = \frac{n + 0.14}{N_{sm}} < 1 \quad (5.15)$$

where  $n$  is any positive integer satisfying the constraint  $\alpha_m < 1$ . Though not apparent from (5.15), this relationship says that the optimum magnet width is an integer multiple of slot pitches  $\tau_s$  plus an additional 14 percent of a slot pitch. For the motors considered in Fig. 5.4 the maximum optimal magnet fractions are: (a)  $(2 + 0.14)/(1 \cdot 3) = 71$  percent or 128 electrical degrees, (b)  $(4 + 0.14)/(1.5 \cdot 3) = 92$  percent, or 166 electrical degrees, and (c)  $(5 + 0.14)/(2 \cdot 3) = 86$  percent or 154 electrical degrees, respectively.

## Summary

Many of the above cogging torque reduction techniques are commonly used in motor design. Most motors have shoes and utilize skewing. Fewer employ fractional pitch windings, and fewer yet have magnets shaped for cogging torque reduction, though they may be shaped for other unrelated reasons. Because of the associated escalating magnet cost, air gap lengthening is not normally employed. Hendershot (1991) makes the point that the benefits of fractional pitch windings are not utilized as often as they should be.

## Sinusoidal versus Trapezoidal Motors

In practice there are two common forms of brushless PM motors: motors having a sinusoidal back emf, which are commonly referred to as ac synchronous motors, and trapezoidal back emf motors, most commonly called brushless dc motors. Of these, the ac synchronous motor has been around the longest, especially with wound field excitation. The brushless dc motor evolved from the brush dc motor as power electronic devices became available to provide electronic commutation in place of the mechanical commutation provided by brushes. Although both motor types span a broad range of applications and power levels, brushless dc motors tend to be more popular in lower-output-power applications.

The primary motor type considered in this text is the brushless dc motor. While the ideal motor considered in Chap. 4 has a square-wave back emf, the actual back emf has a more trapezoidal shape when magnet leakage flux is taken into account, and especially when  $N_{spp} > 1$ , thus the reason for calling it a trapezoidal back emf motor.

The ac synchronous motor differs significantly from the brushless dc motor. An ac synchronous motor has sinusoidally distributed windings, where windings from different phases often share the same slots and the number of turns per slot for a given phase winding vary as  $\sin \theta_e$ . This winding distribution guarantees that the back emf generated in each phase winding has a sinusoidal shape. Furthermore, this motor is driven by sinusoidal currents, which will be shown later to produce constant torque. Further information regarding this motor type can be found in numerous references such as Miller (1989).

## Topologies

Two topologies were identified at the beginning of Chap. 4. When magnet flux travels in the radial direction and interacts with current flowing in the axial direction, torque is produced. Likewise, magnet flux traveling in the axial direction and interacting with radial current

flow produces torque. These topologies are called radial and axial flux, respectively. The radial flux topology is the familiar cylindrical motor considered earlier in this chapter. A motor having axial flux topology is often called a pancake motor because the rotor is a flat disk.

Before developing design equations for each of these topologies, it is beneficial to qualitatively discuss them.

### **Radial flux**

The radial flux topology is by far the most common topology used in motor construction. With reference to Fig. 5.4, the strengths of this topology include: (1) rotor-stator attractive forces are balanced around the rotor so there is no net radial force on the rotor; (2) heat produced by the stator windings is readily removed because of the large surface area around the stator back iron; (3) except for skewing, the rotor and stator are uniform in the axial direction; and (4) the rotor is mechanically rigid and easily supported on both ends. Weaknesses of this topology include: (1) for a surface-mounted magnet rotor, it is not possible to use rectangular-shaped magnets; at least one surface must be arced; (2) if the motor is to operate at high speeds, some means of holding the magnets to the rotor is required; this sleeve or strapping adds to the air gap length; (3) the air gap is not adjustable during or after motor assembly; and (4) the adhesive bonding the rotor magnets to the rotor back iron forms another air gap since the adhesive is nonmagnetic.

### **Axial flux**

Historically, motors having axial flux topology are not very common. They commonly appear in applications where the motor axial dimension is more limited than the radial dimension. Although it is possible to consider an axial flux motor with a single air gap, the dual axial air gap topology as shown in Fig. 5.9 will be considered here. The strengths of this topology include: (1) by employing two air gaps, the rotor-stator attractive forces are balanced and no net axial or thrust load appears on the motor bearings; (2) heat produced by the stator windings appear on the outside of the motor, making it relatively easy to remove; (3) the magnets have two flat surfaces; no grinding to an arc shape is required; (4) no magnet retainment is required in the air gap to hold the magnets on the rotor; (5) there is no rotor back iron; (6) the air gap is adjustable during and after assembly; and (7) the stator is relatively easy to wind since it is open and flat. Weaknesses of this topology include: (1) unless the motor has many magnet poles or the outer radius is large, the winding end turn length can be sub-

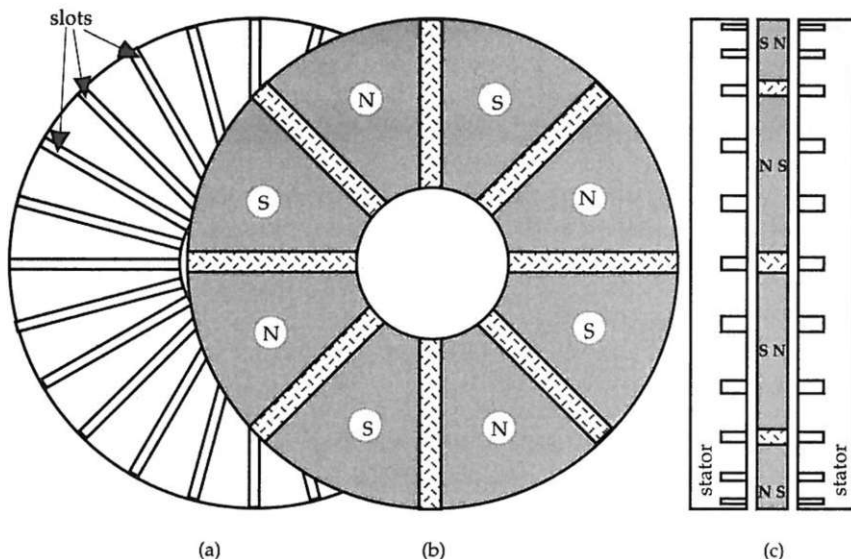


**Figure 5.9** Dual axial flux motor topology.

stantial with respect to the slot length, leading to poor winding utilization; (2) the end turns at the inner radius have a restricted volume; (3) linear skew does not eliminate cogging torque since torque is a function of radius squared; and (4) stator laminations must stack in the circumferential direction, i.e., wound as a spiral, which makes the stator expensive to manufacture.

## Conclusion

Many design variations were considered in this chapter. The motivations for these variations are numerous. Many are implemented for strictly economic reasons, while others are used to improve performance in some way or another. Many design variations were not discussed in this chapter as well, since there are as many variations as there are motors themselves. Given the body of information provided in this chapter and Chap. 4, it is possible to develop equations for the design of brushless permanent-magnet motors.

# Design Equations

The preceding chapters provide a wealth of information regarding the design of many aspects of brushless PM motors. In this chapter, this information is brought together to illustrate motor magnetic design. In the process of doing so, many additional design tradeoffs become apparent. Thus the design equations presented here add yet another layer of understanding of brushless PM motor design. To limit the scope of this work, only slotted stator designs will be considered.

The accuracy of the equations developed in this chapter is directly dependent upon the accuracy with which magnetic circuit analysis models the magnetic field distribution within the motor structure. While this is not exact, the developed design equations have sufficient accuracy for most engineering purposes. Further refinement of the design can be conducted by using finite element analysis.

It is important to note that motor design is often an iterative process. Numerous passes through the design procedure are common, with each pass conducted with different parameter values. It is through this process that a great deal of additional insight is obtained. Many tradeoffs and otherwise obscure constraints become apparent only by iteration.

## Design Approach

In the design equations that follow, the approach is to start with basic motor geometrical constraints and a magnetic circuit describing magnet flux flow. From this circuit, the magnet operating point is found, as are the important motor dimensions and current required to generate a specific motor output power at some rated speed. Given the desired back emf at rated speed, the number of turns per phase are

found. From the winding information, phase inductances and resistances are computed.

## Radial Flux Motor Design

The radial flux topology considered here is shown in Fig. 5.2c and is repeated in Fig. 6.1. Since this topology has one air gap, the magnetic circuit analysis conducted in Chap. 4 applies here. As a result, the magnetic circuits shown in Figs. 4.2 and 4.3 can be used to determine the magnetic circuit operating point.

### Fixed parameters

Many unknown parameters are involved in the design of a brushless PM motor. As a result, it is necessary to fix some of them and then determine the remaining as part of the design. Which parameters to fix is up to the designer. Usually, one has some idea about the overall motor volume allowed, the desired output power at some rated speed, and the voltage and current available to drive the motor. Based on these assumptions, Table 6.1 shows the fixed parameters assumed here.

The parameters given in the table are grouped according to function. The required power or torque at rated speed, the peak back emf, and the maximum conductor current density are measures of the motor's input and output. Topological constraints include the number of phases, magnet poles, and slots per phase. The air gap length, magnet length, outside stator radius, outside rotor radius, motor axial length, core loss, lamination stacking factor, back iron mass density, conductor resistivity and associated temperature coefficient, conductor packing factor, and magnet fraction are physical parameters. Magnet rema-

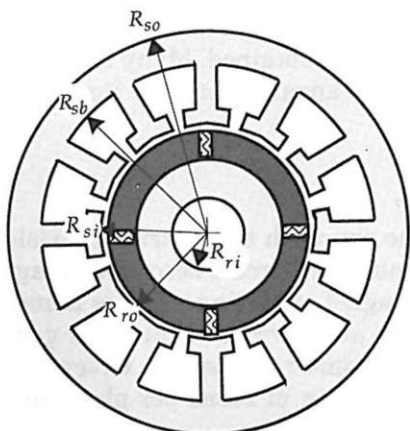


**Figure 6.1** Radial flux motor topology showing geometrical definitions.

**TABLE 6.1 Fixed Parameters for the Radial Flux Topology**

Parameter	Description
$P_{hp}$ , or $T$	Power, hp, or rated torque, N · m
$S_r$	Rated speed, rpm
$E_{max}$	Maximum back emf, V
$J_{max}$	Maximum slot current density, A/m <sup>2</sup>
$N_{ph}$	Number of phases
$N_m$	Number of magnet poles
$N_{sp}$	Number of slots per phase, $N_{sp} \geq N_m$
$g$	Air gap length, m
$l_m$	Magnet length, m
$R_{so}$	Outside stator radius, m
$R_{ro}$	Outside rotor radius, m
$L$	Motor axial length, m
$\Gamma(B, f)$	Steel core loss density vs. flux density and frequency
$k_{st}, \rho_{bt}$	Lamination stacking factor and steel mass density
$\rho, \beta$	Conductor resistivity and temperature coefficient
$k_{cp}$	Conductor packing factor
$\alpha_m$	Magnet fraction, $\tau_m / \tau_p$
$B_r$	Magnet remanence, T
$\mu_R$	Magnet recoil permeability
$B_{max}$	Maximum steel flux density, T
$w_s$	Slot opening, m
$\alpha_{sd}$	Shoe depth fraction $(d_1 + d_2)/w_{tb}$
Winding approach	Lap or wave, single- or double-layer, or other

nence, magnet recoil permeability, and maximum steel flux density are magnetic parameters. Shoe parameters include the slot opening width and shoe depth fraction. Finally, the winding approach must be specified.

Of the parameters in the table, it is interesting to note that the stator outside radius, motor axial length, and rotor outside radius are considered fixed. The stator outside radius and axial length are fixed because they specify the overall motor size. The rotor outside radius is fixed because one often wishes to either specify the rotor inertia, which increases as  $R_{ro}^4$ , or to maximize  $R_{ro}$ , since torque increases as  $R_{ro}^2$ . Clearly, as  $R_{ro}$  increases for a fixed  $R_{so}$ , the area available for conductors decreases, forcing one to accept a higher conductor current density to achieve the desired torque. Secondarily, by specifying the rotor outside radius, the design equations follow in a straightforward fashion and no iteration is required to find an overall solution.

### Geometric parameters

From the parameters given in Table 6.1 and the dimensional description shown in Figs. 6.1 and 6.2, it is possible to identify important

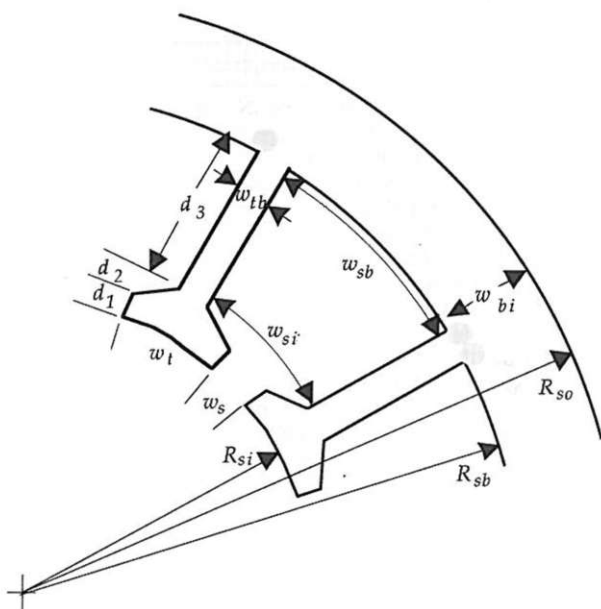


**Figure 6.2** Slot geometry for the radial flux motor topology.

geometric parameters. The various radii are associated by

$$\begin{aligned} R_{sb} &= R_{so} - w_{bi} \\ R_{si} &= R_{sb} - d_s = R_{ro} + g \\ R_{ri} &= R_{ro} - l_m - w_{bi} \end{aligned} \quad (6.1)$$

The pole pitch at the inside surface of the stator is related to the angular pole pitch by

$$\tau_p = R_{si}\theta_p \quad (6.2)$$

where

$$\theta_p = \frac{2\pi}{N_m} \quad (6.3)$$

is the angular pole pitch in mechanical radians and the coil pitch at the rotor inside radius is

$$\tau_c = \alpha_{cp}\tau_p \quad (6.4)$$

where  $\alpha_{cp}$  is given by (5.8). Likewise the slot pitch at the rotor inside radius is

$$\tau_s = R_{si}\theta_s \quad (6.5)$$

where

$$\theta_s = \frac{2\pi}{N_s} \quad (6.6)$$

is the angular slot pitch in mechanical radians. Knowledge of the slot opening gives the tooth width at the stator surface of

$$w_t = \tau_s - w_s \quad (6.7)$$

The width of the slot bottom is given by

$$w_{sb} = R_{sb}\theta_s - w_{tb} \quad (6.8)$$

Given that  $d_s = d_1 + d_2 + d_3$ , and

$$d_1 + d_2 = \alpha_{sd}w_{tb} \quad (6.9)$$

the conductor slot depth is

$$d_3 = d_s - \alpha_{sd}w_{tb} \quad (6.10)$$

and the slot cross-sectional area available for conductors is

$$A_s = d_3 \left[ \theta_s \left( R_{sb} - \frac{d_3}{2} \right) - w_{tb} \right] \quad (6.11)$$

In addition, the slot width just beyond the shoes is

$$w_{si} = (R_{si} + \alpha_{sd}w_{tb})\theta_s - w_{tb} \quad (6.12)$$

From this expression it is possible to define the slot fraction as

$$\alpha_s = \frac{w_{si}}{w_{si} + w_{tb}} \quad (6.13)$$

As shown in Fig. 6.2, the stator teeth have parallel sides and the slots do not. However, the situation where the slots have parallel sides and the teeth do not is equally valid. A trapezoidal-shaped slot area maximizes the winding area available and is commonly implemented when the windings are wound randomly (Hendershot, 1991), i.e., when they are wound turn by turn without any predetermined orientation in a slot. On the other hand, a parallel-sided slot with no shoes is more

commonly used when the windings are fully formed prior to insertion into a slot.

The unknowns in the above equations are the back iron widths of the rotor and stator  $w_{bi}$  and the tooth width  $w_{tb}$ . Given these two dimensions, all other dimensions can be found. In particular, the total slot depth is given by

$$d_s = R_{sb} - R_{ro} - g \quad (6.14)$$

which must be greater than zero. In addition, the inner rotor radius  $R_{ri}$  must be greater than zero. If either of these constraints is violated, then  $R_{ro}$  or  $R_{so}$  must be changed.

### Magnetic parameters

The unknown geometric parameters  $w_{bi}$  and  $w_{tb}$  are determined by the solution of the magnetic circuit. Because the analysis conducted in Chap. 4 applies here without modification, it will not be repeated. The air gap flux and flux density are given by (4.11) and (4.12), respectively, and can be evaluated using the fixed and known geometric parameters given above.

As discussed in Chap. 4, the flux from each magnet splits equally in both the stator and rotor back irons and is coupled to the adjacent magnets. Thus the back iron must support one-half of the air gap flux; that is, the back iron flux is

$$\phi_{bi} = \frac{\phi_g}{2}$$

If the flux density allowed in the back iron is  $B_{\max}$  from the table of fixed values, then the above equation dictates that the back iron width must be

$$w_{bi} = \frac{\phi_g}{2B_{\max}k_{st}L} \quad (6.15)$$

where  $k_{st}$  is the lamination stacking factor (2.16).

Since there are  $N_{sm} = N_{spp}N_{ph}$  slots and teeth per magnet pole, the air gap flux from each magnet travels through  $N_{sm}$  teeth. Therefore, each tooth must carry  $1/N_{sm}$  of the air gap flux. If the flux density allowed in the teeth is also  $B_{\max}$ , the required tooth width is

$$w_{tb} = \frac{\phi_g}{N_{sm}B_{\max}k_{st}L} = \frac{2}{N_{sm}} w_{bi} \quad (6.16)$$

Using (6.15) and (6.16), all geometric parameters can be found.

### Electrical parameters

The electrical parameters of the motor include resistance, inductance, back emf, and current. All of these parameters are a function of how the motor is wound. *It is assumed that no matter what winding approach is used, all coils making up a phase winding are connected in series.* This assumption maximizes the back emf and minimizes the current required per phase to produce the required rated torque.

Before any parameters can be found, it is necessary to convert the rated motor speed to radians per second using (1.4). Then, if the motor output is specified in terms of horsepower, it must be converted into an equivalent torque. Since there are 746 watts per horsepower, the equivalent torque is

$$T = \frac{746P_{hp}}{\omega_m} \quad (6.17)$$

where  $\omega_m$  is the rated mechanical speed in radians per second.

**Torque.** To find the electrical parameters, it is necessary to specify the relationship between torque and the other motor parameters. Following the derivation in Chap. 4, the torque developed by a single phase when  $N_{spp} = 1$  is found by combining (1.1) and (4.15),

$$T = (N_m B_g L n_s i) R_{ro}$$

where the product in parentheses is the force produced by the interaction of  $N_m$  magnet poles providing an air gap flux density of  $B_g$ , with each pole interacting with  $n_s$  conductors each carrying a current  $i$  exposed to  $B_g$  over a length  $L$ . In this situation, where there may be more than one slot per pole per phase,  $n_s$  must be replaced by the number of turns per pole per phase (5.4),  $n_{tpp} = N_{spp}n_s$ , which gives a torque expression of

$$T = N_m B_g L R_{ro} N_{spp} n_s i$$

If  $N_{spp} > 1$ , the air gap flux density must be modified by the distribution factor (5.6) and pitch factor (5.9). Moreover, if the magnets are skewed, the skew factor (5.13) must be included. Inclusion of these terms gives a final torque expression of

$$T = N_m k_d k_p k_s B_g L R_{ro} N_{spp} n_s i \quad (6.18)$$

**Back emf.** Now using (6.18) and the input-output power relationship  $T\omega = e_b i$  from (3.28), the peak back emf at rated speed  $\omega_m$  is

$$e_{\max} = \frac{T\omega_m}{i} = N_m k_d k_p k_s B_g L R_{ro} N_{spp} n_s \omega_m \quad (6.19)$$

from which the number of turns per slot required to produce  $E_{\max}$  is

$$n_s = \text{int} \left( \frac{E_{\max}}{N_m k_d k_p k_s B_g L R_{ro} N_{spp} \omega_m} \right) \quad (6.20)$$

where once again  $\text{int}(\cdot)$  returns the integer part of its argument because the number of turns must be an integer. Due to the truncation involved in (6.20), the peak back emf may be slightly less than  $E_{\max}$ . The actual peak back emf achieved can be found by substituting the value computed in (6.20) back into (6.19).

**Current.** Given the desired torque, the required current can be specified in a number of ways. Conductor current, slot current, phase current, or their associated current densities can be found. In addition, these can be specified when any number of phases are conducting simultaneously. Moreover, the peak or rms value can be specified. And finally, the shape of the current is a function of the back emf waveshape as well as the implemented motor drive scheme. As a result, the peak slot current and peak slot current density under the assumption that only one phase is producing the desired torque will be computed. These values represent a worst case condition, since more than one phase is usually contributing to the motor torque at one time. In addition, the phase current is computed under the assumption that all phases are contributing equally and simultaneously to the motor torque.

Solving the torque expression (6.18) for the total slot current  $I_s = n_s i$  gives

$$I_s = \frac{T}{N_m k_d k_p k_s B_g L R_{ro} N_{spp}} \quad (6.21)$$

If all  $N_{ph}$  phases are conducting current simultaneously and the back emf is a square wave as shown in Fig. 4.8, the phase current is also a square wave having a peak and rms value of

$$I_{ph} = \frac{I_s}{N_{ph} n_s} \quad (6.22)$$

This current value is useful for estimating the ohmic or  $I^2R$  losses of the motor when producing the rated output. In an actual motor the rms phase current is greater than (6.22), since the back emf is never an exact square wave. Therefore, computations using (6.22) are optimistic.

The slot current (6.21) is distributed among  $n_s$  conductors occupying the slot cross-sectional area given by (6.11). Part of this area is occupied by conductor insulation, inevitable gaps between slot conductors, and

additional insulation placed around the slot periphery, called slot liners (Hendershot, 1991). (Slot liners are used to keep the slot conductors from developing electrical shorts to the stator back iron.) As a result, only some fraction of the total cross-sectional area is occupied by slot conductors themselves. This fraction is taken into account by specifying a conductor packing factor as

$$k_{cp} = \frac{\text{area occupied by conductors}}{\text{total area}}$$

Typically  $k_{cp}$  is less than 50 percent, but it can be higher under special circumstances. The exact value of this parameter is known only through experience.

Using (6.11), (6.21), and the conductor packing factor given in Table 6.1, the slot and conductor current density is

$$J_c = \frac{I_s}{k_{cp} A_s} \quad (6.23)$$

This current density must be compared with the maximum allowable current density  $J_{\max}$  given in Table 6.1. If  $J_c$  exceeds  $J_{\max}$ , some compromise must be made. The easiest way to decrease the current density is to increase the available slot area by increasing the difference  $R_{so} - R_{ro}$ . Since a higher current density implies higher  $I^2R$  losses, the value of  $J_{\max}$  is limited only by the ability to cool the motor and the maximum allowable motor temperature. The choice of  $J_{\max}$  is usually based on past experience. For comparison purposes, typical copper residential wiring has a rated peak current density between 4 and 10 MA/m<sup>2</sup>. According to Hendershot (1991), this range of current densities is also typical for motor windings, with the lower end being acceptable for totally enclosed motors and the upper end acceptable for forced air cooled motors.

Based on the slot cross-sectional area, the number of turns required, and the conductor current density, it is straightforward to choose a wire gage suitable for the motor windings. Because of the variety of wire types, insulation types and thicknesses, and slot liners available, this additional analysis is beyond the scope of this text. Some pertinent information can be found in Hendershot (1991).

**Resistance.** The phase resistance and inductance of the motor windings are functions of the winding approach chosen, the end turn layout, and  $N_{spp}$ . The phase resistance determines the ohmic or  $I^2R$  losses of the motor, and the phase inductance determines the maximum rate of change in phase current, since  $di/dt = v_p/L$ , where  $v_p$  is the phase voltage.

Without giving any proof, it is possible to show that the total phase resistance is identical for the three winding approaches considered in Chap. 4. Intuitively, this does make sense since the number of slot conductors is invariant and all slot conductors must be connected in series to form a phase winding. As a result, a single-layer wave winding will be considered for simplicity.

Reinterpreting the slot and end turn resistances, (4.28) and (4.29), respectively, using the terminology of Chap. 5 gives

$$R_s = \frac{\rho n_s^2 L}{k_{cp} A_s} \quad (6.24)$$

$$R_e = \frac{\rho n_s^2 \pi \tau_c}{2 k_{cp} A_s} \quad (6.25)$$

where  $A_s$  is the slot cross-sectional area (6.11). Given  $N_{sp}$  slots per phase and one end turn bundle containing  $n_s$  turns per slot, the phase resistance is

$$R_{ph} = N_{sp}(R_s + R_e) \quad (6.26)$$

**Inductance.** The phase inductance has three components due to the air gap, slots, and end turns. The air gap inductance given in Chap. 4 was per pair of slots. Therefore, rewriting the air gap inductance (4.16) on a per slot basis gives

$$L_g = \frac{n_s^2 \mu_R \mu_0 L \tau_c k_d}{4(l_m + \mu_R k_c g)} \quad (6.27)$$

where  $k_d$  has been included to compensate the air gap inductance roughly for distributed windings. The slot leakage inductance given in (5.1) applied to rectangular slots. Modifications must be made for the trapezoidal slots shown in Fig. 6.2. Repeating (5.1) gives

$$L_s = n_s^2 \left[ \frac{\mu_0 d_3 L}{3w_{sb}} + \frac{\mu_0 d_2 L}{(w_s + w_{sb})/2} + \frac{\mu_0 d_1 L}{w_s} \right] \quad (6.28)$$

The first term in (6.28) is the distributed inductance of the winding area. Because the width of the slot varies with radius,  $w_{sb}$  in the denominator must be replaced with an average or effective radius. Since the slot depth of this area is  $d_3$ , the effective slot width is  $A_s/d_3$ . The second term in (6.28) is the inductance of the sloping portion of the shoe. Here  $w_{sb}$  must be interpreted as  $w_{si}$ . The final term in (6.28) is

the inductance of the shoe tip and requires no correction. Applying these corrections to (6.28) gives a slot leakage inductance per slot of

$$L_s = n_s^2 \left[ \frac{\mu_o d_3^2 L}{3A_s} + \frac{\mu_o d_2 L}{(w_s + w_{si})/2} + \frac{\mu_o d_1 L}{w_s} \right] \quad (6.29)$$

The approximate end turn inductance given by (4.22) also applies to a rectangular slot. Replacing the rectangular cross-sectional area  $d_s w_s$  with the trapezoidal cross-sectional area  $A_s$  gives

$$L_e = \frac{n_s^2 \mu_o \tau_c}{8} \ln \left( \frac{\tau_c^2 \pi}{4A_s} \right) \quad (6.30)$$

As earlier with the phase resistance, given  $N_{sp}$  slots per phase and one end turn per slot, the total phase inductance is

$$L_{ph} = N_{sp}(L_g + L_s + L_e) \quad (6.31)$$

## Performance

The performance of a motor can be measured in a variety of ways. Depending upon the intended application, a multitude of performance measures could be defined. Examples of performance measures include material cost, tooling and fabrication cost, power density, and efficiency. Of these, efficiency is fundamentally important and will be developed here.

To compute the efficiency it is necessary to compute the ohmic winding loss and the core loss. Of these, the core loss is the most difficult to compute accurately. The magnets and rotor back iron experience little variation in flux and therefore do not generate significant core loss. On the other hand, the stator teeth and stator back iron experience flux reversal on the order of  $B_{max}$  at the fundamental electrical frequency. With knowledge of  $B_{max}$  and  $f_e$ , the core loss of the stator can be roughly approximated. In reality, various areas of the stator experience different flux density magnitudes as well as different flux density waveshapes, making it difficult to use traditional core loss curves based on a sinusoidal flux density waveshape. More accurate estimation of the core loss requires rigorous analysis that is beyond the scope of this text (Slemon and Liu, 1990).

The ohmic motor loss is equal to the sum of that from each phase. Using (6.22) and (6.26), the ohmic motor loss is

$$P_r = N_{ph} I_{ph}^2 R_{ph} \quad (6.32)$$

This ohmic power loss is optimistic since it assumes an ideal square wave back emf and simultaneous square wave conduction of all phases.

Thus one can expect the ohmic loss to be significantly greater than that given in (6.32). More accurate estimation of the ohmic power loss requires knowledge of the motor drive scheme and more accurate prediction of the back emf. Adjustments to (6.32) will be made in Chap. 7.

Before considering core loss, it is interesting to consider the area over which this heat is generated. Without developing a thermal model for the motor or conducting a thermal analysis, it is at least beneficial to identify the density at which heat leaves the slot conductors and passes into the stator teeth and back iron. Using  $L(2d_3 + w_{sb})$  as the slot area in contact with the conductors, the heat density in  $\text{W/m}^2$  leaving the slot conductors is

$$q_s = \frac{P_r}{L(2d_3 + w_{sb})N_s} \quad (6.33)$$

Clearly, the greater  $q_s$  is, the higher the operating temperature of the motor will be.

Using core loss data for the stator material like that shown in Fig. 2.15, the core loss is given approximately by

$$P_{cl} = \rho_{bi}V_{st}\Gamma(B_{\max}, f_e) \quad (6.34)$$

where  $\rho_{bi}$  is the mass density ( $\text{kg/m}^3$ ) of the back iron,  $V_{st}$  is the stator volume, and  $\Gamma(B_{\max}, f_e)$  is the core loss density ( $\text{W/kg}$ ) of the stator material at the flux density  $B_{\max}$  and frequency  $f_e$ . In (6.34), the stator volume is given with sufficient accuracy by

$$V_{st} = [\pi(R_{so}^2 - R_{si}^2) - N_s A_s] L k_{st} \quad (6.35)$$

where  $A_s$  is the slot cross-sectional area given in (6.11).

Combining (3.20), (6.32), and (6.34), the efficiency of the motor producing rated torque at rated speed is

$$\eta = \frac{T\omega_m}{T\omega_m + P_r + P_{cl} + P_s} \cdot 100\% \quad (6.36)$$

where  $P_s$  is the stray loss, composed of windage, friction, and other less dominant loss components. Depending on motor speed and construction,  $P_s$  typically decreases the efficiency on the order of several percent. If desired, the loss incurred in driving the motor can be included in (6.36), giving a more realistic total system efficiency.

Finally, summing the ohmic and core losses and dividing by the stator peripheral area gives an estimate of the maximum heat density to be removed from the motor:

$$q_{st} = \frac{P_r + P_{cl}}{2\pi R_{so} L} \quad (6.37)$$

### Design procedure

The material presented so far provides information that can be used to design radial flux brushless PM motors. It is only necessary to choose the correct equations, evaluate them in the correct order, and understand the limits of their applicability. To facilitate this process, the required equations are organized in this section. Starting with the given parameters in Table 6.1, a motor design can be completed by evaluating the equations shown in Table 6.2 in the order given.

### Summary

This completes the derivation of design equations for the radial flux topology. The equations presented represent one of many approaches to design. Certainly other sets of given parameters could be chosen, and other sets of assumptions could be used. Other approaches will lead to different solutions, but the general tradeoffs in all cases will be the same. The performance of a motor designed using the above guidelines will no doubt deviate from that predicted by the equations. The amount of deviation is dependent upon how closely the underlying assumptions are met. Development of more accurate design procedures and equations requires more complicated analysis that would cloud the underlying tradeoffs.

### Dual Axial Flux Motor Design

The topology of the dual axial flux motor is shown in Fig. 5.9 and is repeated in Fig. 6.3. The design of a motor having this topology is complicated by the presence of two air gaps, by the changing dimensions with radius, and by the fact that torque is produced over a continuum of radii, not just at a single radius as in the radial flux motor. It is assumed here that the windings from the two stators are connected in series to maximize the back emf.

### Magnetic circuit analysis

Magnetic circuit analysis of a dual air gap topology closely follows that of the single air gap case considered in Chap. 4. Here, following the construction shown in Fig. 4.30, repeated in Fig. 6.4, is the magnetic circuit shown in Fig. 6.5. This magnetic circuit is similar to that shown in Fig. 4.2, except for the additional air gap, magnet leakage, and stator. Steps in the simplification of the magnetic circuit are shown in Fig. 6.6. In Fig. 6.6a, the stator back iron reluctances are ignored

TABLE 6.2 Design Equations for the Radial Flux Topology

No.	Expression	Description
(1.4)	$\omega_m = (\pi/30)S_r$	Mechanical speed, rad/s
(1.3)	$\omega_e = (N_m/2)\omega_m$	Electrical speed, rad/s
(n.a.)	$f_e = \omega_e/(2\pi)$	Fundamental electrical frequency, Hz
(6.16)	$T = 746P_{hp}/\omega_m$	Torque from horsepower
(5.2)	$N_s = N_{sp}N_{ph}$	No. of slots
(5.3)	$N_{spp} = N_{sp}/N_m$	No. of slots per pole per phase
(5.5)	$N_{sm} = N_{spp}N_{ph}$	No. of slots per pole
(5.8)	$\alpha_{cp} = \text{int}(N_{spp})/N_{spp}$	Coil-pole fraction
(6.3)	$\theta_p = 2\pi/N_m$	Angular pole pitch
(6.6)	$\theta_s = 2\pi/N_s$	Angular slot pitch
(5.7)	$\theta_{se} = \pi/N_{sm}$	Slot pitch, electrical radians
(6.1)	$R_{si} = R_{ro} + g$	Inside stator radius
(6.2)	$\tau_p = R_{si}\theta_p$	Pole pitch
(6.4)	$\tau_c = \alpha_{cp}\tau_p$	Coil pitch
(6.5)	$\tau_s = R_{si}\theta_s$	Slot pitch at air gap
(6.7)	$w_t = \tau_s - w_s$	Tooth width at air gap
(5.6)	$k_d = \frac{\sin(N_{spp}\theta_{se}/2)}{N_{spp}\sin(\theta_{se}/2)}$	Distribution factor
(5.9)	$k_p = \alpha_{cp}$	Pitch factor
(5.13)	$k_s = 1 - \theta_{se}/(2\pi)$	Skew factor
(4.11)	$C_\phi = \frac{2\alpha_m}{1 + \alpha_m}$	Flux concentration factor
(2.27)	$P_c = l_m/(gC_\phi)$	Permeance coefficient
(4.6)	$k_{ml} = 1 + \frac{4l_m}{\pi\mu_R\alpha_m\tau_p} \ln \left[ 1 + \pi \frac{g}{(1 - \alpha_m)\tau_p} \right]$	Magnet leakage factor
(n.a.)	$g_c = g + l_m/\mu_R$	Effective air gap for Carter coefficient
(2.12)	$k_c = \left[ 1 - \frac{1}{\frac{\tau_s}{w_s} \left( 5 \frac{g_c}{w_s} + 1 \right)} \right]^{-1}$	Carter coefficient
(4.7)	$A_g = \frac{\tau_p L (1 + \alpha_m)}{2}$	Air gap area
(4.13)	$B_g = \frac{C_\phi}{1 + \mu_R k_c k_{ml}/P_c} B_r$	Air gap flux density
(2.3)	$\phi_g = B_g A_g$	Air gap flux
(6.15)	$w_{bi} = \frac{\phi_g}{2B_{\max}k_{st}L}$	Back iron width
(6.16)	$w_{tb} = \frac{2}{N_{sm}} w_{bi}$	Tooth width
(6.1)	$R_{sb} = R_{so} - w_{bi}$	Stator back iron radius
(6.1)	$R_{ri} = R_{ro} - l_m - w_{bi}$	Rotor inside radius
(6.8)	$w_{sb} = R_{sb}\theta_s - w_{tb}$	Slot bottom width
(6.12)	$w_{si} = (R_{si} + \alpha_{sd}w_{tb})\theta_s - w_{tb}$	Slot width inside shoes
(6.13)	$\alpha_s = \frac{w_{si}}{w_{si} + w_{tb}}$	Slot fraction inside shoes
(6.14)	$d_s = R_{sb} - R_{ro} - g$	Total slot depth

**TABLE 6.2 Design Equations for the Radial Flux Topology (Continued)**

No.	Expression	Description
(6.10)	$d_3 = d_s - \alpha_{sd}w_{tb}$	Conductor slot depth
(6.9)	$d_1 + d_2 = \alpha_{sd}w_{tb}$	Shoe depth, split between $d_1$ and $d_2$
(6.11)	$A_s = d_3[\theta_s(R_{sb} - d_3/2) - w_{tb}]$	Conductor area
(6.20)	$n_s = \text{int} \left( \frac{E_{\max}}{N_m k_d k_p k_s B_g L R_{ro} N_{spp} \omega_m} \right)$	No. of turns per slot
(6.19)	$e_{\max} = N_m k_d k_p k_s B_g L R_{ro} N_{spp} n_s \omega_m$	Peak back emf
(6.21)	$I_s = \frac{T}{N_m k_d k_p k_s B_g L R_{ro} N_{spp}}$	Peak slot current
(6.22)	$I_{ph} = \frac{I_s}{N_{ph} n_s}$	Phase current
(6.23)	$J_c = \frac{I_s}{k_{cp} A_s}$	Peak conductor current density
(4.37)	$ B_s _{\max} = \frac{\mu_o I_s}{w_s}$	Peak slot flux density
(6.24)	$R_s = \frac{\rho n_s^2 L}{k_{cp} A_s}$	Slot resistance
(6.25)	$R_e = \frac{\rho n_s^2 \pi \tau_c}{2 k_{cp} A_s}$	End turn resistance
(6.26)	$R_{ph} = N_{sp}(R_s + R_e)$	Phase resistance
(6.27)	$L_g = \frac{n_s^2 \mu_R \mu_o L \tau_c k_d}{4(l_m + \mu_R k_c g)}$	Air gap inductance
(6.29)	$L_s = n_s^2 \left[ \frac{\mu_o d_3^2 L}{3A_s} + \frac{\mu_o d_2 L}{(w_s + w_{si})/2} + \frac{\mu_o d_1 L}{w_s} \right]$	Slot leakage inductance
(6.30)	$L_e = \frac{n_s^2 \mu_o \tau_c}{8} \ln \left( \frac{\tau_c^2 \pi}{4A_s} \right)$	End turn inductance
(6.31)	$L_{ph} = N_{sp}(L_g + L_s + L_e)$	Phase inductance
(6.35)	$V_{st} = [\pi(R_{so}^2 - R_{si}^2) - N_s A_s] L k_{st}$	Stator steel volume
(6.32)	$P_r = N_{ph} I_{ph}^2 R_{ph}$	Ohmic power loss
(6.34)	$P_{cl} = \rho_{bi} V_{st} \Gamma(B_{\max}, f_e)$	Core loss
(6.36)	$\eta = \frac{T \omega_m}{T \omega_m + P_r + P_{cl} + P_s} \cdot 100\%$	Efficiency
(6.33)	$q_s = \frac{P_r}{L(2d_3 + w_{sb})N_s}$	Slot heat density
(6.37)	$q_{st} = \frac{P_r + P_{cl}}{2\pi R_{so} L}$	Stator heat density

because they are assumed to be insignificant as before. Figure 6.6b is obtained by swapping the right magnet model with the lower air gap and magnet leakage reluctances, by combining the two magnet sections, and by expressing all reluctances by equivalent permeances. Finally, combining the magnet and magnet leakage permeances gives Fig. 6.6c, where the effective magnet permeance is  $\tilde{P}_m = P_m + 2P_{ml}$ .

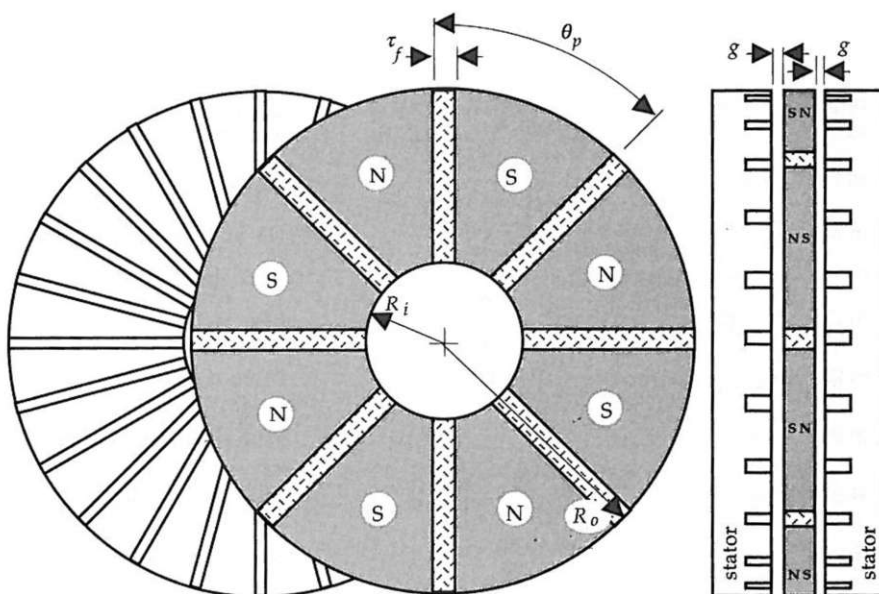


Figure 6.3 Dual axial flux motor topology showing geometrical definitions.

By flux division, the air gap flux is related to the magnet flux by  $\tilde{P}_m$

$$\begin{aligned}\phi_g/2 &= \frac{P_g/8}{P_g/8 + \tilde{P}_m/4} \phi_r/2 \\ \phi_g &= \frac{1}{1 + 2\tilde{P}_m/P_g} \phi_r\end{aligned}\quad (6.38)$$

This equation is identical to that for the single air gap case (4.2) with proper permeance interpretation. In particular,  $P_g/2$  appears in (6.38)

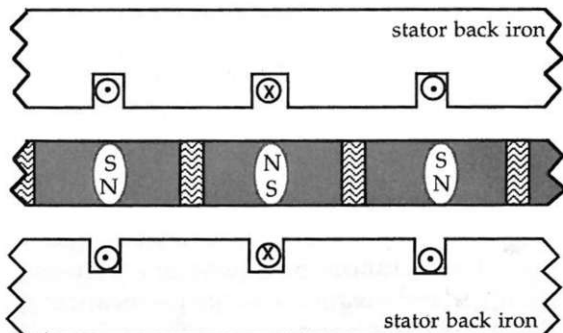
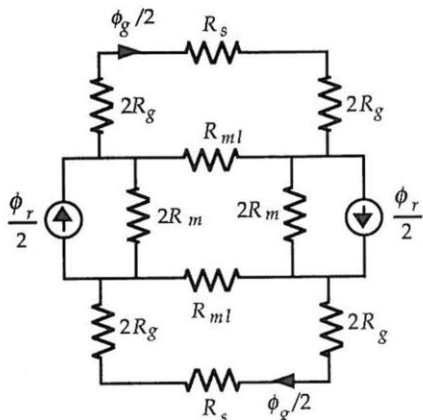


Figure 6.4 Dual air gap construction.



**Figure 6.5** Magnetic circuit model for dual air gap construction.

because the net air gap permeance in the dual air gap case is one-half that of the single air gap case, i.e., the total air gap length is double for the dual air gap case.

Given knowledge of the magnet, magnet leakage, and air gap permeances, further simplification of (6.38) is possible. These permeances can be determined with the help of Fig. 6.3. From the figure, the magnet permeance is

$$P_m = \frac{\mu_R \mu_o A_m}{l_m} \quad (6.39)$$

where the magnet cross-sectional area is

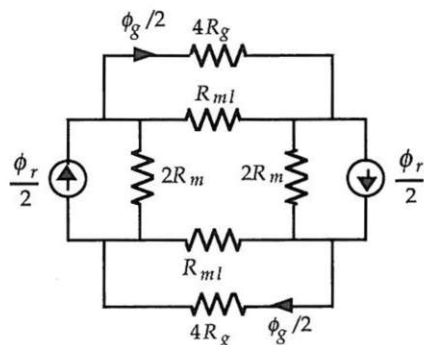
$$A_m = \frac{\pi}{N_m} (R_o^2 - R_i^2) - \tau_f (R_o - R_i) = \alpha_m \frac{\pi}{N_m} (R_o^2 - R_i^2) \quad (6.40)$$

where  $\alpha_m$  is the magnet fraction for this topology,

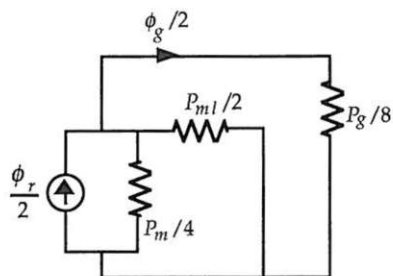
$$\alpha_m = 1 - \frac{N_m \tau_f}{\pi (R_o - R_i)} \quad (6.41)$$

The magnet leakage permeance is given by the same expression determined in Chap. 4, (4.4), with appropriate parameter changes for this topology,

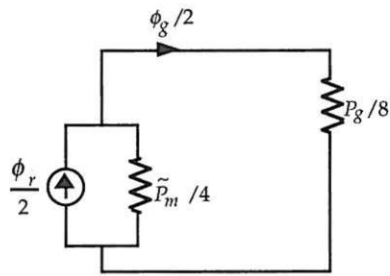
$$P_{ml} = \frac{\mu_o (R_o - R_i)}{\pi} \ln \left( 1 + \pi \frac{g}{\tau_f} \right) \quad (6.42)$$



(a)



(b)



(c)

Figure 6.6 Simplifications of the magnetic circuit in Fig. 6.5.

Combining (6.39), (6.40), and (6.42) gives the effective magnet permeance of

$$\tilde{P}_m = P_m + 2P_{ml} = k_{ml}P_m \quad (6.43)$$

where the magnet leakage factor  $k_{ml}$  is

$$k_{ml} = 1 + 2 \frac{P_{ml}}{P_m} = 1 + \frac{2l_m N_m}{\pi^2 \mu_R \alpha_m (R_i + R_o)} \ln \left( 1 + \pi \frac{g}{\tau_f} \right) \quad (6.44)$$

As in Chap. 4, the air gap permeance must be approximated since the magnet flux crossing the air gap travels through an increasing cross-sectional area. Using the average of the areas, the air gap permeance is

$$P_g = \frac{\mu_o A_g}{g_e} \quad (6.45)$$

where  $g_e = k_c g$  is the effective air gap length as described in Chap. 4 by (4.9),  $k_c$  is some average Carter coefficient, and the air gap cross-sectional area is

$$A_g = \frac{\pi(1 + \alpha_m)}{2N_m} (R_o^2 - R_i^2) \quad (6.46)$$

Finally substituting (6.39), (6.40), (6.43), (6.44), and (6.45) into (6.38) gives an air gap flux of

$$\phi_g = \frac{1}{1 + \frac{4\mu_R \alpha_m k_{ml} k_c g}{(1 + \alpha_m) l_m}} \phi_r \quad (6.47)$$

Recognizing that the flux concentration factor is unchanged from (4.10),

$$C_\phi = \frac{A_m}{A_g} = \frac{2\alpha_m}{1 + \alpha_m} \quad (6.48)$$

and that the permeance coefficient is  $P_c = l_m/(2gC_\phi)$  since there are two air gaps in series, (6.47) can be rewritten as

$$\phi_g = \frac{1}{1 + \mu_R k_c k_{ml}/P_c} \phi_r \quad (6.49)$$

which is identical to (4.11) for the single air gap case. In terms of magnet and air gap flux densities, this expression becomes

$$B_g = \frac{C_\phi}{1 + \mu_R k_c k_{ml}/P_c} B_r \quad (6.50)$$

which is identical to (4.12).

Thus, with appropriate changes to reflect two air gaps and axial flux flow, the magnetic circuit solution has the same form for both the single air gap radial flux motor and the dual air gap axial flux motor.

### Fixed parameters

The parameters assumed fixed for dual axial flux motor design are shown in Table 6.3. As with Table 6.1, the parameters are grouped

**TABLE 6.3 Fixed Parameters for the Dual Axial Flux Topology**

Parameter	Description
$P_{hp}$ , or $T$	Power, hp, or rated torque, N · m
$S_r$	Rated speed, rpm
$E_{max}$	Maximum back emf, V
$J_{max}$	Maximum slot current density, A/m <sup>2</sup>
$N_{ph}$	Number of phases
$N_m$	Number of magnet poles
$N_{sp}$	Number of slots per phase, $N_{sp} \geq N_m$
$g$	Air gap length, m
$l_m$	Magnet length, m
$R_o$	Outside radius, m
$R_i$	Inside radius, m
$k_{st}$	Lamination stacking factor
$\Gamma(B, f)$	Steel core loss density vs. flux density and frequency
$k_{st}, \rho_{bi}$	Lamination stacking factor and steel mass density
$\rho, \beta$	Conductor resistivity and temperature coefficient
$k_{cp}$	Conductor packing factor
$\tau_f$	Magnet spacer width, m
$B_r$	Magnet remanence, T
$\mu_R$	Magnet recoil permeability
$B_{max}$	Maximum steel flux density, T
$w_s$	Slot opening, m
$\alpha_{sd}$	Shoe depth fraction $(d_1 + d_2)/w_s$
Winding approach	Lap or wave, single- or double-layer, or other

according to function. The axial motor length is not specified in this topology, since it does not directly affect the torque produced. As a result, the slot depth is not constrained but can be determined by specifying the conductor current density. Also, only two radii are specified since flux flow is in the axial direction.

### Geometric parameters

From the fixed parameters in Table 6.3 and the topology shown in Figs. 6.3 and 6.7, it is possible to derive several important geometric parameters. The magnet pole pitches at the inner and outer radii are

$$\begin{aligned}\tau_{pi} &= R_i \theta_p \\ \tau_{po} &= R_o \theta_p\end{aligned}\quad (6.51)$$

where  $\theta_p = 2\pi/N_m$  is the angular pole pitch and the associated coil pitches are

$$\begin{aligned}\tau_{ci} &= \alpha_{cp} \tau_{pi} \\ \tau_{co} &= \alpha_{cp} \tau_{po}\end{aligned}\quad (6.52)$$

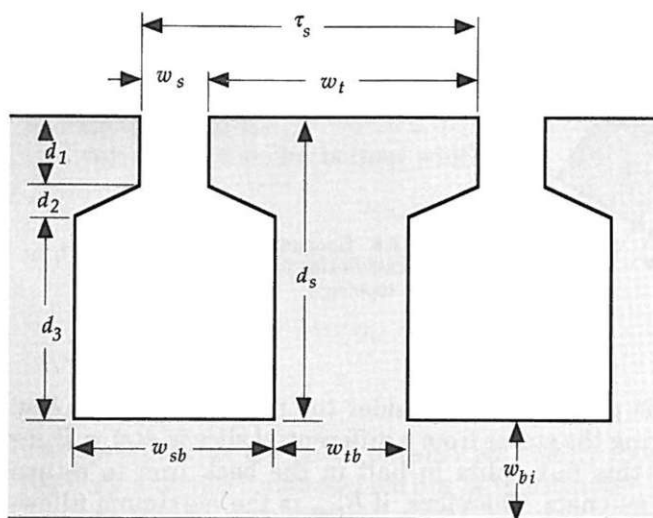


Figure 6.7 Slot geometry for the dual axial flux motor topology.

where the coil-pole fraction is given by (5.8). The slot pitches at the inner and outer radii are

$$\begin{aligned}\tau_{si} &= R_i \theta_s \\ \tau_{so} &= R_o \theta_s\end{aligned}\quad (6.53)$$

where  $\theta_s = 2\pi/N_s$  is the angular slot pitch. The slot cross-sectional area available for conductors is rectangular in this case and can be simply expressed as

$$A_s = w_{sb} d_3 \quad (6.54)$$

where  $w_{sb}$  is the slot bottom width.

The unknown parameters in this design are the slot dimensions. The width of the stator teeth varies with radius. After the tooth width at the slot bottom and back iron width are determined by the magnetic circuit solution, the slot depth can be determined by constraining the conductor current density to be exactly  $J_{\max}$ .

### Magnetic parameters

The magnetic parameters to be found are the stator back iron thickness and the stator tooth width. Since the magnet produces constant flux density over its surface, the total flux crossing the air gap increases linearly with radius due to increasing magnet width. Thus the amount of flux to be supported by the stator back iron increases with radius.

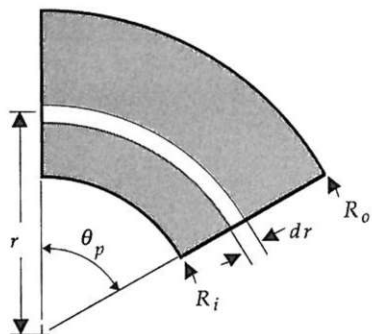


**Figure 6.8** Geometry for the torque calculation in the dual axial flux topology.

To understand this phenomenon, consider the magnet shown in Fig. 6.8. The flux entering the stator from a differential slice is  $\phi(r) = B_g \theta_p r dr$ . In the stator, this flux splits in half in the back iron to return through adjacent magnets. Therefore, if  $B_{\max}$  is the maximum allowable flux density in the back iron, the back iron flux is  $\phi_{bi}(r) = B_{\max} w_{bi} k_{st} dr$ , from which the required back iron thickness is

$$w_{bi}(r) = \frac{B_g \theta_p r}{2B_{\max} k_{st}} \quad (6.55)$$

It is not practical to build stators with a linearly increasing back iron width. Therefore, a constant back iron width equal to the maximum of (6.55) is chosen,

$$w_{bi} = \frac{B_g \tau_{po}}{2B_{\max} k_{st}} \quad (6.56)$$

Using the same argument made earlier in (6.16) the required tooth bottom width is

$$w_{tb}(r) = \frac{2}{N_{sm}} w_{bi}(r)$$

which is

$$w_{tbi} = \frac{B_g \tau_{pi}}{N_{sm} B_{\max} k_{st}} \quad (6.57)$$

at the inner radius. Since the slot width is constant, the tooth bottom width increases linearly with radius. This agrees with the topology shown in Fig. 6.3. Thus, even though the tooth width is smaller at the inner radius, the flux density in the stator teeth is uniform with respect to radius. That is, the narrow teeth at the inner radius are not any

more saturated than the teeth at the outer radius. Moreover, since the stator back iron thickness is wider than necessary at the inner radius, the net steel reluctance at the inner radius is much lower than that at the outer radius.

Given (6.57), the slot bottom width is

$$w_{sb} = \tau_{si} - w_{tbi} \quad (6.58)$$

and the slot aspect ratio at the inner radius is

$$\alpha_{si} = \frac{w_{sb}}{w_{tbi} + w_{sb}} \quad (6.59)$$

### Electrical parameters

The derivation of electrical parameters closely follows the radial flux topology analysis conducted earlier in this chapter. Therefore, the derivations for this topology will not be justified as thoroughly.

**Torque.** The torque produced by the axial flux topology requires some development because the torque is produced at a continuum of radii from  $R_i$  to  $R_o$ . Rather than develop the torque expression from the basic configuration considered in Chap. 4, it is convenient to start with the torque expression developed for the radial flux topology (6.18)

$$T = N_m k_d k_p k_s B_g L R_{ro} N_{spp} n_s i$$

where  $L$  is the conductor length exposed to the air gap flux density  $B_g$  and  $R_{ro}$  is the radius at which torque is produced. Based on this equation, and the geometry shown in Fig. 6.8, the incremental torque produced at a radius  $r$  by the interaction of  $B_g$  and a conductor of length  $dr$  is

$$T(r) = 2N_m k_d k_p k_s B_g N_{spp} n_s i r dr \quad (6.60)$$

where the factor of 2 appears because there are conductors on two stators producing torque at the radius  $r$ . Integration of this incremental torque gives a total developed torque of

$$T = 2N_m k_d k_p k_s B_g N_{spp} n_s i \int_{R_i}^{R_o} r dr = N_m k_d k_p k_s B_g N_{spp} n_s i (R_o^2 - R_i^2) \quad (6.61)$$

**Back emf.** Using (6.61) and following what was done earlier in (6.19), the peak back emf at rated speed is

$$e_{\max} = \frac{T \omega_m}{i} = N_m k_d k_p k_s B_g N_{spp} n_s (R_o^2 - R_i^2) \omega_m \quad (6.62)$$

from which the number of turns per slot required to produce  $E_{\max}$  is

$$n_s = \text{int} \left[ \frac{E_{\max}}{N_m k_d k_p k_s B_g N_{spp} (R_o^2 - R_i^2) \omega_m} \right] \quad (6.63)$$

where as before  $\text{int}(\cdot)$  returns the integer part of its argument because the number of turns must be an integer. Due to the truncation involved in (6.62), the peak back emf may be slightly less than  $E_{\max}$ . The actual peak back emf achieved can be found by substituting the value computed in (6.63) back into (6.62).

**Current.** Following the analysis conducted for the radial flux topology, the required total slot current, phase current, and conductor current densities are

$$I_s = \frac{T}{N_m k_d k_p k_s B_g N_{spp} (R_o^2 - R_i^2)} \quad (6.64)$$

$$I_{ph} = \frac{I_s}{N_{ph} n_s} \quad (6.65)$$

and

$$J_c = \frac{I_s}{k_{cp} A_s} \quad (6.66)$$

respectively. Given the specified maximum conductor current density  $J_{\max}$  and the slot cross-sectional area (6.54), the conductor slot depth required to support  $J_{\max}$  is

$$d_3 = \frac{I_s}{k_{cp} w_{sb} J_{\max}} \quad (6.67)$$

From this value, the total stator axial length can be computed as

$$L = d_s + w_{bi} \quad (6.68)$$

where

$$d_s = d_1 + d_2 + d_3 \quad (6.69)$$

**Resistance.** As stated earlier, the windings on the two stators are assumed to be connected in series. Therefore, factors of 2 are required since  $N_s$ ,  $N_{sm}$ ,  $N_{sp}$ ,  $N_{spp}$ , and  $n_{tpp}$  are defined per stator. The slot re-

sistance per slot is given by (4.28) with appropriate changes to reflect this topology,

$$R_s = \frac{\rho n_s^2 (R_o - R_i)}{k_{cp} A_s} \quad (6.70)$$

Since the end turn length is different at the inner and outer radii, the end turn resistance per slot is the average of that at the two radii,

$$R_e = \frac{\rho n_s^2 \pi (\tau_{co} + \tau_{ci})}{4 k_{cp} A_s} \quad (6.71)$$

Given two stators each having  $N_{sp}$  slots per phase, the phase resistance is

$$R_{ph} = 2N_{sp}(R_s + R_e) \quad (6.72)$$

**Inductance.** Calculation of the phase inductance requires slightly more work than the resistance because the air gap inductance is influenced by the two stators and two air gaps. As opposed to the single air gap case considered in Fig. 4.17, there are two air gap reluctances in series and the effective number of turns creating the air gap flux is equal to  $2n_s$ . Furthermore, the coil cross-sectional area is not rectangular but rather is  $A_c = \theta_c(R_o^2 - R_i^2)/2$ , where  $\theta_c = \alpha_{cp}\theta_p$  is the angular coil pitch in mechanical radians. Applying this information to (4.16) and dividing by 4 to express the air gap inductance on a per slot per stator basis gives

$$L_g = \frac{(2n_s)^2 \mu_R \mu_o A_c k_d}{8(l_m + 2\mu_R k_c g)} = \frac{n_s^2 \mu_R \mu_o \theta_c (R_o^2 - R_i^2) k_d}{4(l_m + 2\mu_R k_c g)} \quad (6.73)$$

The slot leakage inductance per slot is given by (6.29) with the slot length  $L$  replaced by  $R_o - R_i$ ,

$$L_s = n_s^2 \left[ \frac{\mu_o d_3}{3w_{sb}} + \frac{\mu_o d_2}{(w_s + w_{sb})/2} + \frac{\mu_o d_1}{w_s} \right] (R_o - R_i) \quad (6.74)$$

and the approximate end turn inductance per slot is given by the sum of one-half of (4.22) for the inner and outer end turns,

$$L_e = \frac{n_s^2 \mu_o \tau_{co}}{16} \ln \left( \frac{\tau_{co}^2 \pi}{4A_s} \right) + \frac{n_s^2 \mu_o \tau_{ci}}{16} \ln \left( \frac{\tau_{ci}^2 \pi}{4A_s} \right) \quad (6.75)$$

As earlier with the phase resistance, the total phase inductance is the sum of that due to all slots,

$$L_{ph} = 2N_{sp}(L_g + L_s + L_e) \quad (6.76)$$

### Performance

The performance of this topology follows that of the radial flux topology. The  $I^2R$  loss is given by (6.32) and the core loss is given by (6.34) where the approximate stator volume is

$$V_{st} = 2k_{st}[\pi(R_o^2 - R_i^2)(w_{bi} + d_s) - N_s A_s(R_o - R_i)] \quad (6.77)$$

Combining this information allows one to estimate the efficiency as (6.36). In a manner similar to that calculated for the radial flux topology, the heat density leaving the slot conductors and the maximum heat density appearing at the stator periphery are

$$q_s = \frac{P_r}{(R_o - R_i)(2d_3 + w_{sb})N_s} \quad (6.78)$$

$$q_{st} = \frac{P_r + P_{cl}}{2\pi(R_o^2 - R_i^2)} \quad (6.79)$$

### Design procedure

The design procedure for the dual axial flux topology follows the evaluation of the equations given in Table 6.4.

### Summary

In the above sections, design equations for the dual axial flux topology were developed. A key difference between this topology and the radial flux topology is the fact that torque is produced over a continuum of radii. In practice, the dual axial flux topology is not that popular for several reasons. First, it is ignored many times because the tooling and manufacturing processes needed for its construction are not readily available. Second, it offers superior performance only in those applications where the allowable radial dimension is sufficiently large.

### Conclusion

This concludes the development of design equations for the conventional radial and dual axial topologies. The equations presented here represent just one of many different approaches to the motor design

**TABLE 6.4 Design Equations for the Dual Axial Flux Topology**

No.	Expression	Description
(1.4)	$\omega_m = (\pi/30)S_r$	Mechanical speed, rad/s
(1.3)	$\omega_e = (N_m/2)\omega_m$	Electrical speed, rad/s
(n.a.)	$f_e = \omega_e/(2\pi)$	Fundamental electrical frequency, Hz
(6.17)	$T = 746P_{hp}/\omega_m$	Torque from horsepower
(5.2)	$N_s = N_{sp}N_{ph}$	No. of slots
(5.3)	$N_{spp} = N_{sp}/N_m$	No. of slots per pole per phase
(5.5)	$N_{sm} = N_{spp}N_{ph}$	No. of slots per pole
(5.8)	$\alpha_{cp} = \text{int}(N_{spp})/N_{spp}$	Coil-pole fraction
(6.3)	$\theta_p = 2\pi/N_m$	Angular pole pitch
(6.6)	$\theta_s = 2\pi/N_s$	Angular slot pitch
(5.7)	$\theta_{se} = \pi/N_{sm}$	Slot pitch, electrical radians
(6.51)	$\tau_{pi} = R_i\theta_p$	Inside pole pitch
(6.51)	$\tau_{po} = R_o\theta_p$	Outside pole pitch
(6.52)	$\tau_{ci} = \alpha_{cp}\tau_{pi}$	Inside coil pitch
(6.52)	$\tau_{co} = \alpha_{cp}\tau_{po}$	Outside coil pitch
(6.53)	$\tau_{si} = R_i\theta_s$	Inside slot pitch
(5.6)	$k_d = \frac{\sin(N_{spp}\theta_{se}/2)}{N_{spp}\sin(\theta_{se}/2)}$	Distribution factor
(5.9)	$k_p = \alpha_{cp}$	Pitch factor
(5.13)	$k_s = 1 - \theta_{se}/(2\pi)$	Skew factor
(6.41)	$\alpha_m = 1 - \frac{N_m\tau_f}{\pi(R_o - R_i)}$	Magnet fraction
(4.11)	$C_\phi = \frac{2\alpha_m}{1 + \alpha_m}$	Flux concentration factor
(2.27)	$P_c = l_m/(2gC_\phi)$	Permeance coefficient
(6.43)	$k_{ml} = 1 + \frac{2l_mN_m}{\pi^2\mu_R\alpha_m(R_i + R_o)} \ln \left( 1 + \pi \frac{g}{\tau_f} \right)$	Magnet leakage factor
(n.a.)	$g_c = 2g + l_m/\mu_R$	Effective air gap for Carter coefficient
(2.12)	$k_c = \left[ 1 - \frac{1}{\frac{\tau_{si}}{w_s} \left( 5 \frac{g_c}{w_s} + 1 \right)} \right]^{-1}$	Carter coefficient
(6.46)	$A_g = \frac{\pi(1 + \alpha_m)}{2N_m} (R_o^2 - R_i^2)$	Air gap area
(4.13)	$B_g = \frac{C_\phi}{1 + \mu_R k_c k_{ml}/P_c} B_r$	Air gap flux density
(2.3)	$\phi_g = B_g A_g$	Air gap flux
(6.56)	$w_{bi} = \frac{B_g \tau_{po}}{2B_{\max} k_{st}}$	Back iron width
(6.57)	$w_{tbi} = \frac{B_g \tau_{pi}}{N_{sm} B_{\max} k_{st}}$	Tooth width at inner radius
(6.58)	$w_{sb} = \tau_{si} - w_{tbi}$	Slot bottom width
(6.59)	$\alpha_{si} = \frac{w_{sb}}{w_{tbi} + w_{sb}}$	Slot aspect ratio at inner radius

**TABLE 6.4 Design Equations for the Dual Axial Flux Topology (Continued)**

No.	Expression	Description
(6.9)	$d_1 + d_2 = \alpha_{sd} w_{tbi}$	Shoe depth, split between $d_1$ and $d_2$
(6.63)	$n_s = \text{int}\left(\frac{E_{\max}}{N_m k_d k_p k_s B_g N_{spp} (R_o^2 - R_i^2) \omega_m}\right)$	No. of turns per slot
(6.62)	$e_{\max} = N_m k_d k_p k_s B_g N_{spp} n_s (R_o^2 - R_i^2) \omega_m$	Peak back emf
(6.64)	$I_s = \frac{T}{N_m k_d k_p k_s B_g N_{spp} (R_o^2 - R_i^2)}$	Peak slot current
(6.65)	$I_{ph} = \frac{I_s}{N_{ph} n_s}$	Phase current
(6.67)	$d_3 = \frac{I_s}{k_{cp} w_{sb} J_{\max}}$	Conductor slot depth
(6.54)	$A_s = w_{sb} d_3$	Conductor area
(6.66)	$J_c = \frac{I_s}{k_{cp} A_s}$	Peak conductor current density
(6.69)	$d_s = d_1 + d_2 + d_3$	Total slot depth
(6.68)	$L = d_s + w_{bi}$	Stator axial length
(4.37)	$ B_s _{\max} = \frac{\mu_o I_s}{w_s}$	Peak slot flux density
(6.70)	$R_s = \frac{\rho n_s^2 (R_o - R_i)}{k_{cp} A_s}$	Slot resistance
(6.71)	$R_e = \frac{\rho n_s^2 \pi (\tau_{co} + \tau_{ci})}{4 k_{cp} A_s}$	End turn resistance
(6.72)	$R_{ph} = 2 N_{sp} (R_s + R_e)$	Phase resistance
(6.73)	$L_g = \frac{n_s^2 \mu_R \mu_o \theta_c (R_o^2 - R_i^2) k_d}{4 (l_m + 2 \mu_R k_c g)}$	Air gap inductance
(6.74)	$L_s = n_s^2 \left[ \frac{\mu_o d_3}{3 w_{sb}} + \frac{\mu_o d_2}{(w_s + w_{sb})/2} + \frac{\mu_o d_1}{w_s} \right] (R_o - R_i)$	Slot leakage inductance
(6.75)	$L_e = \frac{n_s^2 \mu_o \tau_{co}}{16} \ln \left( \frac{\tau_{co} \pi}{4 A_s} \right) + \frac{n_s^2 \mu_o \tau_{ci}}{16} \ln \left( \frac{\tau_{ci} \pi}{4 A_s} \right)$	End turn inductance
(6.76)	$L_{ph} = 2 N_{sp} (L_g + L_s + L_e)$	Phase inductance
(6.77)	$V_{st} = 2 k_{st} [\pi (R_o^2 - R_i^2) (w_{bi} + d_s) - N_s A_s (R_o - R_i)]$	Stator steel volume
(6.32)	$P_r = N_{ph} I_{ph}^2 R_{ph}$	Ohmic power loss
(6.34)	$P_{cl} = \rho_{bi} V_{st} \Gamma(B_{\max}, f_e)$	Core loss
(6.36)	$\eta = \frac{T \omega_m}{T \omega_m + P_r + P_{cl} + P_s} \cdot 100\%$	Efficiency
(6.78)	$q_s = \frac{P_r}{(R_o - R_i)(2d_3 + w_{sb})N_s}$	Slot heat density
(6.79)	$q_{st} = \frac{P_r + P_{cl}}{2 \pi (R_o^2 - R_i^2)}$	Stator heat density

problem. The approach followed here may not be the best approach. However, it offers a good starting point for those interested in developing their own motor design capabilities and does illustrate many of the design tradeoffs inherent in motor design. There is no end to the exceptions and variations that could be considered. Many companies have computer-based design programs that have been modified and improved regularly for decades. To compete with these programs, the analysis conducted in this chapter would have to include libraries of material characteristics, wire gage selection, motor drive selection and characterization, and at least a one-dimensional, steady-state thermal characterization.

## Motor Drive Schemes

The preceding material presented in this text is not complete without an understanding of how brushless PM motors are electrically driven to produce rotational motion. Since motor torque is the input to a mechanical system or load, it is desirable to have fine control over torque production. In the common situation where smooth mechanical motion is desired, constant ripple-free torque must be produced. Based on the material presented so far, constant torque is difficult to produce for several reasons. First, periodically varying cogging torque usually exists which is independent of any applied motor excitation. Second, the desired mutual torque is not even unidirectional unless the phase current changes sign whenever the back emf does. Furthermore, constant mutual torque is produced only when the product of the back emf and applied current is constant with respect to position. While elaborate and expensive drive schemes are possible, in many applications simplifying assumptions are made that lead to readily implemented drive schemes that perform reasonably well. In this chapter, these simple drive schemes will be illustrated for two- and three-phase motors. The fundamental task for a motor drive is to apply current to the correct windings, in the correct direction, at the correct time. This process is called *commutation*, since it describes the task performed by the commutator (and brushes) in a conventional brush dc motor. As before, the goal is to develop an intuitive understanding rather than discuss every nuance of every possible motor drive scheme. More detailed information can be found in references such as Leonhard (1985), and Murphy and Turnbull (1988). With this intuitive understanding, more complex drive schemes are readily understood.

### Two-Phase Motors

Until now, torque and back emf expressions have been developed considering just one motor phase. When there is more than one phase,

each individual phase acts independently to produce torque. Following the ideas that lead to the torque-back emf-current relationship (3.28), consider the two-phase motor illustrated in Fig. 7.1. Power dissipated in the phase resistances produces heat, the phase inductances store energy but dissipate no power, and power absorbed by the back emf sources  $E_A$  and  $E_B$  is converted to mechanical power  $T\omega$  (think about it: where else could it go?). Writing this last relationship mathematically gives

$$E_A i_A + E_B i_B = T\omega \quad (7.1)$$

Here the back emf sources are determined by the motor design and the currents are determined by the motor drive. Because of the  $BLv$  law (3.12), the back emf sources are linear functions of speed, i.e.,  $E = k\omega$ , where  $k$ , the back emf waveshape, is a function of motor parameters and position. Substituting this relationship into (7.1) gives

$$k_A i_A + k_B i_B = T \quad (7.2)$$

Thus the mutual torque produced is a function of the back emf waveshapes and the applied currents. Most importantly, (7.2) applies instantaneously. Any instantaneous variation in the back emf waveshapes or the phase currents will produce an instantaneous torque variation.

Equation (7.2) provides all the information necessary to design drive schemes for the two-phase motor. Since the back emf waveshapes are a function of position, it is convenient to consider (7.2) graphically. Making the simplifying assumption that the back emf is an ideal

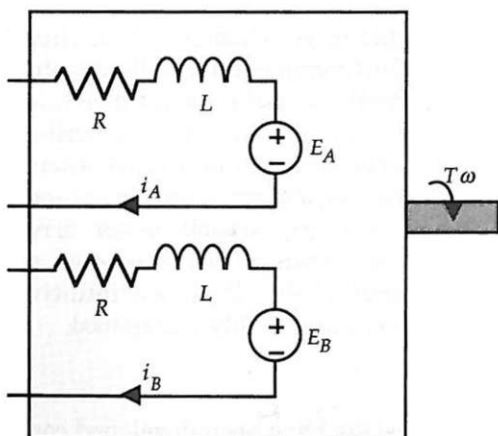
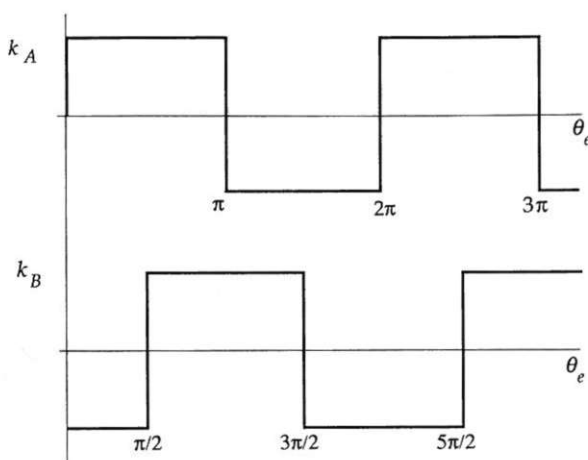


Figure 7.1 A two-phase motor.



**Figure 7.2** Square wave back emf shapes for a two-phase motor.

square wave, Fig. 7.2 shows the back emf waveshapes, with that from phase *B* delayed by  $\pi/2$  electrical radians with respect to phase *A*.

### One-phase-ON operation

Given the waveshapes shown in Fig. 7.2, several drive schemes become apparent. The first, shown in Fig. 7.3, is one-phase-ON operation where only one phase is conducting current at any one time. In this figure, the phase currents are superimposed over the back emf waveshapes and (7.2) is applied instantaneously to show the resulting motor torque on the lower axes. The overbar notation is used to signify current flowing in the reverse direction. Some important aspects of this drive scheme include:

- Ideally, constant ripple-free torque is produced.
- The shape of the back emf of the phase not conducting at any given time, e.g., phase *A* over  $3\pi/4 \leq \theta \leq 5\pi/4$ , has no influence on torque production since the associated current is zero. Thus the shape of the back emf need only be flat when the current is applied. The smoothing of the transitions in the back emf that exist in a real motor do not add torque ripple.
- Neither phase is required to produce torque in regions where its associated back emf is changing sign.
- Each phase contributes an equal amount to the total torque produced. Thus each phase experiences equal losses and the drive electronics are identical for each phase.

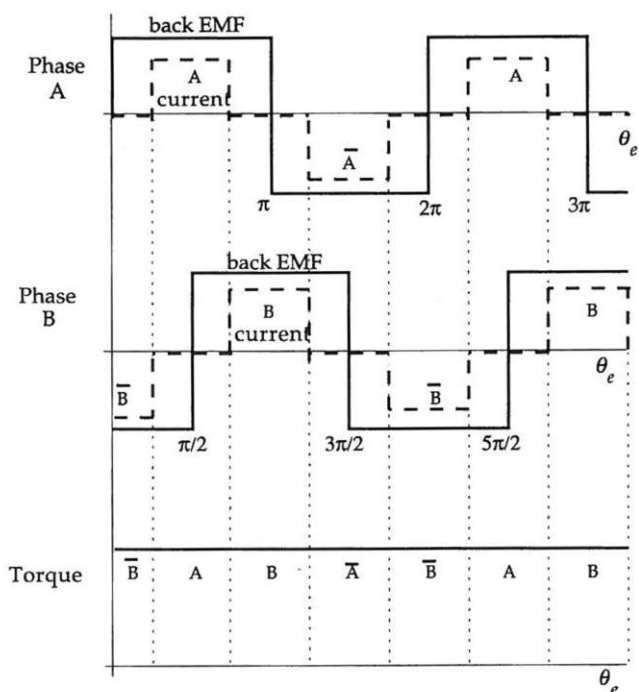


**Figure 7.3** One-phase-ON torque production.

- Copper utilization is said to be 50 percent, since at any time only one-half of the windings are being used to produce torque; the other half have no current flowing in them.
- The amount of torque produced can be varied by changing the amplitude of the current pulses.
- Square pulses of current are required but not achievable in the real world, since the inductive phase windings limit the current slope to  $di/dt = v/L$ , where  $v$  is the applied voltage and  $L$  is the inductance. Using  $\theta = \omega t$ , this relationship can be stated in terms of position as  $di/d\theta = v/(\omega L)$ . With either interpretation, the rate of change in current is finite, whereas Fig. 7.3 assumes that it is periodically infinite.

### Two-phase-ON operation

Following the same procedure used to construct Fig. 7.3, Fig. 7.4 shows two-phase-ON operation, where both phases are conducting at all

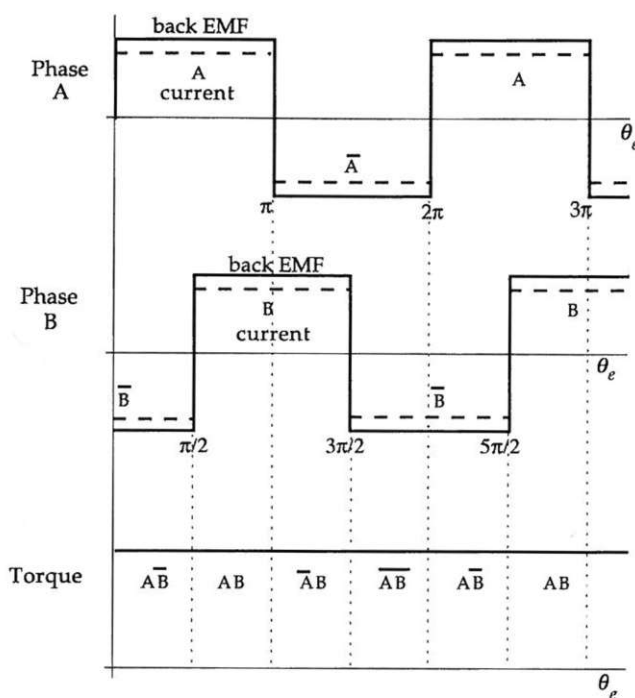


Figure 7.4 Two-phase-ON torque production.

times. The phase current values given in (6.22) and (6.65) assume this drive scheme. Important aspects of this drive scheme include:

- Ideally, constant ripple-free torque is produced.
- The shape of the back emf is critical at all times, since torque is produced in each phase at all times.
- If either current does not change sign at exactly the same point that the back emf does, negative phase torque is produced, which leads to torque ripple.
- Both phases are required to produce torque in regions where their associated back emf's are changing sign.
- Each phase contributes an equal amount to the total torque produced. Thus each phase experiences equal losses and the drive electronics are identical for each phase.
- Copper utilization is 100 percent.
- The amount of torque produced can be varied by changing the amplitude of the square wave currents.

- Impossible to produce square wave currents are required.
- For a constant torque output, the peak phase current is reduced by one-half compared with the one-phase-ON scheme.

### The sine wave motor

A square wave back emf motor driven by square current pulses in either one- or two-phase-ON operation as described above represents what is usually called a brushless dc motor. On the other hand, if the back emf is sinusoidal, the motor is commonly called a synchronous motor. Operation of this motor follows (7.2) also. However, in this case it is easier to illustrate torque production analytically. The key to understanding the two-phase synchronous motor is by recalling the trigonometric identity  $\sin^2\theta + \cos^2\theta = 1$ .

Let phase A have a back emf shape of  $k_A = K \cos \theta$ , and be driven by a current  $i_A = I \cos \theta$ . If as before the back emf of phase B is delayed by  $\pi/2$  electrical radians from phase A,  $k_B = K \sin \theta$ , and the associated phase current is  $i_B = I \sin \theta$ . Applying these expressions to (7.2) gives

$$\begin{aligned} k_A i_A + k_B i_B &= T \\ KI(\cos^2\theta + \sin^2\theta) &= KI = T \end{aligned} \tag{7.3}$$

Thus once again the torque produced is constant and ripple-free. In addition, the currents are continuous and only finite  $di/d\theta$  is required to produce them. Just as in the square wave case considered earlier, the currents must be synchronized with the motor back emf. To summarize, important aspects of this drive scheme include:

- Ideally, constant ripple-free torque is produced.
- The shape of the back emf and drive currents must be sinusoidal.
- If both phase currents are out of phase an equal amount with their respective back emf's, the torque will have a reduced amplitude but will remain ripple-free.
- Each phase contributes an equal amount to the total torque produced. Thus each phase experiences equal losses and the drive electronics are identical for each phase.
- Copper utilization is 100 percent.
- The amount of torque produced can be varied by changing the amplitude of the sinusoidal currents.
- The phase currents have finite  $di/d\theta$ .

Based on the three examples considered above, it is clear that there are an infinite number of ways to produce constant ripple-free torque.

All that is required is that the left-hand side of (7.2) instantaneously sum to a constant. The trouble with the square wave back emf schemes is that infinite  $di/d\theta$  is required. The torque ripple that results from not being able to generate the required square pulses is called commutation torque ripple. The trouble with the sinusoidal back emf case is that pure sinusoidal currents must be generated. In all cases, the back emf and currents must be very precise whenever the current is nonzero; any deviation from ideal produces torque ripple. For the square wave back emf schemes position information is required only at the commutation points (i.e., four points per electrical period). On the other hand, for the sinusoidal back emf case much higher resolution is required if the phase currents are to closely follow the back emf waveshapes. Thus simple and inexpensive Hall effect sensors are sufficient for the brushless dc motor, whereas an absolute position sensor, e.g., an absolute encoder or resolver, is required in the sinusoidal current drive case.

Despite the fact that the square wave back emf schemes inevitably produce torque ripple, they are commonly implemented because they are simple and inexpensive. In many applications, the cost of higher performance cannot be justified.

### H-bridge circuitry

Based on Figs. 7.3 and 7.4 it is necessary to send positive and negative current pulses through each motor winding. The most common circuit topology used to accomplish this is the full bridge or H-bridge circuit as shown in Fig. 7.5. In the figure,  $V_{cc}$  is a dc supply, switches  $S_1$  through  $S_4$  are commonly implemented with MOSFETs or IGBTs (though some still use bipolar transistors because they're cheap), diodes  $D_1$  through  $D_4$ , called freewheeling diodes, protect the switches by providing a reverse current path for the inductive phase current, and  $R$ ,  $L$ , and  $E_b$  represent one motor phase winding.

Basic operation of the H bridge is fairly straightforward. As shown in Fig. 7.6a, if switches  $S_1$  and  $S_4$  are closed, current flows in the positive direction through the phase winding. On the other hand, when switches

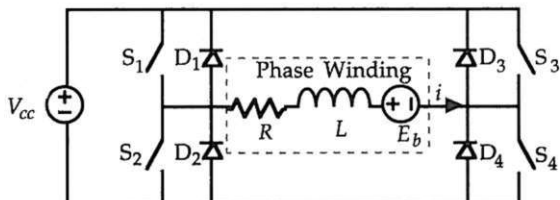
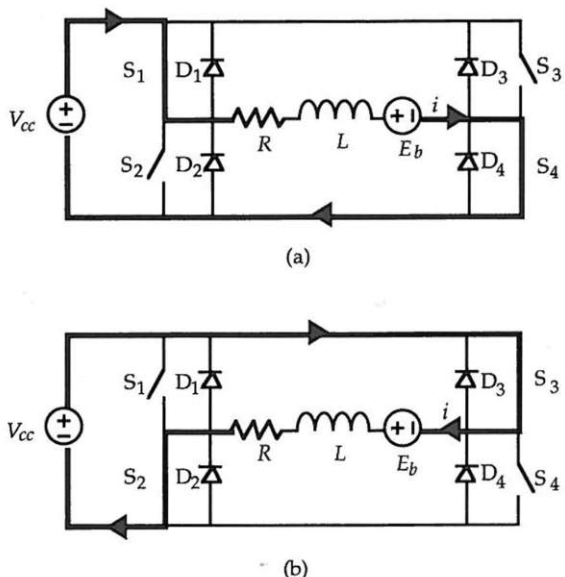


Figure 7.5 An H-bridge circuit.

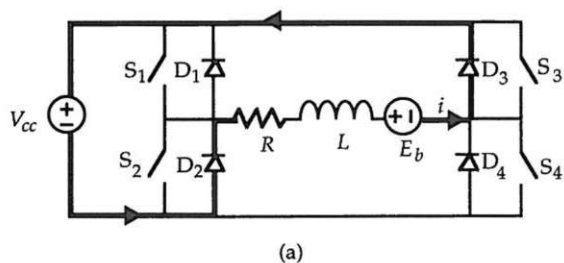


**Figure 7.6** (a) Positive current conduction and (b) negative current conduction in an H-bridge circuit.

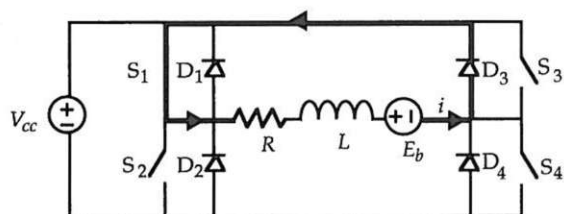
\$S\_2\$ and \$S\_3\$ are closed, current flows in the negative direction through the phase winding as shown in Fig. 7.6b. In either case, the current climbs exponentially according to the \$L/R\$ time constant and reaches the value of \$(\pm V\_{cc} - E\_b)/R\$ if the switches are left closed long enough.

**Turn-off behavior.** What takes more work to understand is the turn-off behavior of the H bridge and how phase current is controlled to limit its magnitude. Current control is accomplished by chopping, i.e., employing pulse-width-modulation (PWM) techniques. Because of its fundamental nature, PWM will be discussed at length later. For the time being, consider the turn-off behavior of the H bridge. This behavior is guided by the fundamental behavior of inductors. That is, that current cannot change instantaneously but must be continuous, and the larger the voltage across an inductor, the faster the current through it will change.

To start, let the phase current be a constant \$I\_m\$ with switches \$S\_1\$ and \$S\_4\$ closed as shown in Fig. 7.6a. Given these initial conditions, consider what happens when both switches are opened to bring the current back to zero. Now, since current no longer flows through \$S\_1\$ and \$S\_4\$, a negative voltage appears across the inductor because \$di/dt\$ is negative. At the same time, the phase current continues to flow in the same direction because it can't change instantaneously. The only path for current flow



(a)



(b)

**Figure 7.7** Current decay when (a) switches  $S_1$  and  $S_4$  open, (b) only switch  $S_4$  opens.

is through diodes  $D_2$  and  $D_3$  as shown in Fig. 7.7a. No current can flow through open switches or in the reverse direction through diodes  $D_1$  or  $D_4$ . During this time, the voltage across the phase inductance is

$$L \frac{di}{dt} = -Ri - V_{cc} - E_b \quad (7.4)$$

which is clearly large and negative when  $i > 0$ ,  $V_{cc} > 0$ , and  $E_b > 0$ . As time progresses, the current decreases exponentially toward the negative value  $-(V_{cc} + E_b)/R$ . Upon reaching zero current, the diodes turn OFF, the energy in the inductor ( $0.5Li^2$ ) is returned to the supply, and the circuit rests. If the circuit lacked freewheeling diodes, the inductor voltage would increase in amplitude until one or more switches are destroyed in an attempt to provide a current path for the inductor current.

In some situations, just one of the two switches is opened. To illustrate this action, assume the conditions shown in Fig. 7.6a and open only switch  $S_4$ ; let  $S_1$  remain closed. The path for decaying current flow in this case is through  $D_3$  and  $S_1$  as shown in Fig. 7.7b, giving an inductor voltage of

$$L \frac{di}{dt} = -Ri - E_b \quad (7.5)$$

which is much smaller in magnitude than that given in (7.4) because  $-V_{ce}$  is missing. Hence the inductor current decays much more slowly in this situation. Later this turn-off mode will prove helpful in implementing PWM current control.

**Switch current.** A major task in drive circuit design is to size the switches, that is, to determine their rms currents. In the H bridge, switches  $S_1$  and  $S_4$  carry the positive portion of the phase current, whereas switches  $S_2$  and  $S_3$  carry the negative portion of the phase current. Because of this division, the rms switch current is less than the rms phase current. As illustrated for the two-phase-ON scheme in Fig. 7.8, the rms value of the switch current is easily shown to be  $100/\sqrt{2} = 70.7$  percent of the rms phase current. Though not shown, the same ratio applies to the one-phase-ON scheme.

**Summary.** Important aspects of the H-bridge circuit include:

- Bidirectional current flow is easily achieved.
- Given that the back emf and current have the same sign in Figs. 7.3 and 7.4, the back emf acts to fight the increase in phase current amplitude during turn-on.
- In the one-phase-ON drive scheme in Fig. 7.3, the back emf and current have the same sign at the turn-off points. Thus, by (7.4), the

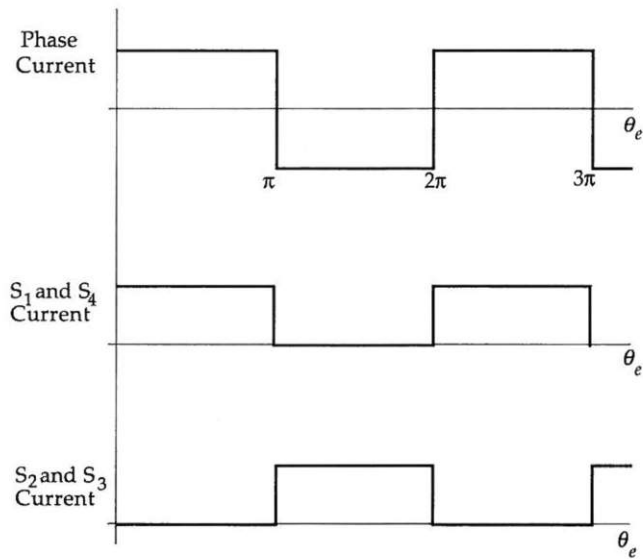


Figure 7.8 Phase and switch currents for two-phase-ON operation.

back emf acts to assist the decrease in phase current during turn-off.

- In the two-phase-ON drive scheme Fig. 7.4, the back emf and current have opposite signs immediately after the turn-off points. Thus the back emf acts to fight the decrease in phase current during turn-off. Thus the back emf hinders commutation at both turn-on and turn-off in the two-phase-ON drive scheme.
- At no time can vertical pairs of switches, i.e.,  $S_1$  and  $S_2$  or  $S_3$  and  $S_4$ , be closed simultaneously. If this happens, a *shoot-through fault* occurs where the motor supply is shorted. In implementation, a short delay is often added between commutations to guarantee no shoot-through condition occurs.
- For the square wave back emf schemes, the rms switch current is equal to 70.7 percent of the rms phase current.
- For two-phase motors, two H bridges are required, giving a total of eight switches to be implemented by power electronic devices.

### Three-Phase Motors

Three-phase motors overwhelmingly dominate all others. The exact reasons for this dominance are not known, but the historical dominance of three-phase induction and synchronous motors and the minimal number of power electronic devices required are likely contributing factors. The addition of a third phase provides an additional degree of freedom over the two-phase motor, which manifests itself in more drive schemes and terminology. For example, wye ( $\text{Y}$ ) and delta ( $\Delta$ ) connections are possible.

In three-phase motors, the power balance equation leads to

$$k_A i_A + k_B i_B + k_C i_C = T \quad (7.6)$$

where  $k_C$  and  $i_C$  are the back emf shape and current respectively, of the third phase. By construction, the back emf's of each phase have the same shape but are offset from each other by  $2\pi/3$  electrical radians, or 120 electrical degrees. The back emf shapes for the ideal square wave back emf motor are shown in Fig. 7.9.

### Three-phase-ON operation

The most obvious drive scheme for the three-phase motor is to extend the two-phase-ON operation of the two-phase motor as shown in Fig. 7.10. Here each phase conducts current at all times and contributes equally to the torque at all times. At each commutation point one phase

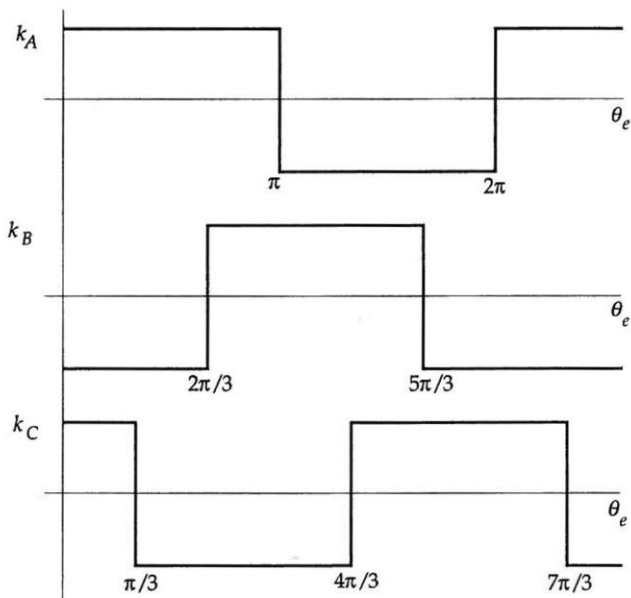


**Figure 7.9** Square wave back emf shapes for a three-phase motor.

current changes sign and the others remain unchanged. The phase current values given in (6.22) and (6.65) assume this drive scheme. The important aspects listed above for the two-phase-ON, two-phase motor apply here as well.

Despite the conceptual simplicity of this drive scheme, it is hardly ever implemented in practice because three H bridges as shown in Fig. 7.5 are required, one for each phase winding. The resulting 12 power electronic devices make the drive expensive compared with other drive schemes.

### Y connection

Just as the Y connection is a popular configuration in three-phase power systems, it is also the most common configuration in three-phase brushless PM motors. As shown in Fig. 7.11, the center or neutral of the Y is not brought out and each external terminal or line is connected to a half bridge circuit, and the collection of three half bridges is called a three-phase bridge. In this way, an H bridge appears between each set of terminals. Only six power electronic devices are needed for the switches in the three-phase bridge, as opposed to eight for a two-phase motor. The supply voltage is applied from line to line through the switches rather than from line to neutral. Compared with the three-phase-ON case, the supply voltage works against two back emf sources

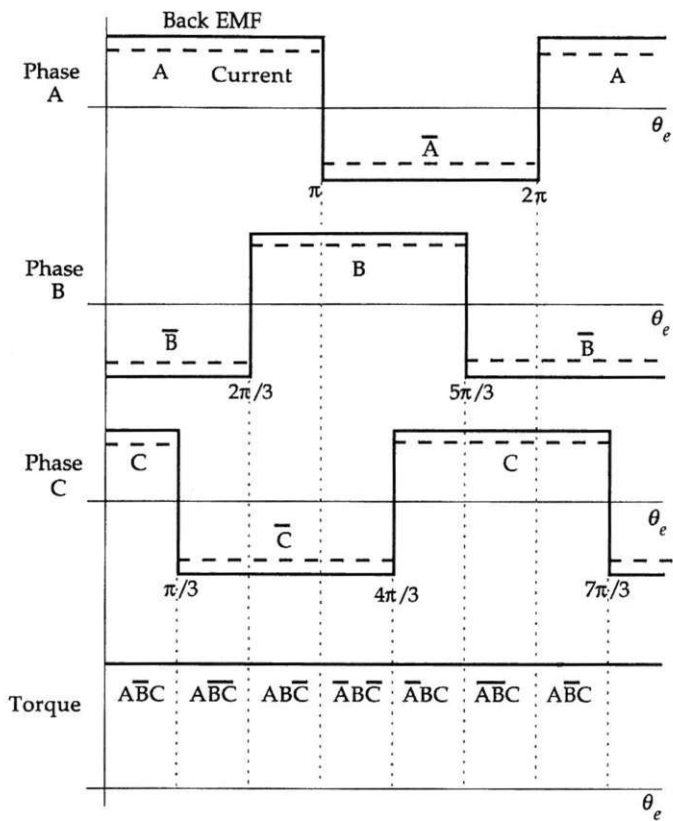


Figure 7.10 Three-phase-ON operation.

to force current into the motor. Furthermore, independent control of the phase currents is not possible since Kirchhoff's current law,  $I_A + I_B + I_C = 0$ , must be satisfied.

Torque production follows the idea that current should flow in only two of the three phases at a time, and that there should be no torque production near the back emf sign crossings. Figure 7.12 shows the phase currents superimposed on the back emf's. Each phase conducts current over the central  $2\pi/3$  electrical radians of each half cycle. The resulting torque is shown at the bottom of the figure with the letter designating the current polarities contributing to the torque. At each commutation point, one switch remains closed, one opens, another closes, and the rest remain open. There are six commutations per electrical period, and thus this drive scheme is often called a six-step drive (Murphy and Turnbull, 1988). The six numbered arrows shown in Fig. 7.11 illustrate these six steps, as do the respective circled step numbers in Fig. 7.12.

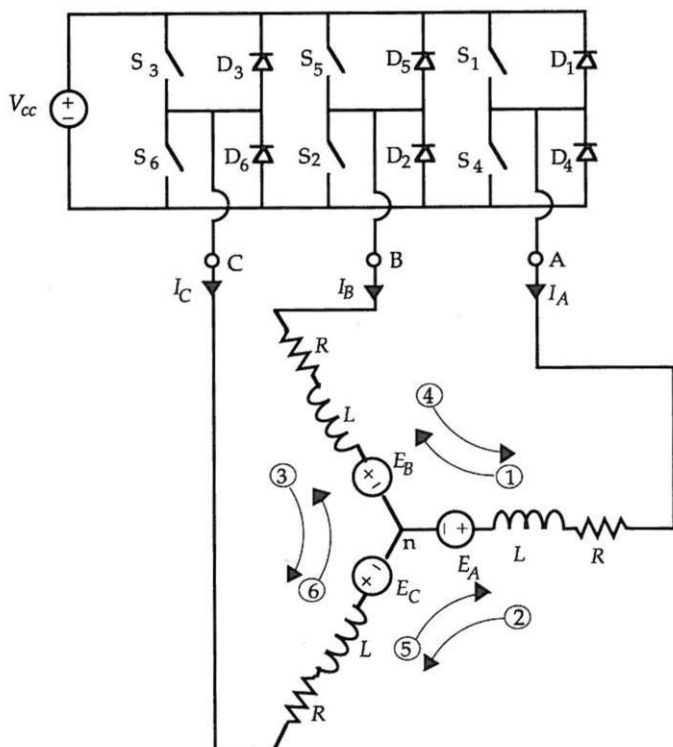


Figure 7.11 Y-connected three-phase motor and drive circuitry.

Because only two phases are conducting current and contributing to torque production at any one time, the amplitude of the current must be 50 percent larger here than in the three-phase-ON case above where all three phases contribute simultaneously. When two phases are called upon to produce the same torque that three phases do, the current in each phase must be  $3/2$  as large, since  $(3/2) \cdot (2 \text{ phases}) = (1) \cdot (3 \text{ phases})$ . As a result, if this drive scheme is implemented, Eqs. (6.22) and (6.65) must be modified to reflect the current waveforms shown in Fig. 7.12.

Equations (6.22) and (6.65) are the rms phase currents required to produce a specified rated torque. Based on the above, these currents must be increased in amplitude by a factor of  $3/2$ . Moreover, the equations must reflect the rms value of the phase currents, which is  $\sqrt{2/3} I_{\text{peak}}$  based on the waveforms shown in Fig. 7.12. Combining these factors, (6.22) and (6.65) become

$$I_{ph} = \frac{3}{2} \sqrt{\frac{2}{3}} \frac{I_s}{3n_s} = \sqrt{\frac{3}{2}} \frac{I_s}{3n_s} \quad (7.7)$$

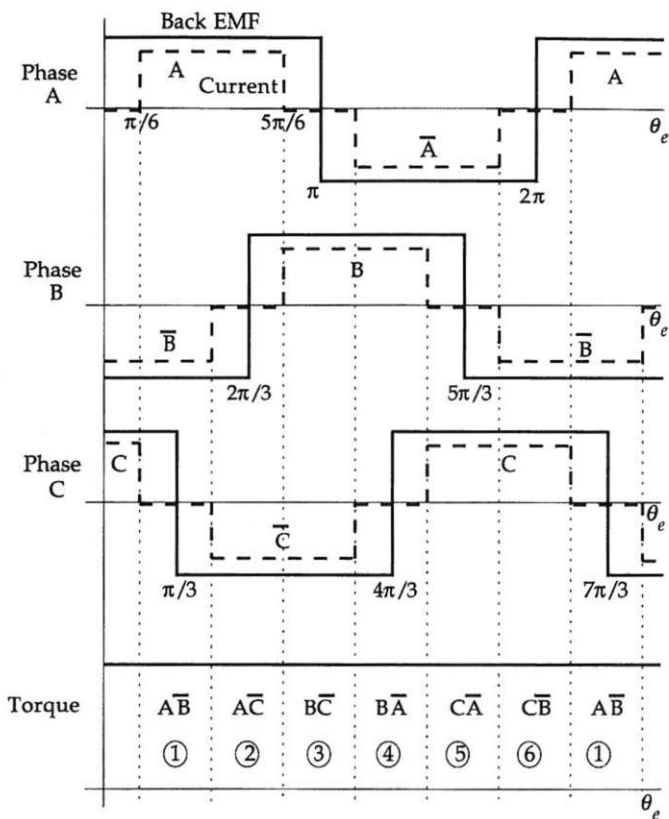


Figure 7.12 Torque production in a Y-connected three-phase motor.

for the six-step driven three-phase motor. Compared with the three-phase-ON case, the rms phase current is approximately 22 percent larger and the ohmic motor loss is 50 percent greater. Thus, while the Y connection minimizes the number of power electronic devices used, it does not minimize losses.

To summarize, important aspects of this drive scheme include:

- Ideally, constant ripple-free torque is produced.
- Only six switches are required, which is a minimum number.
- Phases are not required to produce torque in regions where their associated back emf is changing sign. Thus the back emf can be more trapezoidal than square.
- Each phase contributes an equal amount to the total torque produced. Thus each phase experiences equal losses and the drive electronics are identical for each phase.

- Copper utilization is 67 percent, since at any one time only two of the three phases are conducting current.
- For the same output, ohmic motor losses are 50 percent greater than those in the three-phase-ON drive scheme.
- The amount of torque produced can be varied by changing the amplitude of the square wave currents.
- Impossible to produce  $120^\circ$  wide square wave currents are required. The inherent finite rise and fall time of the current creates torque ripple, commonly called commutation torque ripple.
- Independent control of phase currents is not possible.
- From  $I_A + I_B + I_C = 0$ , it can be shown that the phase currents cannot have any harmonics that are multiples of three, i.e., triple-n or *tripplen* harmonics (Murphy and Turnball, 1988; Kassakian, Schlecht, and Verghese, 1991).
- Because phase windings appear in series, the supply voltage must be greater than the vector sum of the back emf's at rated speed.

### $\Delta$ connection

The  $\Delta$  connection shown in Fig. 7.13 is the dual of the Y connection. This connection is not that popular because it has a major weakness,

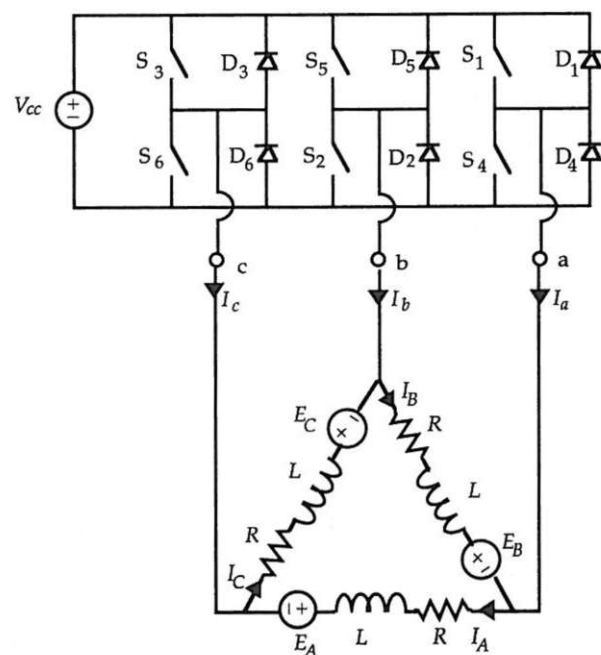


Figure 7.13  $\Delta$ -connected three-phase motor and drive circuitry.

that being the additional ohmic motor loss and torque ripple due to circulating currents flowing around the delta. Three-phase power system utility generators are never  $\Delta$ -connected for this reason. It is relatively easy to show that if the back emf waveforms of each phase do not have exactly the same shape or are not exactly  $120^\circ$  out of phase with one another or contain any triplen harmonics, circulating currents will flow around the delta. Because of this weakness,  $\Delta$ -connected motors appear only in lower-performance motors at low output power levels, e.g., in the fractional horsepower range, where their higher losses can be offset with lower material costs (Miller, 1989).

Based on the above, a motor having the ideal square wave back emf shape as shown in Fig. 7.9 cannot be connected in the  $\Delta$  connection because a square wave back emf motor has very high triplen harmonic content. Given the nature of dual circuits, it is not surprising that swapping the current and back emf waveforms of the Y connection gives a workable solution for the  $\Delta$  connection as shown in Fig. 7.14. Creating a motor with  $120^\circ$  wide square wave back emf waveforms is

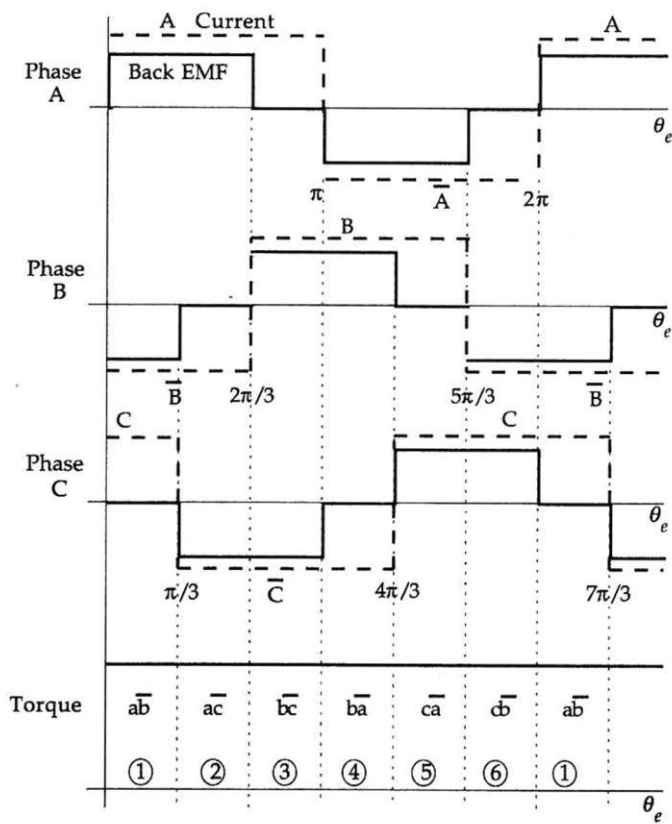


Figure 7.14 Torque production in a  $\Delta$ -connected three-phase motor.

not difficult. Simply making the magnet arc narrower works, which results in the use of less magnet material.

To ease the explanation of the  $\Delta$  connection, the rising edges of the back emf's and currents are aligned in Fig. 7.14. As shown, the back emf of one phase is zero at all times. Each takes a turn at being zero for  $60^\circ$ . Because of this zero back emf, the line current splits approximately equally through the remaining two phases, which conduct current in opposite directions. As before, the torque produced is given by applying (7.6). The lowercase letters under the torque curve signify the line currents during the respective commutation intervals. The line not given in each commutation interval is left floating electrically and is associated with the phase having zero back emf. A comparison of these states with those of the Y connection in Fig. 7.12 shows that the three-phase bridge circuit switches identically for both configurations. It is for this reason that the commutation logic in commercial driver ICs for small brushless motors works with either Y- or  $\Delta$ -connected motors.

To summarize, important aspects of this drive scheme include:

- Ideally, constant ripple-free torque is produced.
- Only six switches are required, which is a minimum number.
- Each phase contributes an equal amount to the total torque produced. Thus each phase experiences equal losses and the drive electronics are identical for each phase.
- Copper utilization remains 67 percent even though all three phases conduct current simultaneously. At all times one phase is conducting current and adding to the ohmic motor loss but is not producing torque since the back emf is zero in each phase one-third of the time.
- The amount of torque produced can be varied by changing the amplitude of the square wave currents.
- Impossible to produce square wave currents are required. The inherent finite rise and fall time of the current creates torque ripple.
- With all else being equal, ohmic motor losses are 50 percent greater than those in the Y connection, but the motor requires only two-thirds of the magnetic material (Miller, 1989).
- Just as in the Y-connected case, the phase current amplitude must be increased by 50 percent to make up for the fact that only two phases are producing the required torque. Since the phase currents are square waves, (6.22) and (6.65) becomes  $I_{ph} = I_s/(2n_s)$ .
- Compared with the three-phase-ON case, ohmic motor losses are 125 percent greater.

- Independent control of phase currents is not possible.
- From  $I_a + I_b + I_c = 0$ , it can be shown that the phase currents cannot have any harmonics that are multiples of three, i.e., triple- $n$  or *triplen* harmonics (Kassakian, Schlecht, and Verghese, 1991).
- Because phases appear in parallel, the supply voltage need only be greater than the peak phase back emf at rated speed.
- The  $\Delta$  connection is traditionally found in low-power, lower-performance motors.

### The sine wave motor

The sine wave back emf motor completes the discussion of three-phase motors. A three-phase motor with sinusoidal back emf can be Y- or  $\Delta$ -connected because there are by definition no triplen harmonics. Excitation of a sinusoidal motor with sinusoidal currents gives constant ripple-free torque just as the two-phase sinusoidal motor does. In this case, the back emf's and currents are all offset from each other by 120 electrical degrees. Following the notation used earlier, the torque is found by substitution into (7.6) and is given by

$$k_A i_A + k_B i_B + k_C i_C = T$$

$$KI \sin^2 \theta + KI \sin^2 (\theta - 120^\circ) + KI \sin^2 (\theta - 240^\circ) = T \quad (7.8)$$

$$3/2KI = T$$

The simple elegance of (7.3) and (7.8) is due to the pure sinusoidal content of the back emf and phase currents. Because of this elegance, a great deal of work goes into the design of some motors to minimize the higher harmonics in the back emf so that a sinusoidal drive can be implemented. Many of the techniques employed were discussed in previous chapters. The sine wave motor commonly appears in high-performance applications where high accuracy and minimal torque ripple are required.

As shown by (7.8), each phase produces torque proportional to one-half the peak value of the current and back emf as compared with a unity ratio for the square wave back emf motor driven three-phase-ON. Therefore, in a sinusoidal motor driven by sinusoidal currents, correction of (6.22) and (6.65) are necessary to establish the rms phase current required to produce a specified torque. The factor of  $1/2$  is taken into account by increasing the current amplitude by a factor of 2. Combining this information with the factor of  $1/\sqrt{2}$  for the rms values of a sinusoid, (6.22) and (6.65) become

$$I_{ph} = \sqrt{2} \frac{I_s}{3n_s} \quad (7.9)$$

## PWM Methods

Specific current waveforms were assumed in each of the motor drive schemes discussed above. To produce these waveforms from a voltage source requires current control. For maximum efficiency, this current control cannot require sustained operation of a power electronic device in its linear operating region. Rather, devices should act as switches having two states: OFF, where power dissipation is zero because there is no current flow, and ON, where power dissipation is low because the voltage across the device is minimized. As a result, current control is implemented as a switching strategy where the switch duty cycle is varied according to some error criterion and the current maintains the correct shape in an average sense only. If switching action occurs at a much higher rate than any variation in the desired current waveform, the deviation between the actual and desired current can be made small. As a whole, these switching strategies are called pulse width modulation (PWM).

Because PWM is applied in countless applications in addition to motor drives, there are hundreds of articles on PWM in the literature. Many of these articles pertain to voltage PWM where one seeks to control voltage rather than current (Holtz, 1992). A smaller number pertain to current control PWM, which is of interest here. As before, the goal is to develop an intuitive understanding rather than discuss every nuance of every PWM scheme. More detailed information can be found in references such as Holtz (1992), Anunciada and Silva (1991), Brod and Novotny (1985), and Murphy and Turnbull (1988).

In motor drive applications, PWM is almost always implemented by controlling the bridge switches themselves. However, switching can also be implemented external to the bridge. Moreover, because motor windings have inductance, PWM action causes the phase inductance to *charge* and *discharge*, giving a continuous current despite the presence of a discontinuous applied voltage. As discussed earlier and shown in Fig. 7.7, inductor discharge can be fast or slow depending upon which switch or switches are controlled by PWM. Intelligent use of this capability can lead to improved performance (Freimanis, 1992).

## Hysteresis PWM

Hysteresis PWM, conceptually the simplest PWM scheme, controls the ON-OFF state of switches to keep the current within a band around the desired value, as shown in Fig. 7.15. In the figure,  $I^*$  is the reference current waveform, i.e., the desired current,  $2\Delta I$  is the tolerance band,  $I^- = I^* - \Delta I$  is the lower bound, and  $I^+ = I^* + \Delta I$  is the upper bound. Whenever the current crosses the upper bound, a switch is opened, allowing current to decay or discharge. Likewise whenever the current

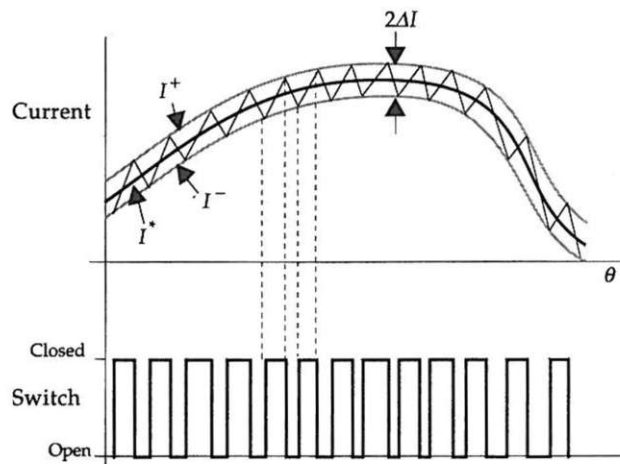


**Figure 7.15** Hysteresis PWM waveforms.

crosses the lower bound, a switch is closed, forcing current to climb in amplitude or charge. Clearly, the rate at which the inductance involved charges and discharges influences the rate at which switching occurs. In a motor drive, where the voltage across the inductance is a function of the difference between a supply voltage and the back emf, the switching frequency will be high at low speeds and low at high speeds. The switching frequency at low speeds can be decreased by increasing the tolerance band. However, this increases the percentage ripple in the current.

Important aspects of this PWM scheme include:

- Precise current control is possible as the tolerance band width is a design parameter.
- The frequency at which switches change state is not a design parameter. As a result, the switching frequency can vary by an order of magnitude or more.
- Acoustic and electromagnetic noise are difficult to filter because their respective spectral components vary with the switching frequency.
- This PWM method is more commonly implemented in motor drives where motor speed and load are constant. Under these circumstances, the variation in switching frequency is small.

#### Clocked turn-ON PWM

This PWM method is the most commonly implemented scheme. Rather than control the peak-to-peak error as the hysteresis controller does, here the switching frequency is held constant. Clocked turn-ON PWM

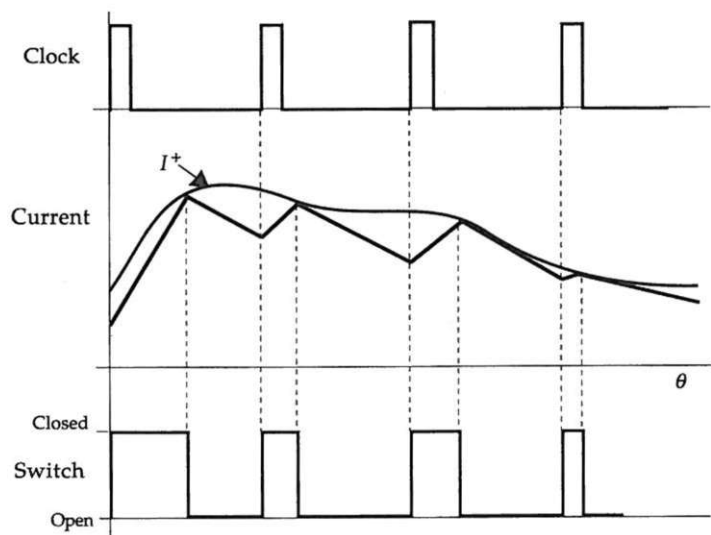


**Figure 7.16** Clocked turn-ON PWM waveforms.

is described in Fig. 7.16, where the top trace is a synchronizing clock. Whenever this clock pulse appears, a switch is closed, causing the inductance to charge. At some point later when the current reaches the  $I^+$ , a switch opens, initiating inductor discharge, which continues until the next clock pulse appears.

Important aspects of this PWM scheme include:

- Current control is not as precise here, since there is no fixed tolerance band that bounds the current.
- The frequency at which switches change state is a fixed design parameter.
- Acoustic and electromagnetic noise are relatively easy to filter because the switching frequency is fixed.
- This PWM method has ripple instability that produces subharmonic ripple components for duty cycles *above* 50 percent (Kassakian, Schlecht, and Verghese, 1991; Anunciada and Silva, 1991). While this instability does not lead to any destructive operating mode, it is a chaotic behavior that reduces performance. The predominant current ripple occurs at one-half the switching frequency.
- Ripple instability can be eliminated by adding a *stabilizing ramp* to the reference current (Kassakian, Schlecht, and Verghese, 1991).

### Clocked turn-OFF PWM

Clocked turn-OFF PWM is the complement of clocked turn-ON PWM. In this method, shown in Fig. 7.17, the clock pulse initiates inductor

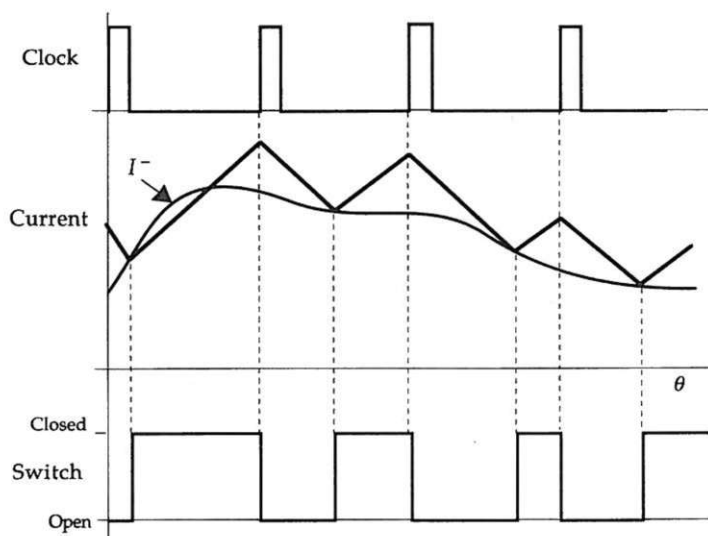


Figure 7.17 Clocked turn-OFF PWM waveforms.

discharge. Later, when the current decays to  $I^-$  a switch closes and the inductance charges until the next clock pulse appears. Once again the switching frequency is fixed by the clock frequency.

Important aspects of this PWM scheme include:

- Current control is not as precise here, since there is no fixed tolerance band that bounds the current.
- The frequency at which switches change state is a fixed design parameter.
- Acoustic and electromagnetic noise are relatively easy to filter because the switching frequency is fixed.
- This PWM method has ripple instability that produces subharmonic ripple components for duty cycles *below* 50 percent (Kassakian, Schlecht, and Verghese, 1991; Anunciada and Silva, 1991). While this instability does not lead to any destructive operating mode, it is a chaotic behavior that reduces performance. The predominant current ripple occurs at one-half the switching frequency.

### Dual current-mode PWM

This PWM method was developed by Anunciada and Silva (1991) to eliminate the ripple instability present in the previous two methods. Their scheme combines the clocked turn-ON and clocked turn-OFF methods in a clever way. For duty cycles below 50 percent, the method implements stable clocked turn-ON PWM, whereas for duty cycles

above 50 percent, the method implements stable clocked turn-OFF PWM.

As illustrated in Fig. 7.18, this method has two clock signals, where the turn-OFF clock is delayed one-half period with respect to the turn-ON clock. Operation is determined by logic that initiates inductor charging when the turn-ON clock pulse appears or the current reaches  $I^-$ , and initiates inductor discharge when the turn-OFF clock appears or the current reaches  $I^+$ . As shown in the figure, the method smoothly moves from one mode to the other. This scheme has all the attributes of the two previous PWM schemes, except for the ripple instability. Furthermore, this scheme reduces to hysteresis PWM if the clock frequency is low compared with the rate at which the inductance charges and discharges.

### Triangle PWM

Triangle PWM is a popular voltage PWM scheme that is commonly used to produce a sinusoidal PWM voltage. When used in this way, it is called sinusoidal PWM (Kassakian, Schlecht, and Verghese, 1991).

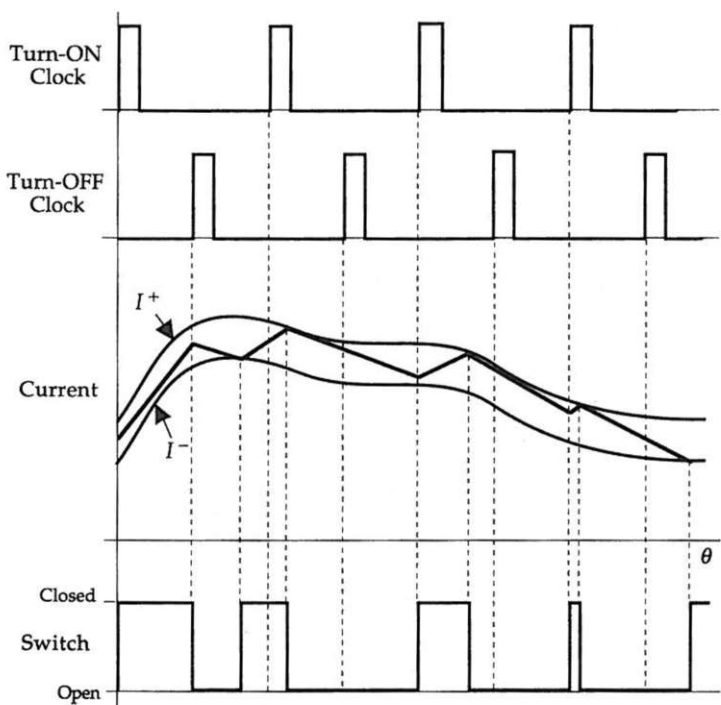


Figure 7.18 Dual current-mode PWM waveforms.

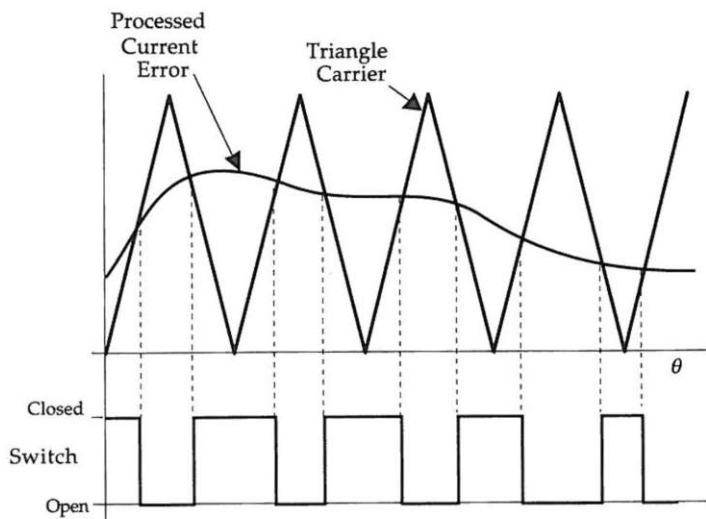


Figure 7.19 Triangle PWM waveforms.

Application of this scheme to current control is accomplished by letting the PWM input be a function of the difference between the desired current and the actual current. As shown in Fig. 7.19, both the turn-ON and turn-OFF of the switch are determined by the intersections of the triangle waveform and the processed current error. As the processed current error increases, so does the switch duty cycle. Typically, the processed current error is equal to a linear combination of the current error and the integral of the current error, i.e., PI control is used. As a result, as the steady-state error goes to zero, the switch duty cycle will go to the correct value to maintain it there. Though Fig. 7.19 shows a unipolar triangle waveform and error signal, both signals can also be bipolar, in which case zero current error produces a 50 percent duty cycle PWM signal (Murphy and Turnbull, 1988).

### Summary

The PWM methods discussed above represent the most common methods implemented in practice. Each method has its own strengths and weaknesses; no one PWM scheme is the best choice for every motor drive. Implementation details for the above PWM methods were not presented so that attention would focus on fundamental switching concepts. For reference, conceptual logic diagrams for each method are shown in Fig. 7.20. These diagrams apply for positive currents only. When the reference current is bipolar, more complex logic diagrams are required.

switching frequency, the smaller the current error will be. On the other hand, the higher the switching frequency, the greater the switching loss incurred by the switches. Furthermore, PWM schemes are only as accurate as the current sensors used. Sensor type, placement, shielding, and signal processing are all critical to accurate operation of a current control PWM method.

# A

## List of Symbols

$A$	Area ( $\text{m}^2$ )	$L_s$	Slot leakage inductance (H)
$B$	Magnetic flux density (T)	$M$	Mutual inductance (H)
$B_a$	Armature reaction flux density (T)	$N$	Number of turns
$B_g$	Air gap flux density (T)	$N_m$	Number of magnet poles
$B_r$	Magnet remanence (T)	$N_p$	Number of pole pairs
$C_d$	Flux concentration factor	$N_{ph}$	Number of phases
$D$	Diameter (m)	$N_s$	Number of slots
$E$	Voltage, emf (V)	$N_{sm}$	Number of slots per magnet pole
$E_b$	Back emf (V)	$N_{sp}$	Number of slots per phase
$E_{\max}$	Maximum back emf (V)	$N_{spp}$	Number of slots per pole per phase
$F$	Magnetomotive force, mmf (A) Force (N)	$P$	Permeance (H) Average power (W)
$H$	Magnetic field intensity ( $\text{A}/\text{m}$ )	$P_c$	Permeance coefficient
$H_c$	Magnet coercivity ( $\text{A}/\text{m}$ )	$P_{cl}$	Core loss (W)
$I$	Current (A)	$P_e$	Eddy current power loss (W)
$I_s$	Total slot current (A)	$P_g$	Air gap permeance (H)
$J_s$	Slot current density ( $\text{A}/\text{m}^2$ )	$P_h$	Hysteresis power loss (W)
$J_{\max}$	Maximum current density ( $\text{A}/\text{m}^2$ )	$P_{hp}$	Power (hp)
$L$	Length (m) Inductance (H)	$P_r$	Resistive, ohmic, or $I^2R$ loss (W)
$L_e$	End turn inductance (H)	$R$	Resistance ( $\Omega$ ) Reluctance ( $\text{H}^{-1}$ )
$L_g$	Air gap inductance (H)	$R$	Radius (m)
		$S$	Motor speed (rpm)

$T$	Torque (N·m)	$\Gamma$	Core loss density (W/kg)
	Temperature (°C)	$\alpha_{cp}$	Coil-pole fraction, $\tau_c/\tau_p$
$V$	Volume ( $m^3$ )	$\alpha_m$	Magnet fraction, $\tau_m/\tau_p$
$W$	Energy (J)	$\alpha_s$	Slot fraction, $w_s/\tau_s$
$W_c$	Coenergy (J)	$\alpha_{sd}$	Shoe depth fraction, $(d_1 + d_2)/w_{tb}$
$d$	Depth or distance (m)	$\delta$	Skin depth (m)
$d_s$	Slot depth (m)	$\mu$	Permeability (H/m)
$e$	Voltage (V)	$\mu_R$	Magnet recoil permeability
$e_b$	Back emf (V)	$\mu_a$	Relative amplitude permeability
$f$	Frequency (Hz)	$\mu_d$	Relative differential permeability
$f_e$	Electrical frequency (Hz)	$\mu_r$	Relative permeability
$f_m$	Mechanical frequency (Hz)	$\mu_0$	Permeability of free space, $4\pi \cdot 10^7$ H/m
$f_{rs}$	Force density ( $N/m^2$ )	$\phi$	Magnetic flux (Wb)
$g$	Air gap length (m)	$\eta$	Efficiency (%)
$g_e$	Effective air gap length (m)	$\lambda$	Flux linkage (Wb)
$i$	Current (A)	$\theta$	Angular position (rad or deg)
$k$	Constant	$\theta_c$	Angular coil pitch (rad or deg)
$k_c$	Carter coefficient	$\theta_e$	Angular electrical position (rad or deg)
$k_{cp}$	Conductor packing factor	$\theta_m$	Angular mechanical position (rad or deg)
$k_d$	Distribution factor	$\theta_p$	Angular pole pitch (rad or deg)
$k_{ml}$	Magnet leakage factor	$\theta_s$	Angular slot pitch (rad or deg)
$k_p$	Pitch factor	$\rho$	Electrical resistivity ( $\Omega \cdot m$ )
$k_s$	Skew factor	$\rho_{bi}$	Back iron mass density ( $kg/m^3$ )
$k_{st}$	Stacking factor	$\sigma$	Electrical conductivity [( $\Omega \cdot m$ ) <sup>-1</sup> ]
$l$	Length (m)	$\tau_c$	Coil pitch (m)
$l_m$	Magnet length (m)	$\tau_m$	Magnet width (m)
$n_c$	Number of turns per coil	$\tau_p$	Magnetic pole pitch (m)
$n_s$	Number of turns per slot	$\tau_s$	Slot pitch (m)
$n_{tpp}$	Number of turns per pole per phase	$\omega$	Frequency (rad/s)
$p$	Instantaneous power (W)	$\omega_e$	Electrical frequency (rad/s)
$q$	Heat density ( $W/m^2$ )	$\omega_m$	Mechanical frequency (rad/s)
$r$	Radius (m)		
$v$	Velocity (m/s)		
$w_{bi}$	Back iron width (m)		
$w_s$	Slot width (m)		
$w_{sb}$	Slot bottom width (m)		
$w_t$	Tooth width (m)		
$w_{tb}$	Tooth bottom width (m)		

# B

## Common Units and Equivalents

Property	SI unit	Equivalents
Magnetic flux	1 weber (Wb)	$10^8$ maxwells or lines $10^5$ kilolines
Flux density	1 tesla (T)	$1 \text{ Wb}/\text{m}^2$ $10^4$ gauss $64.52 \text{ kiloline}/\text{in}^2$
Magnetomotive force (mmf)	1 ampere (A)	1.257 gilberts
Magnetic field intensity	1 ampere/meter (A/m)	$2.54 \cdot 10^{-2}$ ampere/in $1.257 \cdot 10^{-2}$ oersted
Permeability of free space	$4\pi \cdot 10^{-7}$ henry/meter (H/m)	1 henry = 1 Wb/A
Resistivity	1 ohm·meter ( $\Omega \cdot \text{m}$ )	$10^2 \Omega \cdot \text{cm}$ 39.37 $\Omega \cdot \text{in}$
Back emf constant	1 volt·second/radian	104.7 V/k rpm
Velocity	1 radian/second (rad/s)	$30/\pi$ rpm = 9.549 rpm $1/(2\pi)$ rpm = 0.1592 hertz
Length	1 meter (m)	39.37 in 100 cm 1 cm = 0.3937 in 1 mm = 39.37 mils
Area	1 meter <sup>2</sup> (m <sup>2</sup> )	1550 in <sup>2</sup> $10^4 \text{ cm}^2$ $10.764 \text{ ft}^2$ $1.974 \cdot 10^9$ circular mil
Volume	1 meter <sup>3</sup> (m <sup>3</sup> )	$6.1024 \cdot 10^4$ in <sup>3</sup> $10^6 \text{ cm}^3$ $35.315 \text{ ft}^3$
Mass	1 kilogram (kg)	1000 grams 2.205 lb 35.27 oz $6.852 \cdot 10^{-2}$ slug

Property	SI unit	Equivalents
Mass density	1 kilogram/meter <sup>3</sup> (kg/m <sup>3</sup> )	$6.243 \cdot 10^{-2}$ lb/ft <sup>3</sup> $3.613 \cdot 10^{-5}$ lb/in <sup>3</sup> $5.780 \cdot 10^{-4}$ oz/in <sup>3</sup>
Force	1 newton (N)	$1 \text{ m}\cdot\text{kg}/\text{s}^2$ 0.2248 pound (lb <sub>f</sub> ) 3.597 ounces (oz <sub>f</sub> ) $10^5$ dynes
Torque	1 newton·meter (N·m)	141.61 oz·in 8.85 lb·in 0.738 lb·ft $10^7$ dyne·cm $1.02 \cdot 10^4$ g·cm
Energy	1 joule (J)	1 W·s $9.478 \cdot 10^{-4}$ Btu
Power	1 watt (W)	1 J/s $1/746$ hp = $1.3405 \cdot 10^{-3}$ hp
Current density	1 ampere/meter <sup>2</sup> (A/m <sup>2</sup> )	$10^{-4}$ A/cm <sup>2</sup> $6.452 \cdot 10^{-4}$ A/in <sup>2</sup> $5.066 \cdot 10^{-10}$ A/circular mil
Energy density	1 joule/meter <sup>3</sup> (J/m <sup>3</sup> )	$1.6387 \cdot 10^{-5}$ J/in <sup>3</sup> $1.5532 \cdot 10^{-8}$ Btu/in <sup>3</sup> $1.257 \cdot 10^2$ gauss·oersted (G·Oe) 1 MG·Oe = 7.958 kJ/m <sup>3</sup>
Power density (mass)	1 watt/kilogram (W/kg)	0.4535 W/lb $6.083 \cdot 10^{-4}$ hp/lb
Power density (area)	1 watt/meter <sup>2</sup> (W/m <sup>2</sup> )	$10^{-4}$ W/cm <sup>2</sup> $6.452 \cdot 10^{-4}$ W/in <sup>2</sup>
Force density	1 newton/meter <sup>2</sup> (N/m <sup>2</sup> )	$1.450 \cdot 10^{-4}$ lb/in <sup>2</sup> (psi)

# Bibliography

- Anunciada, V., and M. M. Silva (1991), "A New Current Mode Control Process and Applications," *IEEE Transactions on Power Electronics*, vol. 6, no. 4, pp. 601-610.
- Brod, D. M., and D. W. Novotny (1985), "Current Control of VSI-PWM Inverters," *IEEE Transactions on Industry Applications*, vol. IA-21, No. 4, pp. 562-570.
- Chai, H. D. (1973), "Permeance Model and Reluctance Force between Toothed Structures," *Proceedings of the Second Annual Symposium on Incremental Motion Control Systems and Devices*, B. C. Kuo, ed., Urbana, IL, pp. K1-K12.
- de Jong, H. C. J. (1989), *AC Motor Design: Rotating Magnetic Fields in a Changing Environment*, Hemisphere Publishing Company, New York. *This text can be viewed as a successful attempt to rewrite the material presented in the classic motor design texts of the first half of this century. As opposed to those earlier texts, the notation and terminology in this text reflects modern thinking.*
- Freimanis, M. (1992), "Hybrid Microstepping Chopper Can Reduce Iron Losses," *Motion Control*, April 1992, pp. 36-39.
- Gogue, G. P., and J. J. Stupak (1991), "Professional Advancement Courses, Part A: Electromagnetics Design Principles for Motors/Actuators, Part B: DC Motor/Actuator Design," *PCIM Conference 1991*, Sept. 22-27, Universal City, CA. *This set of notes is used by the authors in day-long short courses. The basics of magnetic circuit modeling are covered. A very good discussion of permanent magnets and magnetizing techniques and fixtures is presented. Some equations are presented, but for the most part the notes contain a wealth of practical information not found in college textbooks.*
- Hague, B. (1962), *The Principles of Electromagnetism Applied to Electrical Machines*, Dover Publications, New York. *This text is a reprint of a text originally published in 1929. It offers an amazing collection of analytically derived field distributions and force equations applicable to electrical machines.*
- Hanselman, D. C. (1993), "AC Resistance of Motor Windings Due to Eddy Currents," *Proceedings of the Twenty-Second Annual Symposium on Incremental Motion Control Systems and Devices*, B. C. Kuo, ed., Urbana, IL, pp. 141-147.
- Hendershot, J. R. (1991), *Design of Brushless Permanent Magnet Motors*, Magna Physics Corp., Hillboro, OH. *This text is more of a survey of motor design, material properties, and manufacturing techniques than a text on motor design itself. Very few equations are presented, but the immense amount of practical information presented is indispensable. An excellent companion to the text you're holding.*
- Holtz, J. (1992), "Pulsewidth Modulation—A Survey," *IEEE Transactions on Industrial Electronics*, vol. 39, no. 5, pp. 410-420.
- Huang, H., W. M. Anderson, and E. F. Fuchs (1990), "High-Power Density and High Efficiency Motors for Electric Vehicle Applications," *Proceedings of the International Conference on Electric Machines*, Cambridge, MA, pp. 309-314.
- Kassakian, J. G., M. F. Schlecht, and G. C. Verghese (1991), *Principles of Power Electronics*, Addison Wesley, Reading, MA. *This text is refreshingly different from most power electronics texts in that it seeks to convey fundamental principles rather than just extensively analyze every possible power electronic circuit. What the text lacks is sufficient extensive examples which put the fundamental principles to work.*
- Leonhard, W. (1985). *Control of Electrical Drives*, Springer-Verlag, New York. *A classic text on the control of all common motor types.*
- Li, Touzhu, and G. Slemmon (1988), "Reduction of Cogging Torque in Permanent Magnet Motors," *IEEE Transactions on Magnetics*, vol. 24, no. 6, pp. 2901-2903.

- Liwschitz-Garik, M., and C. C. Whipple (1961). *Alternating-Current Machines*, Second Edition, D. Van Nostrand Company, Princeton NJ. *This text, first printed in 1946, is one of the last classic texts on electric machines. It's one of those books that many well-seasoned motor designers have on their bookshelf. The notation and terminology used in this text is antiquated but discernible with some effort.*
- McCaig, M., and A. G. Clegg (1987), *Permanent Magnets in Theory and Practice*, Second Edition, John Wiley & Sons, New York. *This text represents one of the very few readable texts on permanent magnets. As the title states, the text presents both theory and practice, and does a good job of it. This text is a rewrite of a prior edition and does contain significant information on neodymium-iron-boron magnet material. This is an excellent text for those who seek a greater understanding of permanent magnets than that typically presented in a motor book.*
- McPherson, G., and R. D. Laramore (1990), *An Introduction to Electrical Machines and Transformers*, Second Edition, John Wiley & Sons, New York. *This is one example of the many college texts available in this area. This text is both more readable and more thorough than most.*
- Miller, T. J. E. (1989), *Brushless Permanent-Magnet and Reluctance Motor Drives*, Oxford University Press, New York. *This text is a survey of modern brushless motors. It is very readable but lacks some depth in most areas simply because the text covers so much ground. Overall, it is a required text for those involved in the business of brushless motors.*
- Mukherji, K. C., and S. Neville (1971), "Magnetic Permeance of Identical Double Slotting: Deductions from Analysis by F. W. Carter," *Proceedings of the IEE*, vol. 118, no. 9, pp. 1257-1268.
- Murphy, J. M. D., and F. G. Turnbull (1988), *Power Electronic Control of AC Motors*, Pergamon Press, Oxford, UK. *This text covers the electronic control of all major motor types. Just about every control scheme is illustrated. Some power semiconductor material is presented. It is by far the most comprehensive text of its kind.*
- Nasar, S. A. (1987), *Handbook of Electric Machines*, McGraw-Hill, New York. *This text is truly a handbook. It contains chapters submitted by numerous authors, and a wide variety of motor types are considered. A thorough presentation of magnetic circuit analysis and its limitations is made in Chapter 2.*
- Prina, S. R. (1990), *The Analysis and Design of Brushless DC Motors*, Ph.D. Thesis, University of New Hampshire, Durham, NH. *This thesis correlates the measured characteristics of a brushless permanent-magnet motor with results predicted by finite element analysis. This thesis is extremely important to those wishing to know the limitations of finite element analysis.*
- Qishan, G., and G. Hongzhan (1985), "Effect of Slotting in PM Electric Machines," *Electric Machines and Power Systems*, vol. 10, pp. 273-284.
- Roters, H. C. (1941), *Electromagnetic Devices*, John Wiley & Sons, New York. *This is a classic text on magnetic modeling. The circular-arc, straight-line approach to permeance modeling is introduced in this text.*
- Sebastian, T., G. R. Slemon, and M. A. Rahman (1986), "Design Considerations for Variable Speed Permanent Magnet Motors," *Proceedings of the International Conference on Electrical Machines*, München, Germany, pp. 1099-1102.
- Sebastian, T., and G. R. Slemon (1987), "Operating Limits of Inverter Driven Permanent Magnet Motor Drives," *IEEE Transactions on Industry Applications*, vol. IA-23, no. 2, pp. 327-333.
- Slemon, G. R., and X. Liu (1990), "Core Losses in Permanent Magnet Motors," *IEEE Transactions on Magnetics*, vol. 26, no. 5, pp. 1653-1655.
- Slemon, G. R. (1991), "Chapter 3: Design of Permanent Magnet AC Motors for Variable Speed Drives," *Performance and Design of Permanent Magnet AC Motor Drives*, IEEE Press, New York. *This reference is from the published notes of a day-long short course presented by six well-respected authors at the IEEE Industry Applications Society Conference in Dearborn, MI.*
- Ward, P. A., and P. J. Lawrenson (1977), "Magnetic Permeance of Doubly-Salient Air-gaps," *Proceedings of the Institution of Electrical Engineers*, vol. 124, no. 6, pp. 542-544.

- Air gap:  
inductance, 80, 81  
modeling, 19–21
- Armature reaction, 89–91
- Axial flux topology, 122, 123
- Back emf, 46, 59, 70–72, 113–115  
in axial flux design, 147, 148  
in radial flux design, 131  
sinusoidal, 121  
trapezoidal, 121
- Back iron, 64
- BLi law, 57, 59, 91
- BLv law, 47, 59
- Carter coefficient, 22, 68
- Clocked turn-OFF PWM, 176, 177
- Clocked turn-ON PWM, 175, 176
- Coenergy, 48, 50, 51  
for computing inductance, 81  
in doubly-excited systems, 50, 51  
in singly-excited systems, 48–50  
in the presence of a PM, 51
- Coercivity ( $H_c$ ), 31  
(*See also* Remanence)
- Cogging torque, 7, 58, 112, 113, 117–120
- Coil, 75  
magnetic circuit model, 18, 19
- Coil-pole fraction, 115, 144, 145
- Commutation, 155
- Conductor packing factor, 87, 133
- Core loss, 28–30, 96
- Current:  
in a Δ-connected motor, 172  
in axial flux design, 148  
in an H-bridge switch, 164  
in radial flux design, 132  
in a sine wave motor, 173  
in a Y-connected motor, 168, 169
- Δ connection, 170–173
- Detent:  
positions, 7  
torque, 7, 58, 112, 113, 117–120
- Distribution factor, 115
- Dual air gap construction, 99–101
- Dual current-mode PWM, 177, 178
- Eddy current:  
in conductors, 88, 89  
loss, 28, 29
- End turn leakage inductance, 82–84
- Energy, 48, 49, 51  
in doubly-excited systems, 50, 51  
in singly-excited systems, 48–50  
in the presence of a PM, 51  
(*See also* Work)
- Factor:  
conductor packing, 87, 133  
distribution, 115  
flux concentration, 37, 38, 143  
magnet leakage, 67, 142  
pitch, 115–117  
skew, 119  
stacking, 30
- Faraday's law, 46
- Finite element analysis, 13, 14
- Flux concentration, 37, 38
- Flux concentration factor, 37, 38, 143
- Flux linkage, 41, 42, 69, 70
- Flux squeezing, 24
- Force, 52, 73, 74  
conductor, 91–93  
cogging, 93–95  
relationship to torque, 4  
relationship to power, 52  
due to skewing, 120  
(*See also* Torque)
- Fraction:  
coil-pole, 115, 144, 145  
magnet, 66, 141  
slot, 24, 120, 129
- Fractional pitch, 111
- Frequency, fundamental electric, 11
- Fringing, 19
- Fundamental design issues, 96–99

- H-bridge, 161–163  
shoot-through fault in, 165
- Hysteresis:  
loop, 26, 28  
loss, 28, 29  
PWM, 174, 175
- $I^2R$  loss, 76
- Inductance:  
air gap, 80, 81  
in axial flux design, 149, 150  
end turn leakage, 82–84  
mutual, 42, 85, 86  
in radial flux design, 134, 135  
self, 41, 42, 78–84  
slot leakage, 81, 82, 109
- Lamination, 29, 30
- Law:  
BL<sub>i</sub>, 57, 59, 91  
BL<sub>v</sub>, 47, 59  
Faraday's, 46  
Lenz's, 46
- Loading, electric and magnetic, 99
- Lorentz force equation, 56, 63
- Loss:  
core, 28–30, 96  
eddy current, 28, 29  
hysteresis, 28, 29  
ohmic, resistive, or  $I^2R$ , 76
- Magnet (*See* Permanent magnet)
- Magnet aspect ratio, 67, 68
- Magnetic circuit concepts, 14
- Magnet fraction, 66, 141
- Magnet leakage factor, 67, 142
- Magnet leakage flux, 66
- Magnet shaping, 120
- Magnetomotive force (mmf), definition of, 16
- Motor action, 5
- Motor size, 11, 12
- Mutual inductance, 42, 85, 86
- Ohmic loss, 76
- Peak current density, 133
- Permanent magnet (PM):  
bonded versus sintered, 30  
magnetic circuit model, 34–36  
permeance, 35  
properties:  
coercivity, 31
- Permanent magnet (PM), properties  
(*Cont.*):  
maximum energy product, 33  
recoil permeability, 32  
remanence, 31  
temperature dependence of, 32–34  
types, 30
- Permeance, definition of, 16, 17
- Permeance coefficient (PC), 32, 38, 68, 143
- Permeability:  
of freespace, 26  
recoil, 32  
relative, 26  
relative amplitude, 27  
relative differential, 27
- Pitch:  
factor, 115–117  
pole, 66, 67, 70, 115–117  
slot, 22–24, 108, 129
- Pole:  
consequent, 103  
magnet, 8  
salient, 9, 107
- Position, mechanical and electrical, 10
- Power:  
electrical, 59  
mechanical, 52, 53, 59
- Pulse width modulation (PWM) methods:  
clocked turn-ON, 175, 176  
clocked turn-OFF, 176, 177  
dual current-mode, 177, 178  
hysteresis, 174, 175  
triangle, 178, 179
- Radial flux topology, 122
- Recoil permeability, 32
- Relative permeability, 26
- Reluctance, definition of, 17
- Remanence,  $B_r$ , 31  
(*See also* Coercivity)
- Resistance:  
in axial flux design, 148, 149  
end turn, 86  
in radial flux design, 133, 134  
slot, 86  
winding:  
ac, 88, 89  
dc, 87, 88
- Resistive loss, 76
- Resistivity of annealed copper, 87
- Right-hand rule, 56
- Right-hand screw rule, 18
- Ripple instability, 176, 177

- Rotor, 1, 3  
Rotor variations, 103–105
- Self inductance, 41, 42, 78–84  
Shoes, 107, 118  
Six step drive, 167  
Skew factor, 119  
Skewing, 118–120  
Skin depth, 88  
Slot:  
    definition, 9  
    fraction, 24, 120, 129  
    leakage inductance, 81, 82, 109  
    modeling, 21–24  
Speed voltage (*See* Back emf)  
Stacking factor, 30  
Stator, 1, 3  
Stator variations, 106, 107
- Teeth, 9, 107  
Three-phase motors:  
     $\Delta$  connection, 170–173  
    Y connection, 166–170
- Topologies:  
    axial flux, 3, 121–123  
    radial flux, 3, 121, 122
- Torque: 4, 5, 53  
    in axial flux design, 147  
    cogging or detent, 7, 58, 112, 113, 117–120  
    from a macroscopic viewpoint, 54–56  
    from a microscopic viewpoint, 56, 57  
    with respect to motor size, 11  
mutual or alignment, 7, 55, 58  
in radial flux design, 131  
relationship to force, 4  
relationship to power, 52  
reluctance, 7, 55, 57, 58  
repulsion, 7  
Triangle PWM, 178, 179  
Triplen or triple-n, 170, 171, 173  
Turn, 75
- Winding:  
    chorded, short-pitch, or fractional-pitch, 115, 118  
    double-layer lap, 77  
    single-layer lap, 76, 77  
    single-layer wave, 77, 78  
    solenoidal, 9
- Work, 52  
    (*See also* Energy)
- Y connection, 166–170

## **ABOUT THE AUTHOR**

Duane C. Hanselman is an Associate Professor in Electrical Engineering at the University of Maine, Orono. He holds a Ph.D. and an M.S. in Electrical Engineering from the University of Illinois and is a Senior member of the Institute of Electrical and Electronics Engineers (IEEE). Dr. Hanselman is the author of numerous articles on motors and motion control. He is a coauthor of *MATLAB® Tools for Control System Analysis and Design* and a contributing author of *Teaching Design in Electrical Engineering*.

# ***Everything you need to know to design tomorrow's most popular motor today!***

Brushless permanent-magnet motors are increasingly the motor of choice in a wide range of applications, from hard disk drives, laser printers, and VCRs to a variety of industrial and military uses such as robotics, factory automation, and electric vehicles. As their cost continues to decline, they're sure to become a dominant motor type because of their simplicity, reliability, and efficiency. With this book you can find out how these motors work, what their fundamental limitations are, and how to design them.

In an easy-to-follow, keep-it-simple style, the book's author Duane C. Hanselman begins with the fundamental concepts of generic motor operation and design. Based on these fundamental concepts he identifies and explains terminology, i.e., the buzzwords, common to motor design. In addition, he describes how the fundamental concepts both influence and limit motor design and performance. Hanselman also discusses brushless DC and synchronous motor design for both cylindrical (radial) and pancake (axial) topologies.

All the concepts and analytical tools you need are here in one source. A wealth of figures, tables, and equations are provided to illustrate and document all the essential aspects of motor design. Whether you design motors or specify and design systems that use them, you'll find this up-to-date reference absolutely essential.

Cover Design: Kay Wanous

**ISBN 0-07-026025-7**



90000

**McGraw-Hill, Inc.**  
Serving the Need for Knowledge  
1221 Avenue of the Americas  
New York, NY 10020